Diss. ETH No. 23191

Dynamics and temperature of shear banding in metallic glasses

A thesis to attain the degree of
DOCTOR OF SCIENCES of ETH ZURICH
(Dr. sc. ETH Zurich)

presented by
PETER THURNHEER

M.Sc. in Materials Science, ETH Zurich

Born 2nd November 1985
Citizen of Weinfelden TG

Accepted on the recommendation of

Prof. Dr. Jörg F. Löffler, examiner
Prof. Dr. Robert Maaß, co-examiner
Prof. Dr. Mihai Stoica, co-examiner

2016

Acknowledgments

Writing these lines of acknowledgment, and thereby realizing that I have come very close to successfully completing this almost five-year doctoral thesis, I may, in fact, consider myself grateful, and maybe lucky. Luck is said to be nothing more than what happens when preparation meets opportunity, and for both, opportunity and preparation, I am very much indebted to a number of people, to whom I would like to express my deepest gratitude. The *opportunity* to carry out my doctoral thesis at ETH Zurich was generously given to me by Prof. Jörg F. Löffler. I am grateful for his supervision of this thesis, for scientific discussions and for his trust in me to define the research directions of my work independently. I would not have been able to profit from this great opportunity without the *preparation*, meaning the mentoring that I have received from Dr. K. Laws and, in particular, by Prof. Robert Maaß, who both continuously supported and encouraged me throughout the duration of this thesis and participated in many fruitful discussions. I also thank Prof. Robert Maaß and Prof. Mihai Stoica for co-refereeing this work.

I am further indebted to D. Granata, who introduced me to the ternary metallic-glass system Zr–Cu–Al, which stands at the beginning of this work, and to F. Haag, who convinced me to monitor flow discontinuities also with Infrared-Thermography. This work was further supported by B. Wegmann (raw metal etching), E. Fischer (technical support), J. Hecht (LabView programming) and C. Wegmann (general technical support and brain storming).

Outside ETH, the maintaining of a work-life balance was facilitated by my band, friends and family and of course my girlfriend Lorenza, who was the greatest support during the last five years.

Table of Contents

Summary

While outscoring conventional metallic materials in terms of strength and elastic-strain limit, Metallic Glasses (MGs) are inferior in their capability to deform plastically. The designation "exclusively brittle" is misleading, however, because in loading conditions other than tension, considerable amounts of plastic strain, highly localized within narrow layers of weakened material, has been reported. Plastic flow on shear bands, which is what these layers are called, is discontinuous and reminiscent of stick-slip phenomenology, including phases of slow elastic loading followed by phases of fast plastic slip and unloading. Shear bands are the key to an improved understanding of MG plasticity, and thus to advanced alloy-design strategies allowing for the beneficial tailoring of mechanical properties. Because shear bands have a minimal lateral extension, operate during short time scales only, and initiate at locations which are difficult to predict, *in-situ* studies on their properties represent a challenging task. In this study, high-acquisition rate instrumented mechanical testing was used to assess the dynamic properties of shear bands. The question of temperature- and composition-dependent shear-band stability in Zr-, Cu-, Pt-, La- and Au-based metallic glasses is addressed. The heating of a shear band during flow discontinuities is also investigated via infrared thermometry. It is found that shear-band stability, reflected by the activation energy E_S of the shear-band velocity, is strongly composition-dependent, both within and among specific glass-forming systems. A model is presented, which correlates the composition-dependent activation energies with bonding energies of atoms centring typical topological short-range order clusters within the MG structure. It is further found that shear-band heating during flow discontinuity is closely related to shear-band dy-

namics, and causes temperature increases of a few degrees only during stable plastic flow. The results of this thesis not only shed light on the physical origin of composition-dependent shear-band stability, but also define paths for future research aiming at the beneficial tailoring of MG properties.

Zusammenfassung

Metallische Gläser mögen die Festigkeit und die elastische Dehnbarkeit konventioneller Metalllegierungen deutlich übertreffen, doch in Bezug auf plastische Verformung sind sie klar unterlegen. Das heisst nun aber nicht, dass es sich bei Metallischen Gläsern um vollkommen spröde Materialien handelt. Im Gegenteil, unter Last, sofern es denn keine reine Zuglast ist, wird von beträchtlicher plastischer Dehnung berichtet, welche sich auf dünne Schichten von aufgeweichtem Material, den sogenannten Scherbändern, konzentriert. Die Verformung läuft dabei diskontinuierlich ab und erinnert an den aus der Tribologie bekannten Haftgleiteffekt, bei welchem sich Phasen von langsamem, elastischem Aufladen mit Phasen von schnellem, plastischem Entladen abwechseln. Die Scherbänder sind der Schlüssel zum Verständnis der plastischen Verformung in Metallischen Gläsern und damit auch zu neuen Wegen für die Abstimmung von Material und Anwendung. Aufgrund der geringen Scherbanddicke, der sehr kurzen Zeitdauer der plastischen Gleitphase und der Unvorhersehbarkeit des genauen Ortes der Scherbandbildung erweisen sich *in-situ* Studien der Eigenschaften aktiver Scherbänder als ein besonders herausforderndes Unterfangen. In dieser Arbeit werden mechanische Versuche mit sehr genauer Zeitauflösung an verschiedenen metallischen Glaslegierungen durchgeführt, mit dem Ziel, die Temperatur- und Zusammensetzungsabhängigkeit der dynamischen Scherbandeigenschaften zu erfassen. Des Weiteren wird die durch die starke Lokalisierung der Verformung herrührende Erwärmung des Materials mittels Infrarot-Thermometrie untersucht. Es stellt sich heraus, dass die Scherbandstabilität, beschrieben durch die Aktivierungsenergie E_S der thermisch aktivierten Scherbandgeschwindigkeit, eine starke Abhängigkeit von der Legie-

rungszusammensetzung, sowohl innerhalb eins bestimmten Systems als auch zwischen verschiedenen Legierungssystemen, aufweist. Ein Modell wird präsentiert, welches die zusammensetzungsabhängige Aktivierungsenergie mit den Bindungsenergien von Atomen in legierungsspezifischen, typischen Nahordnungsstrukturen in Verbindung bringt. Des Weiteren wird gezeigt, dass die Materialerwärmung, welche die Fliessdiskontinuitäten von metallischen Gläsern begleitet, in enger Verbindung zur Scherbanddynamik steht und im Falle des stabilen Fliessens nur wenige Grad Celsius beträgt.

Stichworte: Metallische Gläser, mechanische Eigenschaften, Scherbänder, Scherbanddynamik, Scherbandtemperatur, Glas Plastizität, Materialdesign

"Do what you can, with what you have, where you are."

Theodore Roosevelt

1.   Introduction

*"Durch Forschen nur gewinnt man Vorsicht
und Bedacht in allem Tun."*

Sophokles

The microstructure and mechanical properties of a material are strongly interconnected. In conventional metallic alloys, the generation, propagation and interaction of dislocations are key processes which determine strength and ductility. In metallic glasses (MGs), these mechanisms are absent, because the atomic structure provides no long-range order and thus no gliding planes on which dislocations may operate. Therefore, one might expect the material to have a yield strength close to the ideal limit and to be, as the proverb goes, *as brittle as a glass*. The first expectation is justified. Metallic glasses are stronger by far than their conventional crystalline counterparts [1-5], reaching strengths up to five GPa [6]. Combining high strength with a high elastic limit of about 2-3% [7], these materials can store large amounts of elastic energy, which makes them attractive for applications such as watch springs [8] sports goods [9], and fasteners [10]. The second expectation is almost justified. In fact, metallic glasses fail brittle in tension [11]. Under certain conditions such as during bending, compression testing [12] or fracture-toughness measurements [13], however, considerable amounts of plastic deformation have been reported. This deformation is highly localized within narrow layers of weakened material, called shear bands. Because of these bands, MGs are

not exclusively brittle, such as oxide glasses. The prospect of new design strategies for developing MGs with improved plastic deformability thus motivates a thorough investigation of shear bands and the factors which determine their resistance towards catastrophic fracture.

This dissertation starts with a general introduction to the topic of Metallic Glasses (MGs), covering structural and basic mechanical aspects (chapter 2). Experts in the field of MGs might start their reading directly at chapter 3, where the fundamentals of localized flow are reviewed. The aims of this thesis are specified in chapter 4, followed by the experimental details in chapter 5. The results of this thesis are then presented in chapter 6, which is divided into four parts. The first part focusses on effects of geometry and geometric constraint, the second and third parts investigate shear-band dynamics during serrated flow within the Zr–Cu–Al ternary and among various metallic glass systems, respectively, and the fourth part covers the *in-situ* experiments on shear-band temperature performed via IR thermography. In chapter 7, the results of the various studies are compiled and discussed in relation to each other.

2. Metallic glasses in general

„She lives in a world of her own – a world of –
little glass ornaments.“

Tennessee Williams, the Glass Menagerie

2.1.   Glasses in general

By definition, a glass is an amorphous solid produced by rapid removal of heat from the molten state, that is, by freezing-in the structure of a liquid into a solid[1]. Glasses are thus meta stable materials, because they are kinetically stabilized only, but do not represent the thermodynamically most stable structural modification. The term "amorphous" implies that there is neither long-range order nor translational symmetry in the atomic structure. Figure 2-1 shows a schematic Time-Temperature-Transformation (TTT) diagram for a glass-forming material, schematically showing the atomic structures of liquid, glass and crystal. The atomic arrangement in the liquid phase ($T>T_l$) is disordered, but not completely random. In the example shown in Figure 2-1, each atom is typically coordinated by six to seven nearest neighbours. The liquid thus possesses some degree of short-range order (SRO). Upon slow cooling, the long-range ordered, crystalline phase usually forms via diffusive rearrangements of the atoms. If, however, cooling to

---

[1] The defining property of "glass" differs in everyday jargon (optical transparency) and physics jargon (disordered atomic structure and processing route).
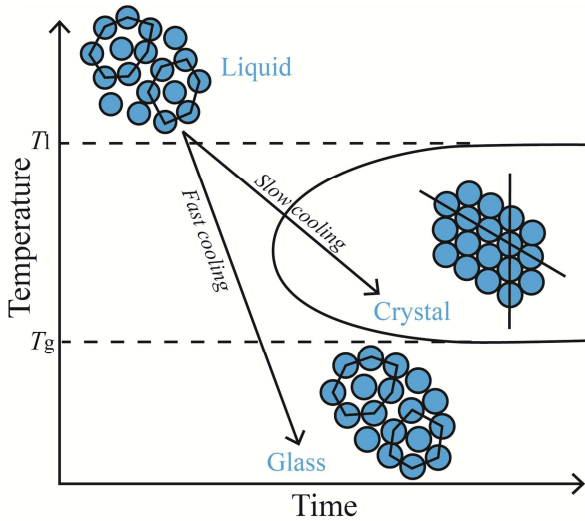
Figure 2-1: Schematic TTT diagram for a glass-forming material.

temperatures below the glass transition temperature T_g is fast enough to suppress these kinetic rearrangements necessary for crystallization, the liquid-like structure is maintained in the solid, and a glass is formed. Compared to the liquid state, the glass is denser and the degree of SRO is increased.

The cooling rate required for glass formation increases with an increased mobility of the constituents in the liquid phase. Kinetics in oxide or polymer melts can be rather slow, so that oxide glasses, such as obsidian, or amorphous polymers, such as rubber, are naturally occurring materials. Cooling rates required for *metallic* glass formation are very high and may only be reached using sophisticated experimental equipment.

2.2. A short history of metallic glasses

In search of metastable, crystalline phases, Pol Duwez, a researcher at the California Institute of Technology, continuously

improved experimental techniques to cool down metal melts at progressively higher rates. This was achieved by improving the heat conduction away from the melt by using copper as a mould material, and by limiting the total heat content of the system by working with small sample volumes only. In Ag–Cu, for example, Duwez succeeded in producing metastable foils of solid solutions, not predicted by the equilibrium phase diagram [14]. Applied to a binary Au–Si alloy [15], the cooling rate of the setup was eventually high enough to fully suppress the diffusive rearrangements necessary for crystallization, leading to the formation of an amorphous metallic solid instead. In his own words: "That was the first liquid-quench amorphous alloy" [16]. Duwez himself used the term "amorphous phases" [17], because "thermal and rheological" evidence that these new materials were truly glasses were only provided in 1967 and 1968 by Chen and Turnbull [18, 19]. Soon, more and more glass-forming alloys were discovered, based on Te [20], Fe [21] and Pd [22]. These early glass-forming alloys only allowed for the production of samples with a maximum thickness of some tens of microns due to the very high cooling rates required. In the 1980s and 1990s new alloys requiring only modest cooling rates were discovered in the alloy systems Al–La–Ni [23] Zr–Al–TM [24] (where TM stands for Transition Metal), Zr–Ti–Cu–Ni–Be [25], and Pd–Cu–Ni–P [26]. In these alloy systems, metallic glass samples of several millimetres in thickness (bulk metallic glasses) can be obtained.

2.3. The structure of metallic glasses

Mechanical properties are inherently connected to the micro- and atomic structure of a material. A deepened understanding of mechanical properties is thus impossible without a deepened understanding of the materials' structure. Figure 2-2 compares the
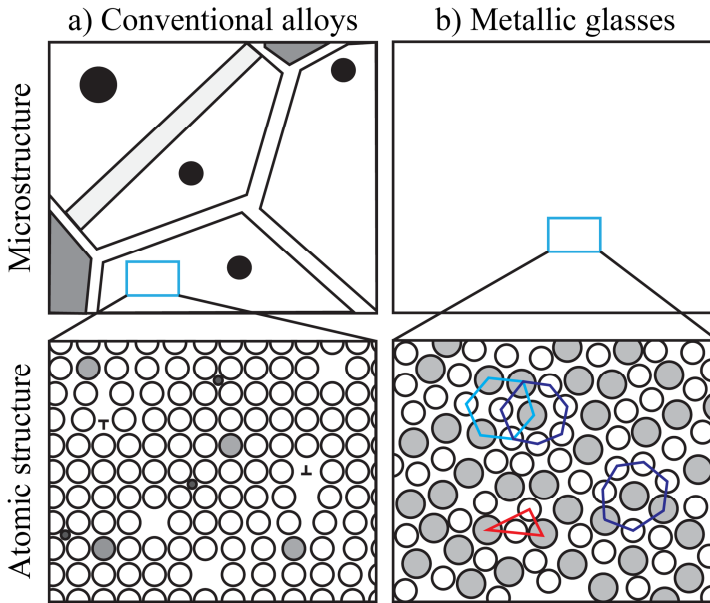
Figure 2-2: Structural features of conventional alloys (a) and metallic glasses (b) at the micro- and the atomic scale.

micro- and atomic structure of conventional alloys (a) with that of metallic glasses (b). At the micro-scale, conventional alloys show features such as grains, grain boundaries, precipitates, twins, and secondary phases. These features are absent in the homogeneous microstructure of the metallic glass

The atomic-scale structure of conventional, crystalline alloys is characterized by long–range order and typical crystal defects such as substitute or interstitial atoms, vacancies and, most important for mechanical properties, dislocations. Next to the strength of chemical bonds, the interaction of dislocations with other micro-structural features is the most essential influence on the mechanical performance of a crystalline material. The atomic structure of metallic glasses - here given for a binary alloy of small white and

large grey species – appears to be featureless; at least at first sight. Structural heterogeneity is only revealed upon closer inspection. While long-range order is absent, short-range order prevails, meaning that neighbouring atoms are located at typical distances from each other. The entity of any atom and its nearest neighbours is called a cluster. Every atom is centring its own cluster, but, at the same time, it is also a constituent of the clusters centred by any of its nearest neighbours. From that perspective, the structure of MGs can be described as a network of interpenetrating, short-range ordered clusters of various shapes and sizes. Assuming chemical homogeneity, these clusters differ mainly in the efficiency of their packing. Examples of densely (light blue, dark blue) and of loosely (red) packed clusters are indicated in Figure 2-2. Note that atoms of the small species are typically centring clusters with fewer neighbours (light blue, 6) than atoms of the large species (dark blue, 7). With densities of more than 97% of their crystalline counterparts, efficient atomic packing is a key characteristic of the metallic-glass structure. In a theoretical model, Miracle *et al.* [27] provided a way to predict the most efficiently packed motifs in an MG alloy, only requiring atomic diameter and fraction of the components as input values. In the simple case where one type of atom is abundant (solvent) compared to the other (solute), the typical structural motif is given by a solute atom coordinated (surrounded) exclusively by solvent atoms.

Figure 2-3a shows how solvent atoms (white) pack around a centre atoms (blue) for a varying relative radius ratio $R = r_{\text{solute}}/r_{\text{solvent}}$ in two dimensions. For $R = 0.414$ efficient packing with a coordination number of $N = 4$ is achieved. Efficient packing here means that two adjacent atoms in the coordinating shell are also nearest neighbours to each other, meaning that they touch. For $R = 0.701$, efficient packing is achieved for five neighbours. For $R = 0.85$,
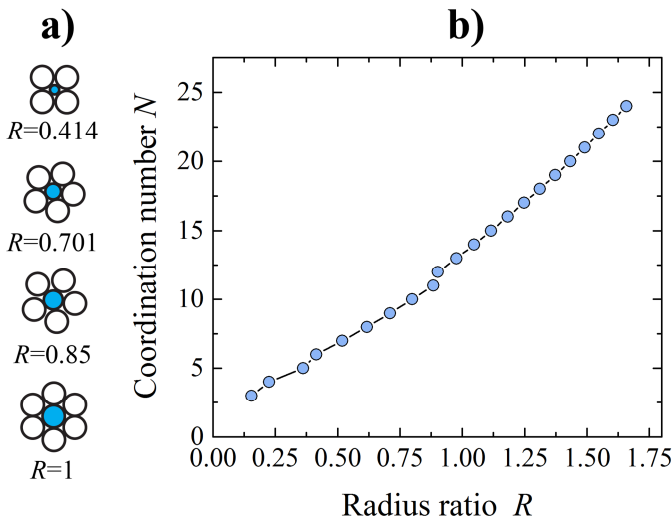
Figure 2-3: a) Packing for different radius ratios in two dimensions; b) coordination number of an efficiently packed cluster as a function of radius ratio R. Both figures are redrawn from Ref. [27].

packing is not efficient: gaps between the coordinating atoms emerge. For $R = 1$, again, packing is efficient with $N = 6$. Figure 2-3b shows the dependence of the coordination number of efficient packing N on radius ratio in three dimensions [27].

The simple model in Figure 2-3a assumes a structure in which every solute atoms is completely surrounded by solvent atoms. This, of course, only holds for binary glasses with high solvent concentrations. In multi-component glasses with low solvent concentrations, it is likely that the coordinating shell of a centre atom contains atoms of all species. This is accounted for in a later work of Miracle *et al.* on Partial Coordination Numbers (PCNs) in the MG model structure [28]. Having included atoms of different sizes in the first neighbouring shell, the effective radius ratio becomes

$$\tilde{R}_i = r_i/\bar{r}_i^{\,s}$$

where r_i and $\bar{r}_i^{\,s}$ are the atomic radius of the centre atom and the mean atomic radius of the atoms in the coordinating shell, respectively. The model further assumes that the atomic fractions within a cluster fully reflect the macroscopic composition. The atomic fraction of any constituent i in the coordinating shell of a cluster is thus different from the macroscopic composition c_α. According to Ref. [28], the partial coordination number of element j around a centre atom of type i is given as

$$N_{i,j} = \begin{cases} \left(N_{i,\text{tot}} + 1\right)c_j \text{ for } i \neq j \\ \left(N_{i,\text{tot}} + 1\right)c_j - 1 \text{ for } i = j \end{cases},$$

where $N_{i,\text{tot}}$ is the total coordination number around an i atom. The atomic fraction of any species j in the coordinating shell around an i atom, $c_{i,j}^{\,s}$, thus becomes

$$c_{i,j}^{\,s} = \frac{N_{i,j}}{N_{i,\text{tot}}}.$$

With Equation 2-2 and Equation 2-3, the mean atomic radius of the atoms in the coordinating shell $\bar{r}_i^{\,s}$ can be expressed as

$$\bar{r}_i^{\,s} = \bar{r} + \frac{\bar{r} - r_i}{N_{i,\text{tot}}(\tilde{R}_i)},$$

where $\bar{r}$ is the mean atomic radius of the alloy. Equation 2-4 is thus implicit for $\bar{r}_i^{\,s}$ and may be solved by iteration, using $\bar{r}_i^{\,s,0} = \bar{r}$ as a

starting value.

It has been further suggested that not only are the atoms efficiently-packed into clusters, but that the clusters themselves are efficiently packed into medium-range order (MRO). Cluster arrangements of *fcc* and *bcc* type [29], icosahedral type [30] or fractal type [31] have been suggested. Naturally, not every atom is centring an effectively packed typical local motif. As we learn from molecular dynamics (MD) simulations [32], the atomic structure is highly heterogeneous. Besides the typical, dominant motifs (which in fact agree for MD [33] and efficient-local atomic packing ELAP [27], namely 12-fold coordination around Cu and 16-fold coordination around Zr in binary $Cu_{64}Zr_{34}$), many atoms sit in configurations that are topologically unfavourable; see for example the cluster in Figure 2-2 marked red, with a very low coordination number (3).
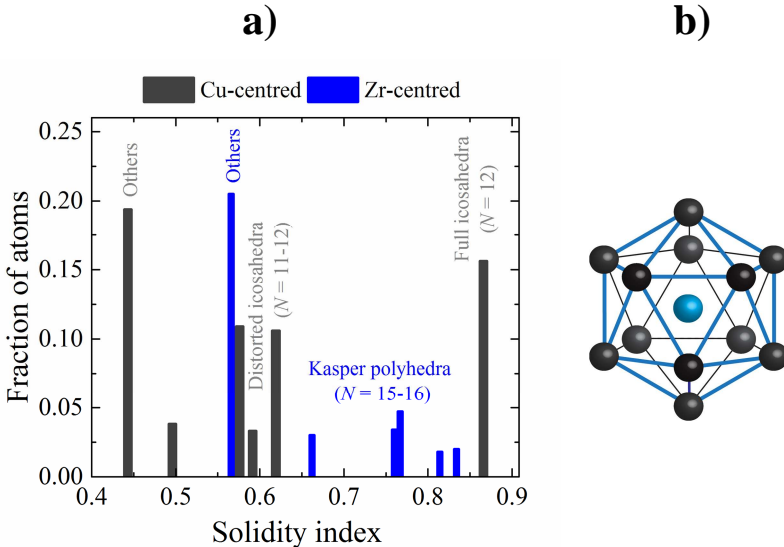
a)   **b)**

Figure 2-4: a) Dominating structural motifs in a Cu–Zr binary alloy according to MD simulations [34], (b) schematic of an icosahedron.

The structural heterogeneity within the glass is explored in an MD work by Ding *et al.* [34], attributing to each cluster a value for its "solidity", a term quantifying how elastically it reacts to small outer stresses (Figure 2-4a). Clusters with a high solidity behave "solid-like", meaning that they are effectively carrying elastic loads. Ding *et al.* find that most Cu atoms are coordinated in icosahedrons (12-fold coordination, Figure 2-4b), i.e. in a very dense and thus stiff coordination. However, the second largest group consists of Cu atoms in most liquid-like, compliant configurations. For Zr atoms, the case is less pronounced, but nevertheless, Kasper-polyhedrons (16-fold coordination) and slight distorted variations thereof make up a dominant fraction of Zr-centred clusters.

Taking these aspects into account, the MG structure can be simplified by imagining a rigid backbone of interconnected, efficiently packed clusters, which encloses islands of atoms in topologically

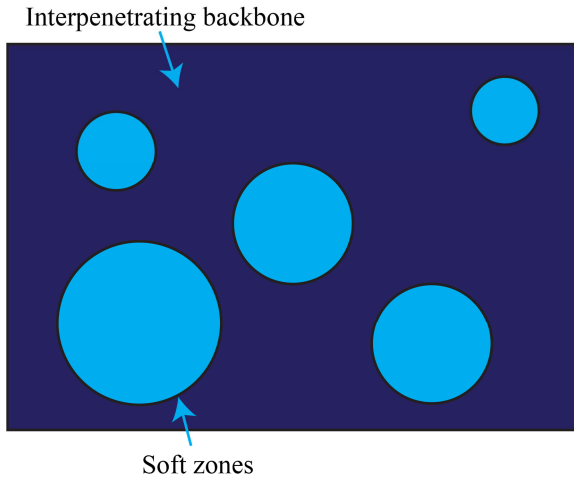Interpenetrating backbone

Soft zones

Figure 2-5: Illustration of the dual metallic glass structure: Interpenetrating backbone consisting of densely packed typical motives, enclosing islands of reduced density.

less favourable configurations. Such a picture of soft zones within a hard matrix is wide-spread in literature, appearing under the names of, for example, solidity and liquidity [34], liquid-like phases or cores [35, 36], atomistic free volume zones [37], nanoscale mechanical heterogeneities [38], soft spots [39], or zones enriched in Geometrically Unfavourable Motifs (GUMs) [13]. A typical representation is shown in Figure 2-5, and is supported by studies on medium-range order [31, 40].

2.4.   General mechanical properties

Having gained a state-of-the-art understanding of MG structure, we now turn our focus towards mechanical properties. Mechanical properties describe the reaction of a material to externally applied loads and displacements. Even at small loads, some of the induced deformation will be non-elastic. In conventional alloys, carriers of such inelastic, or at least anelastic processes are easily identified: dislocations and vacancies. For the glass, no obvious equivalent units can be directly inferred from Figure 2-2. However, zones of decreased density in glasses bear some similarity with vacancies in crystals. This similarity is the basis of the MG deformation model by Spaepen [41], which states that deformation in glasses is carried by diffusive, stress-assisted atomic jumps, promoted by zones of low density, or analogously, zones of increased *free volume* (FV), where free volume is defined as the difference between available volume and minimum required volume (hard-sphere volume) per atom (Figure 2-6a). However, experiments mimicking atomic mechanics using bubble rafts [42] soon revealed that diffusive atomic jumps' cannot be the dominant deformation mechanism in metallic glasses Still, zones of increased free volume remain important, but, instead of hosting stress-assisted atomic jumps, they were
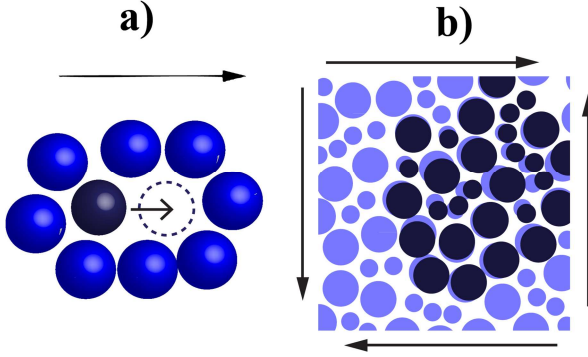
Figure 2-6: Two mechanisms for inelastic deformation in MGs: a) an atomic-Free Volume jump and b) a Shear-Transformation (STs), with the rearranged configuration drawn as an overlay in dark blue.

found to facilitate stress-induced shear rearrangements of groups of 20 to 100 bubbles (atoms) (Figure 2-6b). Such a rearrangement process is termed a Shear Transformation (ST). Notably, an ST is only defined by its transience, and can thus not be sketched into a static structural representation like Figure 2-2. Interestingly, identifying the atoms that will eventually undergo an ST *a priori* is so far not even possible in computer simulations [43]. Nevertheless, such groups of atoms which are prone to shear rearrangement are mainly used to model mechanical behaviour. These theoretical entities are called Shear-Transformation Zones (STZs) [44]. While it is tempting to directly connect these STZs to the soft spots in Figure 2-5, such equivalence, even if anecdotal, has not yet been proven. In the chapter about inhomogeneous flow of MGs (chapter 1), we will go into the matter of STZ and FV modelling in more detail. Prior to that, however, general aspects of MG mechanical properties are reviewed, following the sequence of a mechanical test, i.e., the elastic properties are reviewed first, then yielding is discussed, and finally post-yielding behaviour, the main subject of this thesis, is introduced and examined in more detail in chapter 3.

2.4.1. Elastic properties

The elastic regime of metallic glasses is characterized mainly by a relatively small elastic modulus and a large elastic limit of generally 2-3% [5]. This combination of properties makes possible a high maximum energy-storage density, which is proportional to the resilience $R_s = \sigma_y^2/E$, where σ_y is the yield stress and E is the Young's modulus. This makes MGs very attractive for applications such as watch springs [45] or sports goods [9]. Table 2-1 compiles elastic constants (Young's modulus E, shear modulus G, bulk modulus

Table 2-1: Mean values Young's modulus E, shear modulus G, bulk modulus K, Poisson's ratio v of MG alloys with various base metals, based on the data set from Ref. [46]. G_0 is the shear modulus of the base metal.

	E (GPa)		G (GPa)		K (GPa)		v	G_0 (GPa)
Zr-	91	± 1	33	± 5	109	± 6	0.359	33
Cu-	92	± 7	34	± 3	116	± 8	0.367	48
Mg-	53	± 3	20	± 1	48	± 3	0.314	17
Fe-	195	± 19	75	± 7	180	± 17	0.317	82
Ti-	100	± 5	37	± 2	112	± 3	0.355	44
Pd-	96	± 8	34	± 3	170	± 8	0.405	44
Pt-	95	± 1	34	± 1	200	± 2	0.421	61
Ni-	107	± 1	46	± 10	166	± 41	0.369	76
Co-	232	± 20	93	± 1	220	± 6	0.315	75
Ca-	25	± 6	10	± 2	20	± 5	0.294	7.4
Sr-	20	± 2	8	± 1	16	± 1	0.290	6.1
Hf-	115	± 2	43	± 1	129	± 1	0.351	30
Au-	74.4		27		132		0.400	27
Ce-	33	± 3	13	± 2	32	± 2	0.328	14
La-	35	± 4	13	± 2	38	± 3	0.347	14
RE-	59	± 15	23	± 6	55	± 12	0.321	20-30

K, Poisson's ratio *v*, and shear modulus of the base metal G_o) for MG alloys with different base elements, measured using the ultra-sonic method. The underlying dataset is taken from Ref. [46]. MGs have been reported to effectively inherit their elastic moduli from the base metal [47]. That this happens in spite of the different amorphous structures (SRO) also underlines the strong significance of chemistry (bond strengths) for the mechanical properties of the MGs. The relation of the elastic constants of base metal with those of glassy alloys is shown in Figure 2-7. The data set originally used in Ref. [47] (squares) is extended with values from Ref. [46] (circles). It is noted that the effect of inheritance is less pronounced if the data of Ref. [46] are included.

As mentioned at the beginning of this section, non-elastic processes have been reported even within the macroscopically elastic regime. Among these is the occurrence of a mechanical hysteresis
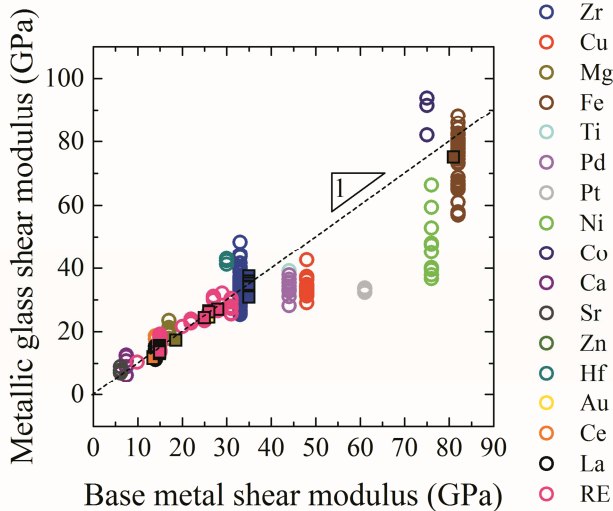

Figure 2-7: Shear-modulus inheritance in MG alloys. Data from Refs. [47] (squares) and [46] (circles).

upon cyclic loading crossing zero stress [48]. A more special form of such a cyclic-loading test is Dynamic Mechanical Analysis (DMA), where a sample is subjected to low-load excitation at different temperatures and frequencies, revealing a significant dissipative process for some MGs clearly below the glass transition temperature [49-53]. Occurring below temperatures where the α-relaxation is dominant, this process is called β-relaxation. It is brought into correlation both with the soft spots of Figure 2-5 and with STZs directly [53]. The latter is due to a size match of beta-relaxation activation energies and model calculations for the energy barriers of ellipsoid STZs. However, it has also been reported that the shape of these β-relaxations may be more reminiscent of atomic chains than ellipsoids [54].

2.4.2. Yielding

Yielding of MGs has been thoroughly investigated by Johnson and Samwer [7]. Their starting point was the expression for the rearrangement energy of an STZ at zero stress (W_{STZ}), originally introduced by Eshelby [55]:

$$W_{\text{STZ}} = (8/\pi^2)G\gamma_c^2\zeta\Omega,$$

Equation 2-5

where G is the shear modulus of the glass, γ_c is the critical yield strain, ζ is a geometric correction factor and Ω_{STZ} is the STZ volume. Modifying this expression to include stress dependence, the authors determined the temperature at which thermal energy and stress-dependent energy match, and by this derived a universal expression for yielding of MGs:

16

$$\tau_c = G\left(\gamma_1 - \gamma_2\left(T/T_g\right)^{\frac{2}{3}}\right),$$

<div align="right">

Equation 2-6

</div>

where τ_c is the critical shear stress, T is the thermal temperature and T_g is the glass-transition temperature, and $\gamma_1 = 3.6\%$ and $\gamma_2 = 1.6\%$ are constants. Because the model treats the glass as an iso-configurational solid, the "Johnson-Samwer" stress might be interpreted as the shear stress at which configurational break down occurs. Critical shear stresses of different glasses at different temperatures can be fitted very well by that model, also revealing an almost constant yield strain of 2.7%. The authors acknowledge some scatter in that value, as they are aware of reports that the yield strain increases slightly with an increase in temperature [56].

In the context of critical stresses, compression-tension asymmetry has been reported. MGs are slightly stronger under compression than under tension. This behaviour was modelled by both Mohr-Coulomb [57, 58] and Drucker-Prager [59] formalism. In contrast to simple Tresca or Von-Mises yield criteria, these models can explain the stress-state dependent fracture angle, i.e. 56° in tension compared to 43° in compression [60]. Weibull statistics on the peak stress of MGs have also been evaluated [61], showing values of 25-75, indicating that the mechanical performance of MGs is flaw insensitive. In fatigue experiments, MGs show fatigue limits relative to the uniaxial strength which are comparable to conventional polycrystalline alloys [62, 63].

2.4.3. Post-yielding behaviour

Post-yielding, or flow behaviour of MGs, is highly dependent on temperature and strain rate [41] (Figure 2-8). Close to and above T_g, the flow of MGs is homogeneous, meaning that plastic defor-
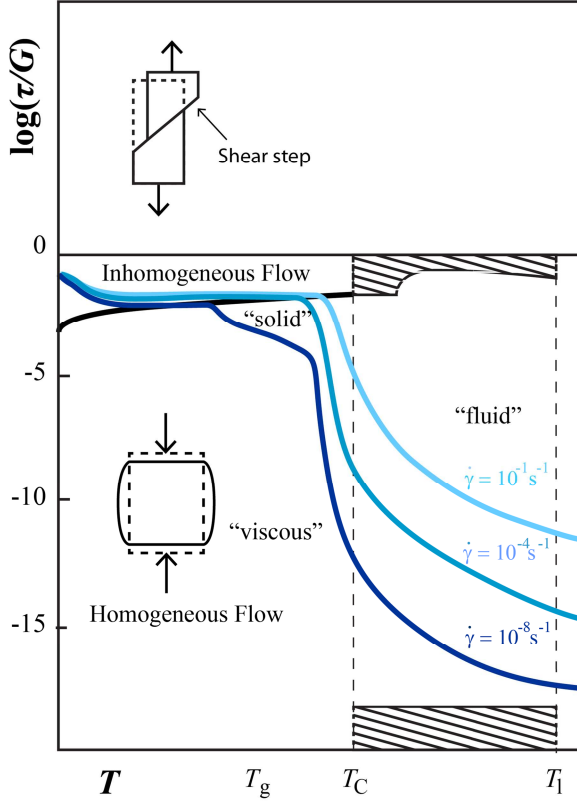
Figure 2-8: Metallic glass deformation map redrawn from Ref. [41].

mation is distributed equally over the sample volume. Even super-plastic behaviour has been reported [64], raising the prospect of advanced processing via thermoplastic forming [65]. In the context of mechanical properties for applications, however, sub-T_g flow behaviour is more relevant. At these temperatures severe flow localization is observed. Deformation is no longer homogeneous, but highly concentrated within thin layers of weakened material: the shear-bands. Plastic strain is accumulated by the generation of macroscopic shear steps at the sample surface (upper sketch in

Figure 2-8). More details regarding shear bands is provided in the next chapter.

Compared to the superplastic behaviour above T_g, the amount of plasticity observed in the inhomogeneous regime is lower, and moreover strongly dependent on both extrinsic and intrinsic factors (Table 2-2). Among extrinsic influences, the stress state in particular is of great importance. Plastic behaviour is restricted to loading conditions other than tension, where mode-I crack opening has been suggested as a probable cause of brittle failure [11]. Recent work has highlighted the possibility of improving tensile ductility by introducing complex stress states using pores, notches or other strategies of advanced geometric design [66-68]. Another external factor strongly influencing mechanical behaviour is temperature. Malleability, the correct term for compressive plasticity according to Schuh [69], depends on temperature in a highly non-linear way (Figure 2-9). While brittle at liquid helium temperatures [70, 71], the greatest inhomogeneous plasticity is reported at temperatures of liquid nitrogen [72]. Before reaching the superplastic regime at and above T_g, brittle behaviour is again observed at and around room temperature [73]. In addition to temperature embrittlement, authors report embrittlement with increasing diameter [74, 75] and decreasing system stiffness [76]. This is generally explained by the reaching of too high temperatures within the shear band, because the amount of dissipated energy per area within the glass is increased [74, 77, 78]. Addressing intrinsic factors, a very prominent correlation between plasticity, or equivalently toughness, and the Poisson's ratio ν has been reported, both within [79-81] and among different MG systems [82] The Poisson's ratio is believed to represent the materials' preference for shearing over cracking [46]. In crystalline alloys, where toughness is linked to dislocation dynamics, the ratio of shear- to bulk-modulus, G/K,
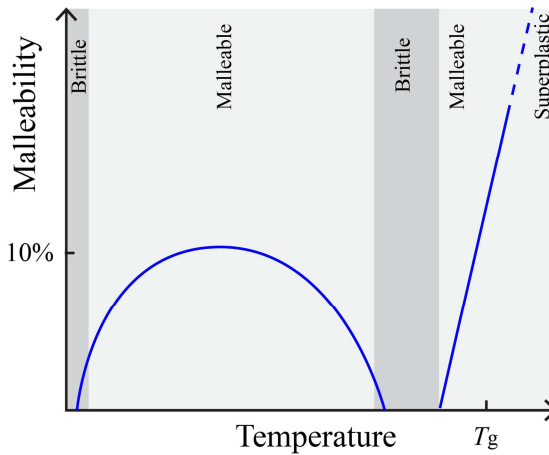
Figure 2-9: Schematic plot of MG malleability as a function of thermal temperature.

is a monotonically decreasing function of v [83]. If v is small enough, spontaneous emission of dislocations from crack tips is possible. This causes the cracks to blunt and thus toughens the material [83].

Table 2-2: Extrinsic and intrinsic factors affecting MG plasticity.

Factor	Symbol	Plasticity promoted by...	Ref
Extrinsic			
Stress-state		Compression, bending	[11]
Testing temperature	T	Low T	[72, 73]
Setup stiffness	k	High stiffness k	[75, 76,
Sample diameter	d	Small d	84]
Intrinsic			
Poisson's ratio	v	High v	[82, 85]
Elastic ratio	K/G	Large K/G	[46]
Free volume	v_f	Much v_f	[86]
β-peak shape		Pronounced peaks	[54]
STZ volume	Ω_{STZ}	Large Ω_{STZ}	[87]

A corresponding derivation for the amorphous case does not yet exist. In addition to the Poisson's ratio criterion, other intrinsic factors which determine plasticity have been suggested. Among them is the free volume content [86], STZ volume [87], or the shape of the mechanical β-relaxations in DMA measurements [54]. None of these three theories, however, is as often used as the Poisson's-ratio criterion.

Details on *how* plastic flow is accumulated within the inhomogeneous deformation regime follow in the next chapter. Before that, we will conclude our overview on mechanical properties with a short section on metallic glass fracture.

2.4.4. Fracture

In uniaxial mechanical tests, the final fracture of MG specimens takes place on a plane tilted with respect to the load axis by ca. 43° in compression and 54° in tension [60]. Figure 2-10 shows a schematic of a typical fracture surface obtained in a compression test. The part of the surface generated incrementally by stable shear-band flow, i.e. the shear-step surface, is smooth, while the remaining surface, generated during final fracture, features the so-called vein-pattern morphology, which represents a "variant of the ubiquitous fluid-meniscus instability" [88], meaning that it is a typical example of a liquid-layer fracture. A scanning electron microscopy (SEM) picture showing both types of fracture surface adjacently is also given in Figure 2-10. The time scale of fracture in millimetre-sized specimens has been reported to be 12.5 µs at most [89]. Infra-red (IR) thermography has revealed instantaneous melting at the moment of fracture [90]. In mechanical tests at very high loading rates, a change of fracture-surface morphology from vein-pattern to corrugated pattern [91] has also been reported.
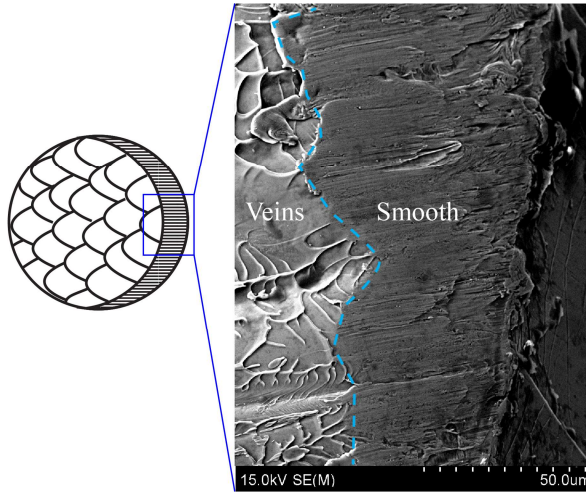
Figure 2-10: SEM image of a typical fracture surface of an MG sample that has accumulated some plastic deformation prior to fracture. "Vein-patterns" mark the surface of the final fracture, whereas a smooth pattern is found on the surface of shear steps generated by stable plastic flow.

3. Overview on inhomogeneous flow

"Metallic glasses are not necessarily hot."

K. Slaughter

In the preceding chapter, we learned about MG structure, general mechanical properties, yielding models, the difference between homogeneous and inhomogeneous deformation, and about the prospects and limitations of metallic glass plasticity. In this chapter, we will concentrate on inhomogeneous flow in MGs, meaning flow carried by shear bands. We will first describe the state-of-the-art understanding of flow localization; then we will take a closer look at the shear bands themselves, present the phenomenology of strain-rate and temperature-dependent flow behaviour, review different perceptions of how plastic strain is accumulated by shear bands, and finally look at the most popular atomistic models which address MG flow in detail.

3.1. Flow localization

According to common perceptions, flow localization in MGs is a consequence of strain-softening, associated with structural rejuvenation (dilatation) [69, 92]. Strain-rate perturbations, easily annihilated by negative feedback in strain-hardening materials, become self-propelling in the purely strain-weakening MGs. The perturbation spreads and eventually develops into a system-spanning instability: the shear band. From an STZ perspective, flow localization occurs once the flipping of an isolated STZ causes changes in

the elastic far-field stress which are great enough to trigger neighbouring STZs. As a consequence, an STZ-cascade can propagate through the material [93].

3.2. Shear bands

Shear bands are not unique to MGs. They are also reported in crystalline metals [94], polymers [95], soils [96, 97], granular media [98] and colloids, etc. [99] .

3.2.1. Appearance

A main feature of MG shear bands is their very small thickness. Electron microscopy studies on plastically deformed MG samples reveal them as deformation lines with thicknesses of 10-20 nm [100-102]. While the shear band itself is thus invisible to the naked eye, when it operates it causes a shear step (or shear offset) Δu_{pl} on the surface, which can easily become several hundreds of microns large (Figure 3-1a).

Schematic illustrations of shear bands and the macroscopic shape changes they cause are shown in Figure 3-1b and c. While
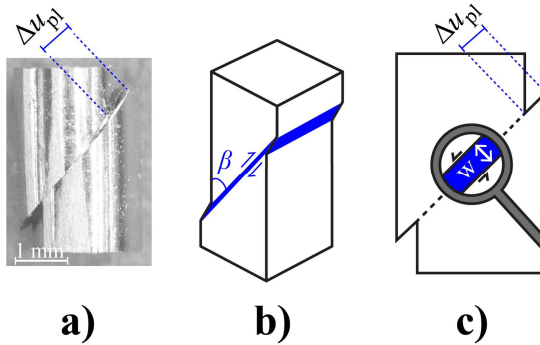

Figure 3-1: a) Metallic glass cylinder deformed on a major shear band; b) illustration of a shear band in tension, redrawn from [103]; c) schematic representation of a), indicating shear-band width w and shear offset Δu_{pl}.

plastic deformation is typically concentrated on one major shear band in a monolithic glass under compression, multiple shear banding, meaning the formation of a network of intersecting shear bands each contributing equally to plastic deformation, has been reported for constrained or complex geometries [67, 68, 75, 104], in the presence of large residual stresses [105, 106] and in MG composites [107, 108].

3.2.2. Shear-band structure

In terms of atomic structure, shear bands differ considerably from the matrix material. A first indication of this was the observation of shear bands' reduced resistance to chemical etching, which was attributed to a decrease in topological and/or chemical short-range order [11]. Recently, sophisticated *in-situ* acoustic emission (AE) [109] and transmission-electron microscopy (TEM) [110, 111] studies have allowed a quantitative assessment of the structural changes associated with shear banding, reporting density changes from -1 to -2% [109, 110] and -10 to +6 % [111]. A decrease in structural order within the shear band is also observed in MD simulations. Fig3-2a shows how the fraction of different Cu-centred structural motifs changes with strain for a Cu–Zr binary MG [112]. At the yield point, where a shear band is initiated (ca. 7% strain – a typical value for simulations), the fraction of the dominant motif (full icosahedrons) is reduced from 25% to 15% at the cost of an increased fraction of fragmented, meaning inefficiently packed, clusters. The fractions of other species do not markedly change with strain. Figure 3-2b shows how the full-icosahedra fraction changes along a line that intersects the shear band [113]. A drop from 20% in the matrix to about 15% in the shear band is found.

In experiments and MD simulations, annealing treatments have been shown to heal the structural differences between matrix and
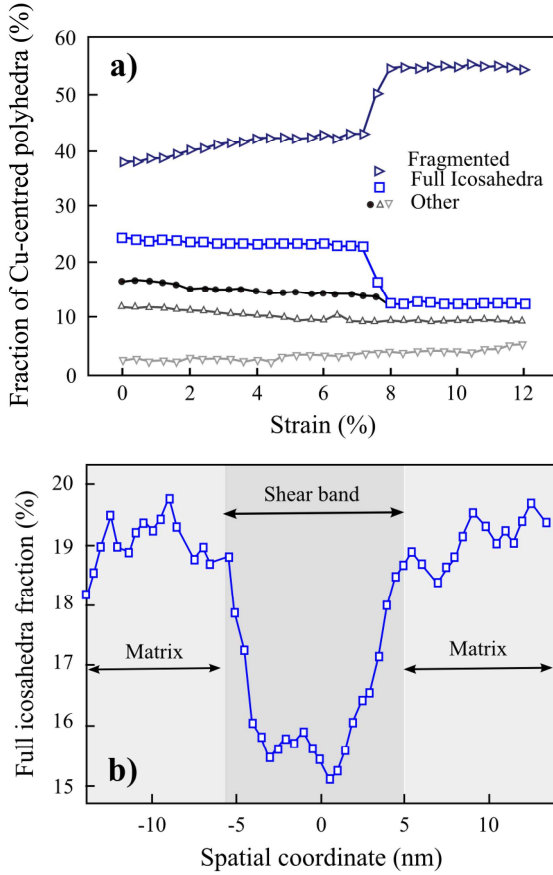
Figure 3-2: Reduction of short-range order in the shear band as a function of strain (a, [112]) and of space coordinate *x* (b, [113]); redrawn from the original publications.

shear-band material. While this is observed directly from full-icosahedra fractions recovering to matrix values in the simulations, it is experimentally captured by the erasing of the etching susceptibility of the shear bands [11].

3.3.   Flow curves: serrated vs. non-serrated flow

The shape of compressive flow curves shows a strong dependence on temperature and applied strain rate. At low temperatures and high strain rates, flow curves are smooth (black curve in Figure 3-3), with a stress overshoot preceding the reaching of steady-state flow stress. At high temperatures and low strain rates (blue curve in Figure 3-3), flow curves show discontinuities, better known as serrations. A typical serrated-flow curve can be divided into three regimes [114, 115]: an elastic regime (1), a transition regime (2) and a purely plastic regime (3). In the transition regime (2), stress increases with strain at a rate lower than in the elastic regime and first serrations, irregularly shaped and spaced, indicate the onset of plastic deformation.
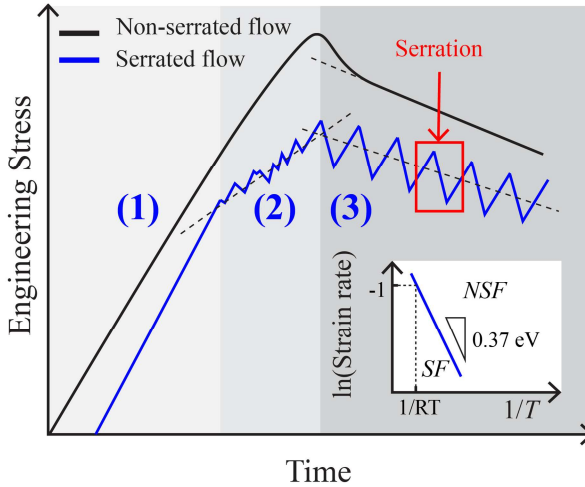

Figure 3-3: Non-serrated (NSF, black) and serrated (SF, blue) flow curves, with (1) indicating the elastic regime; (2) indicating the transition region and (3) revealing the purely plastic regime. The red box indicates a single serration. The inset shows the Arrhenius-type behaviour of the temperature- and strain-rate dependent flow transition (see also Figure 3-8).

Because no strain-hardening mechanism is known for MGs, the transition behaviour is also described as "apparent strain hardening", believed to reflect a geometrically constrained situation, in which some parts of the sample start to deform plastically, while others are still loaded elastically. The purely plastic regime (3) is characterized by regularly spaced and sized serrations with a stress level that either plateaus or slightly decreases with strain.

The transition serrated- and non-serrated flow is described well by an Arrhenius function [116, 117] with an activation energy of 0.37 eV [117] for a Zr-based BMG (inset in Figure 3-3). Shear-band properties can be derived from both serrated and non-serrated flow curves. How this is accomplished is described in the following.

3.3.1. Serrations

Figure 3-4 schematically shows the load and displacement signal versus time for a sequence of three serrations. An individual serration consists of a slow elastic loading stage (light grey area) and a fast plastic slip stage (darker grey area), during which, over the slip duration Δt, load drops by ΔF and plastic strain is generated. The
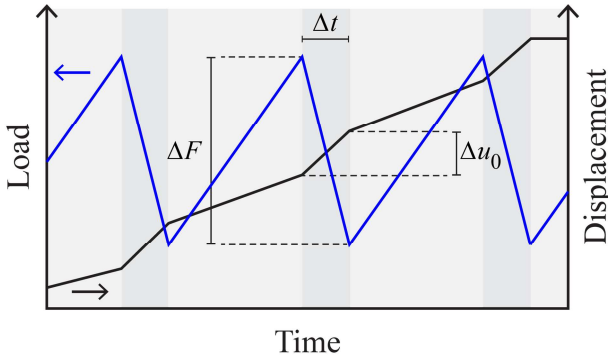

Figure 3-4: Schematic load and displacement signals as a function of time for a sequence of three serrations. A serration is characterized by the drop size ΔF, the duration Δt and the apparent displacement jump Δu_0.

load drop ΔF is typically on the order of 1-2% of the peak load. For each stress drop, there is a corresponding jump Δu_o in the displacement signal (Figure 3-4, black line). For the obvious similarity to stick-slip friction phenomena, the slow loading phases and the fast unloading phases have been referred to as "stick" and "slip" stages, respectively [118].

If flow serrations truly reflect shear-band properties, Δu_o has to be directly related to plastic deformation, i.e. to the size of the emerging shear offset Δu_{pl}. Georgarakis *et al.* [119] found that the sum of displacement jumps $\sum \Delta u_0$ strongly underestimates the total plastic strain. From this they concluded that serrations are rather a measuring artefact than a direct cause of intrinsic material behaviour. In contrast, more recent research has revealed that Δu_o in fact *is* directly related to Δu_{pl}. However, the interplay between glass sample and testing setup must be properly accounted for [120]. To this end, Figure 3-5a shows the load and displacement signal versus time for one serration, and Figure 3-5b and c show the sample-machine assembly at the times 1) and 2) indicated in a),
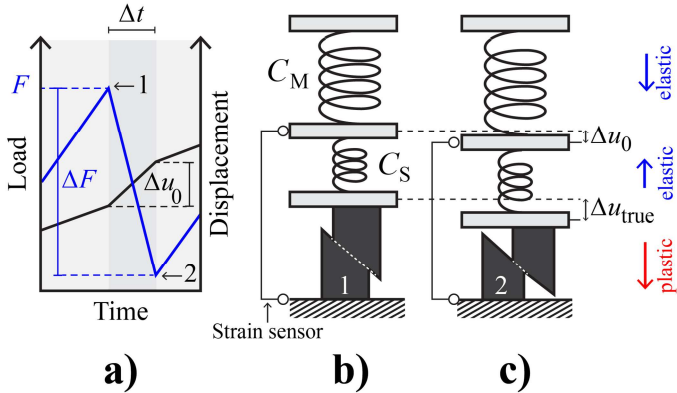

Figure 3-5: Interplay between sample and testing setup during the slip phase of a serration in a quasi-static compression test.

i.e. prior to and shortly after the slip phase of the serration. Here, C_M and C_S refer to the compliance, meaning the inverse stiffness, of machine and sample, respectively. At peak load F (1), both machine and sample are elastically deformed to a displacement $u_{M,S} = FC_{M,S}$. After the slip event (2), load has dropped by ΔF. Under quasi-static conditions, meaning that the plastic deformation rate is much higher than the applied strain rate, the drop in load causes the machine to expand elastically by $\Delta u_0 = \Delta F C_M$. On the sample side, Δu_o is balanced not only by a plastic contribution emerging from the sample shortening ($\Delta u_{true} = \Delta u_{pl}/\sqrt{2}$), but also by an elastic-recovery contribution of the sample, which equals to $\Delta F C_S$. Just like the machine, the sample expands elastically due to the decreased load level. The displacement balance thus reads: $\Delta u_0 = \Delta u_{true} - \Delta F C_S$. Rearranging and accounting for the shear-band angle of typically 45°, the shear-step size Δu_{pl} can be expressed as a function of the apparent-displacement jump Δu_o:

$$\Delta u_{pl} = \sqrt{2}(\Delta u_0 + \Delta F C_S) = \sqrt{2}\Delta F(C_M + C_S) .$$

Equation 3-1

In other words, the registered displacement jump Δu_o reflects only the elastic recovery of the leverage of the testing machine due to the dropping load. Under quasi-static test conditions, this length change is equal to the difference between true plastic deformation and the elastic recovery of the sample. It is noted that the second term in Equation 3-1 was neglected by Georgarakis *et al.* [119] and that its omission may be the true reason for the above mentioned mismatch between the sum of flow-curve strain increments and the total shear-step sizes. Since it has been shown that every serration in the plastic regime of a serrated flow curve corresponds to the initiation, propagation and arrest of a single shear

band [120], Equation 3-1 directly connects the serrated flow signal to the behaviour of individual shear bands.

In addition to the length change, high-acquisition rate instrumented mechanical testing also allows one to determine of the time scale Δt during which the shear offset is generated. It is noted that piezo-cells should be used for the recording of fast events, because conventional load cells show some delay in reacting to dynamic, fast load changes, and may thus strongly overestimate the serration-time scale. Properly instrumented, one can thus determine the load drop ΔF, displacement jump Δu_o and event duration Δt directly from serrated flow curves.

3.4. Models of plastic-strain accumulation

Because shear bands are as thin as 10 nm [100], initiate at locations which are difficult to predict, and operate intermittently for short durations only [118, 121], *in-situ* investigation of the accumulation of plastic strain in metallic glasses (MGs) is a challenging task. It is thus not surprising that since the first reports on the mechanical behaviour of MGs [48], different perceptions have emerged as to the exact mechanism by which shear steps are generated. This is not trivial, because the choice of a specific model has immediate consequences for the estimate of shear-band properties that are not directly measured experimentally, such as the speed at which the shear step is generated (the shear-band velocity v_{SB}), the shear-band viscosity η_{SB} and the temperature rise during shear-band operation ΔT. Figure 3-6 illustrates the four most important models of shear-step generation. These models are labelled as (1) phonon-shear-front propagation, (2) serration- shear-front propagation, (3) serration-transient behaviour, and (4) serration-simultaneous shear. The implications of these models for the event
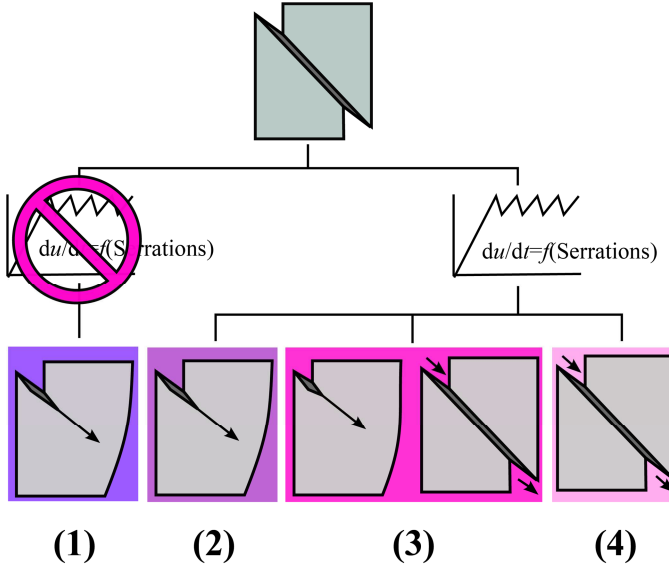
Figure 3-6: Postulated modes of shear-step generation. (1) front-propagation at sound velocities, (2) front-propagation at time-scales obtained from serration analysis, (3) front-propagation changing to simultaneous shear once a major band is established and (4) simultaneous shear.

duration t, the temperature jump ΔT, shear-band velocity v_{SB} and viscosity η_{SB} are summarized in Table 3-1. All these models assume that only one single dominant shear band is operating at a time. The four different scenarios are now presented in detail.

Table 3-1: Event duration t, shear-band velocity v_{SB}, temperature jump ΔT, shear-band viscosity η_{SB} for the four different models. η_{SB} was calculated via $\eta_{SB} = \tau w / v_{SB}$ with the shear stress $\tau = 1$ GPa and $w = 10$ nm.

	t (s)	v_{SB} (m/s)	ΔT (K)	η_{SB} (Pas)	Refs
Model (1)	10^{-8}	10^{3}	1000	10^{-2}	[119], [78]
Model (2)	10^{-3}	1	90	10	[122]
Model (3)	10^{-3}	10^{-3}	3	10^{4}	[123]J
Model (4)	10^{-3}	10^{-3}	3	10^{4}	[124]

3.4.1. Model (1): challenging instrumented testing

As mentioned above, some authors challenge the perception of serrated-flow observables Δu_o and Δt as being physically meaningful [78, 119]. Acknowledging that a shear band cannot be formed instantaneously, they attribute both the generation of the shear band *and* the formation of the shear step to the propagation of a dilating shear wave that travels through the sample at a fraction of the speed of sound (model (1) in Figure 3-6). When taking into account the presence of a stress-redistribution field around the shear front, the time for the generation of a shear step of 1 μm size then amounts to 10^{-8} s. This led the authors to predict temperature rises of thousands of K within the shear band [119]. Such high values would explain reports of the establishment of a micron-sized heat-affected zone around the shear band [125] and of shear banding which causes the melting of fusible tin coatings on top of an emerging shear step [126]. This scenario is an integral part of the model of Miracle *et al.* regarding the size effect in MG ductility [78]. However, a recent study [127] has revealed that melting of a tin coating is not universally observed in MG deformation, but is rather a function of alloy and stress state. This eliminates the condition that shear bands must "necessarily" be hot.

3.4.2. Models (2), (3) and (4), using serration time scales

In contrast to this phonon-based model, some studies report a direct link between the shear steps and features of the serrated-flow curves from instrumented mechanical testing [128, 129] (Figure 3-6 (2)-(4)). These models assume that the time scale of a single serration corresponds to the time scale of the coincident shear-step formation. Although models (2)-(4) agree on serration time scales, they differ in their understanding of how plastic strain is accumulated by a shear band. Model (2) assumes that the shear

step forms via a propagating front [122]. In other words, the full shear step is established behind the shear front, while the material ahead of the front remains undeformed. In this case, the shear-band velocity, i.e. the speed at which the shear step is generated, can be calculated as the ratio of the fully established shear band across the sample of diameter d and the serration time Δt, i.e. $v_{SB} = \sqrt{2}d/\Delta t$. In contrast, model (4) assumes that the shear step is established simultaneously along the shear plane [130]. In that case, it is the shear step only that is divided by the event duration in the calculation of the shear-band velocity, i.e.

$$v_{SB} = \Delta u_{pl}/\Delta t \ .$$

<div align="right">**Equation 3-2**</div>

These calculations provide shear-band velocities that are smaller by a factor of 10^3 than those calculated from model (2) for a sample of a few millimetres in diameter. Note, however, that the velocities calculated from model (2) are still three orders of magnitude smaller than those obtained from model (1). With high-speed imaging methods, Song *et al.* [124] and Wright *et al.* [131] directly observed the scenario of model (4) down to time scales of about 0.2 ms, i.e. a simultaneous deformation on the shear plane within their temporal resolution. They also did not resolve any delayed onset of shear banding on either side of the sample. The perception of sub-resolution intermittency, a necessity for reconciling the above-mentioned experimental finding with model (2), was also made unlikely by recent Acoustic Emission measurements [132], which revealed only one shear-band initiation signal per serration. From that perspective, scenario (2) should be discarded. Most recently, Joo *et al.* [123] carried out experiments using digital image correlation (DIC) on MGs under compression. The authors observed a transition from front-propagating behaviour of the shear

band in the early stage of deformation (associated with small strain increments only) to simultaneous shear in the subsequent stage, during which the large part of the total shear step is generated [123]. This is the scenario (3) in Figure 3-6. Similar results regarding a transition from a propagating to a simultaneous flow mode were obtained in a recent study by Qu *et al.* [133]. These authors report on shear steps that form via a propagating flow mode in the early regime of "apparent strain hardening", i.e. prior to reaching peak stress, and a transition to simultaneous shearing once a major shear band has formed. In a purely strain-weakening material, such as a metallic glass, events prior to reaching peak stress cannot be system-spanning and must thus be associated with local geometric constraints. From that perspective, we may deduce that scenario (4) is an idealized case of scenario (3) and shows an almost perfect elastic-to-plastic transition, devoid of geometrically-induced artefacts that would give rise to apparent front-propagating shear banding at pre-peak plastic strains. Initial apparent propagation thus appears to be related to stress-inhomogeneities within the MG samples rather than to a deformation mechanism according to model (2) in Figure 3-6b.

Shear-band initiation
$\Delta t = \mu s$

Shear-band propagation
$\Delta t = ms$

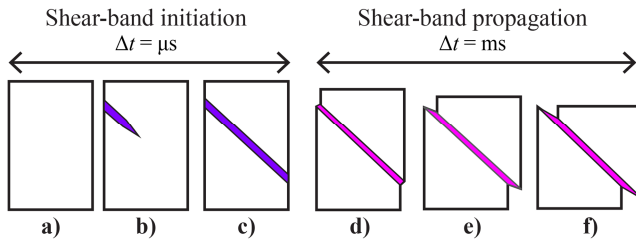a)   b)   c)   d)   e)   f)

Figure 3-7: Idealized shear-band operation. A shear band is initiated by a front-dilating shear wave (a-c). In this stage, only minor amounts of plastic deformation are accumulated. In the subsequent propagation phase (e-f), macroscopic plasticity is accumulated on shear bands by simultaneous shear.

Despite the fact that shear steps can be derived from serrations, there remains the necessity of an elastic wave that travels at a fraction of the speed of sound and effectively *generates* the shear band. According to current understanding there is no need for the time scale associated with shear-band initiation to be identical to the time scale of shear-step generation. In fact, a two-stage mechanism has been proposed which consists of a fast, front-propagating, phonon-controlled initiation phase, generating only a small step but causing structural rejuvenation of the whole band, followed by a slow, simultaneous shearing phase on the now weakened band, creating the major part of the step (Figure 3-7) [109, 118, 134].

3.5. Shear-band velocities and flow transition

Within the serrated flow regime, the shear-band velocity accor-
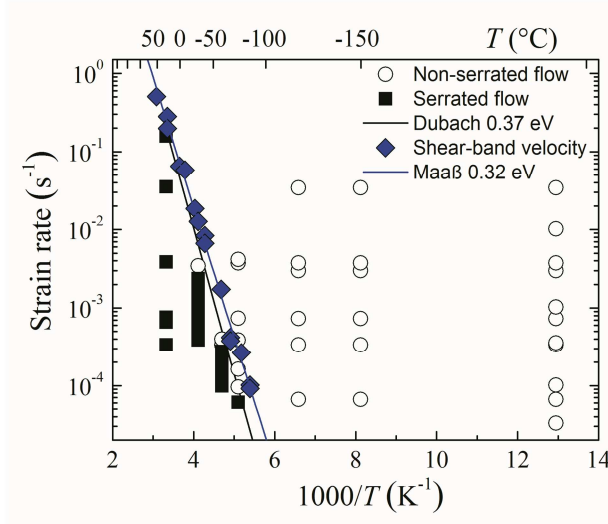

Figure 3-8: Flow transition from [117] vs. shear-band velocities from [120]. Temperature-dependent shear-band velocities represent the rates at which, if applied externally, the flow transition from serrated- to non-serrated flow would occur.

ding to model (4) (Equation 3-2) was found to be independent of applied strain rate [135]. In a Zr-based glass, shear-band velocities increase with increasing temperature, following an Arrhenius-type law with a barrier energy of 0.32 eV [120, 130]. This energy is very similar to the 0.37 eV obtained for the flow-transition. Defining an apparent shear-band strain rate $\dot{\varepsilon}_{SB} = v_{SB}/\sqrt{2}\,l$, where l is the sample length, we can plot the data sets from both experiments into the same figure (Figure 3-8), revealing a striking equi-valence of the two experiments. It appears that during a serration, a shear band accelerates until it reaches approximately that velocity which, if it were applied as an external rate, would cause the transition to non-serrated flow. In other words, non-serrated flow is observed if the applied strain rate exceeds the temperature-dependent shear-band strain rate. Below the flow transition line in Figure 3-8, shear-band velocities are independent of applied rate, causing serrations, and above the transition the shear band is driven at the applied rate. Note that this equivalence of shear-band velocity and the flow transition provides additional support to the perception of the simultaneous-shear mode.

3.6.   Properties from non-serrated flow curves

As opposed to those in the serrated flow regime, constant-strain rate tests in the non-serrated regime provide no direct insights into shear-band dynamics. Nevertheless, there is a means by which shear-band properties can be investigated in this regime, i.e. slide-hold-slide tests. In such tests (Figure 3-9), an MG sample is deformed to plastic strains at a constant rate. The drive is then set to zero and the shear band is allowed to relax. After a pre-defined waiting time, the drive is restarted. Prior to the re-establishment of the flow stress, a stress-overshoot $\Delta\sigma_a$ appears. Its size scales with the logarithm of the waiting time, representing an effect of struc-
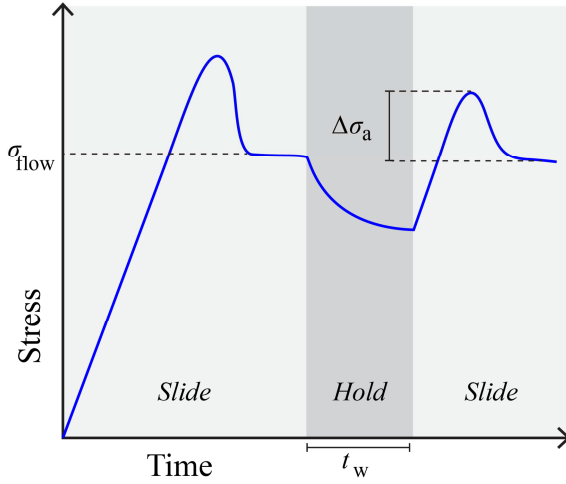
Figure 3-9: Schematic of a slide-hold-slide test in the non-serrated flow regime. The stress overshoot $\Delta\sigma_a$ is a measure of structural relaxation during the hold phase, i.e., waiting time t_w.

tural ageing [136]. In a Zr-based MG, the waiting time required to achieve a stress-overshoot of a given size follows an Arrhenius law as a function of temperature with an activation energy E_a of about 0.16 eV [137, 138]. This energy is associated with structural ageing, i.e. with the restoring of a quasi-equilibrium structure.

3.7. Size effects

To some extent, the flow behaviour of MGs depends on sample size. This short section is dedicated to these effects, which are discussed in descending order of the length scale involved.

Embrittlement in the mid-mm regime

The mechanical properties of MGs are typically studied via quasi-static compression tests on samples with diameters between 1 and 2 mm at ambient conditions, even if the alloys under investigation could be easily cast into larger dimensions. This is because

plastic deformability of MGs tends to decrease as sample size is increased. This size effect is attributed to the reaching of a critical energy-release rate during serrations, eventually causing shear bands to heat up to above a critical temperature which eventually causes structural disintegration [74, 77, 78].

Flow stabilization in the lower-mm regime

It has been reported that the critical strain rate for entering into the non-serrated flow regime decreases in smaller samples, meaning that flow in small samples is closer to stable than in large samples. This size effect is explained by the increased stiffness-per-area $k = 1/A(C_M+C_S)$ in small samples [139], causing partial stabilization of the serration instability.

Extreme ductility by aspect ratio effect

Figure 3-10a shows the plastic deformation of a metallic glass rod of an aspect ratio smaller than 1. At the yield stress (a), a shear band forms, but, oriented in 45° to the load axis, cannot span the sample, thus making only a limited contribution to a decrease in overall load. Moreover, shear offsets in this constrained setting cannot develop freely because they are directly arrested by the testing machine anvils. These constraints promote the initiation of
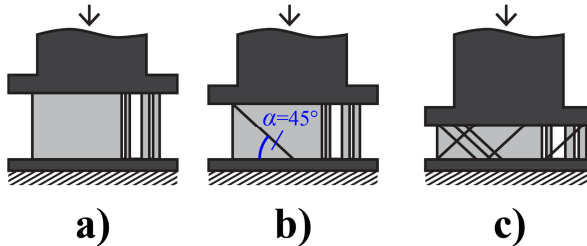

Figure 3-10: A sample of aspect ratio smaller than 1 is compressed (a). At the yield point (b), the first shear band initiates at the typical angle of 45°. The reactivation of the first shear-band is impeded by geometric constraints, necessarily generating multiple-shear banding (c).

multiple shear bands and lead to an increase in sample diameter, which is reflected in apparent strain-hardening flow curves and generates extremely high apparent ductility values [75].

Flow-mode transition at the nanoscale

A flow-mode transition from shear banding to homogeneous flow has been reported for micro-pillars of a size smaller than 100 nm [140, 141]. However, the disappearance of the shear-band mode has been challenged by other authors [142, 143], and thus requires further experimental verification.

3.8. Modelling of inhomogeneous flow

In this section we will look at how the phenomenology of MG flow can be explained in the framework of free-volume and STZ theory (see also Fig. 2-6).

The free-volume model was successfully used to fit the transition from homogeneous to inhomogeneous flow [41]. The transition is attributed to a change of mechanism at the atomic scale. Above the transition, free volume is provided by temperature, whereas below the transition, it is provided by stress. The focus of later modifications of free-volume theory was mainly to explain homogeneous flow. The Self-Consistent Dynamic Free-Volume (SCDFV) model, for example, allows the fitting of viscosity and strain rate-dependent flow stress of MGs at temperatures at and above T_g [144]. Concerning STZ modelling, homogeneous flow has similarly been investigated [145-147]. Only recently has STZ theory been explicitly applied to inhomogeneous flow of MGs [138, 139], particularly to resolving the origin of the transition from serrated to non-serrated flow. These two studies on inhomogeneous MG deformation are described in detail below, following a short introduction to the fundamentals of STZ theory.

3.8.1. Fundamentals of STZ modelling

STZs are "small regions [...] in special configurations, particularly susceptible to inelastic rearrangements in response to shear stresses" [44]. An STZ can only exist in one of two possible configurations, aligned with the principle stress orientations in the material, typically denoted "+" and "-". Triggered by external stress, an STZ can switch configuration, e.g., from "-" to "+". Thereafter, it is jammed and cannot carry further deformation in the "+" direction. Plastic flow is maintained, however, by the annihilation of jammed "+" states and the creation of new "-" configurations. The internal state variable in STZ theory is the dimensionless effective disorder temperature χ. Compared to the concept of free volume, it is here no longer the question of how much volume there is for a single atomic jump, but what configurational changes are possible for a group of atoms with the available free volume. The perspective therefore shifts from volume to entropy, and χ is connected to STZ density ρ_{STZ} via $\rho_{STZ} \propto \exp(-1/\chi)$. Note that in qualitative arguments, free volume and effective temperature might be used analogously. For example, in a glass produced by a very high cooling rate, levels of both free volume and effective temperature are high.

Within STZ theory, the mechanical behaviour of MGs is modelled using a set of three equations. The first links the plastic strain rate $\dot{\gamma}$ to the effective temperature [138]:

$$\dot{\gamma}t_0 = n_0 \exp\left(-\frac{E_{STZ}}{k_B T}\right) \exp\left(-\frac{1}{\chi}\right),$$

Equation 3-3

where t_0 is the inverse attempt frequency, n_0 is the typical number of atoms per STZ, T is the thermal temperature, and E_{STZ} is the stress-dependent STZ activation energy. The first exponential term represents the probability of an STZ rearrangement, while the sec-

ond exponential term takes into account STZ density.

The second equation describes the evolution of the effective temperature over time [138].

$$\frac{d\chi}{dt} = \frac{\dot{\gamma}\sigma}{c_0 \sigma_{\text{STZ}}} \left(1 - \frac{\chi}{\hat{\chi}(\dot{\gamma})}\right).$$

Equation 3-4

Here, c_o is an effective-temperature specific heat per unit volume, σ_{STZ} is the STZ yield stress, and $\hat{\chi}$ is the kinetically ideal value of the effective temperature. Equation 3-4 describes the tendency of the effective temperature to attain its kinetically ideal value $\hat{\chi}$, which, in agreement with simulations, is described as $\hat{\chi} = \chi_w / \ln(q_0 / \dot{\gamma} t_0)$. Two additional parameters emerge, i.e. q_o, a characteristic strain rate at which the steady-state effective temperature diverges and χ_W, a normalized energy scale determining the rate dependence. The material is rate-strengthening (i.e. it has a positive strain-rate sensitivity SRS) if $\chi_w > 1$, while it is rate-weakening for $\chi_w < 1$.

The third equation connects stress, displacement and velocity by the force balance on the shear band. It is often referred to as the machine equation [139]:

$$\frac{M}{A}\ddot{x} = \frac{1}{A(C_M + C_S)}(v_0 t - x) - \sigma,$$

Equation 3-5

where M is the inertia of the system, A is the cross-section area, $\ddot{x}$ is the vertical acceleration of the shear band, C_M and C_S are the compliances (i.e. inverse stiffnesses) of machine and sample, v_o is the applied velocity, t is the time, x is the vertical displacement, and σ is the stress.

Equation 3-3 to 3–5 are the tools for STZ modelling. It is with these tools that the inhomogeneous of metallic glasses can be flow phenomenologically explained. The starting point of the two studies which will be described in more detail below is the commonly supported assumption that stick-slip-like serrated flow is indicative of an underlying *negative* strain-rate sensitivity.

3.8.2.   Model I: Stable flow promoted by stiffness

In the first model, by Sun *et al.* [139], MGs are assumed to be purely rate-weakening materials ($\chi_w < 1$). The occurrence of stable, non-serrated flow is attributed to the suppression of stick-slip instability by stiffness. By performing a linear stability analysis on the steady-state solutions for effective temperature, stress and velocity, a temperature and strain-rate dependent critical stiffness per area k_{cr} is derived:

$$k_{cr}\left(v_0, T\right) = B\tau_c \left(\frac{k_B T}{W_{STZ}}\right)^{2/3} \ln(v_c/v_0) \,,$$

Equation 3-6

where B and v_c are constants, τ_c is the critical yield stress, W_{STZ} is the STZ barrier energy at zero load (in this model, W_{STZ} has been used as STZ activation energy E_{STZ} in Equation 3-3), and v_o is the applied driving rate.

Figure 3-11 schematically shows the dependence of k_{cr} on the applied strain rate. Perturbations decay exponentially over time for $k > k_{cr}$, causing flow to be non-serrated, while they develop into full-size serrations for $k < k_{cr}$, as indicated by the stress-rate trajectories in Figure 3-11b. The stiffness-dependent velocity v_{cr} at which the flow transition occurs, i.e. where $k_{cr} = k$, is obtained from Equation 3-6 as:

$$v_{\mathrm{cr}} = v_{\mathrm{c}} \exp\left(-\frac{k}{B\tau_{\mathrm{c}}}\left(\frac{W_0}{k_{\mathrm{B}}T}\right)^{\frac{2}{3}}\right).$$

<div align="right">

Equation 3-7

</div>

As stiffness is increased, the velocity at which flow becomes non-serrated is decreased, meaning that smaller driving rates are required for reaching non-serrated flow.
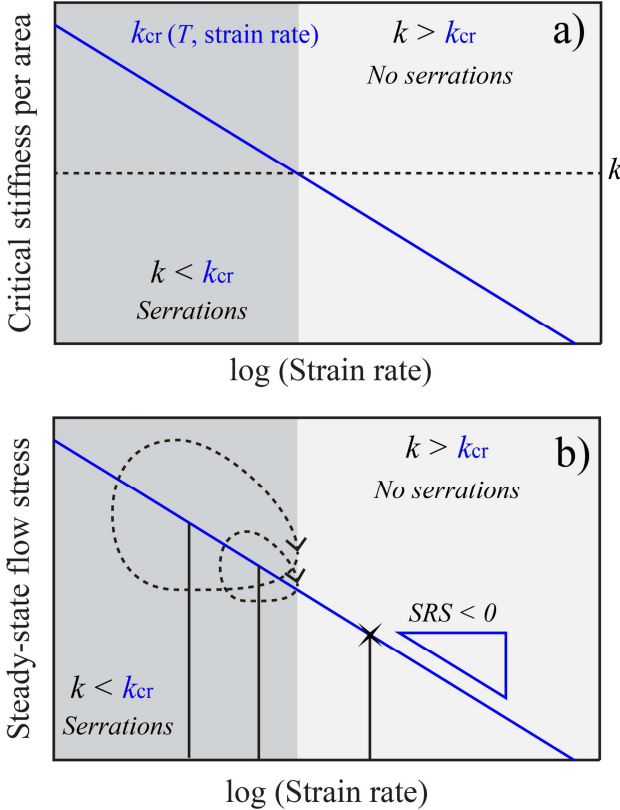

Figure 3-11: a) Critical stiffness per area k_{cr} for the transition from serrated to non-serrated flow as a function of the applied strain rate; b) steady-state flow stress as a function of the applied strain rate. The vertical lines indicate three examples of strain rates. At k < k_{cr}, serrated flow is observed, illustrated by the stress-rate trajectories.

In a narrow temperature regime, Equation 3-7 can be approximated by an Arrhenian with the temperature-dependent activation energy $E(T) = \frac{1}{B\tau_c} k W_{STZ}^{2/3} (k_B T)^{1/3}$.

In summary, model I can qualitatively explain the temperature and strain-rate dependent flow transition, as well as the experimental observation that flow in small samples (i.e. samples with an increased stiffness per area) becomes non-serrated at slower rates than in larger samples. On the downside, however, the model disagrees with experimental evidence for positive strain-rate sensitivity within the non-serrated flow regime for Zr-based glasses [117], because it assumes rate-weakening behaviour for all temperatures.

3.8.3. Model II: Effective-temperature relaxation

Interrupting a strain-rate driven compression test for a certain waiting time t_w, by setting the applied strain rate to zero, causes a stress-overshoot to appear upon the re-starting of the drive prior to the re-establishment of the steady-state flow stress (slide-hold-slide test, see also section 3.6). The magnitude of this stress overshoot depends on waiting time and temperature as [138]

$$\Delta\sigma_a = b \ln \left(1 + \frac{t_w}{\tau_0 \exp(E_a/k_B T)} \right),$$

Equation 3-8

where b and τ_0 are constants, and E_a is the activation energy for ageing. The stress overshoot is believed to reflect structural relaxation, which must therefore be captured by the effective-temperature dynamics. The original set of equations (in particular Equation 3-4) does not include a direct contribution to effective-temperature relaxation by thermal temperature, and would thus not explain ageing dynamics from slide-hold-slide experiments.
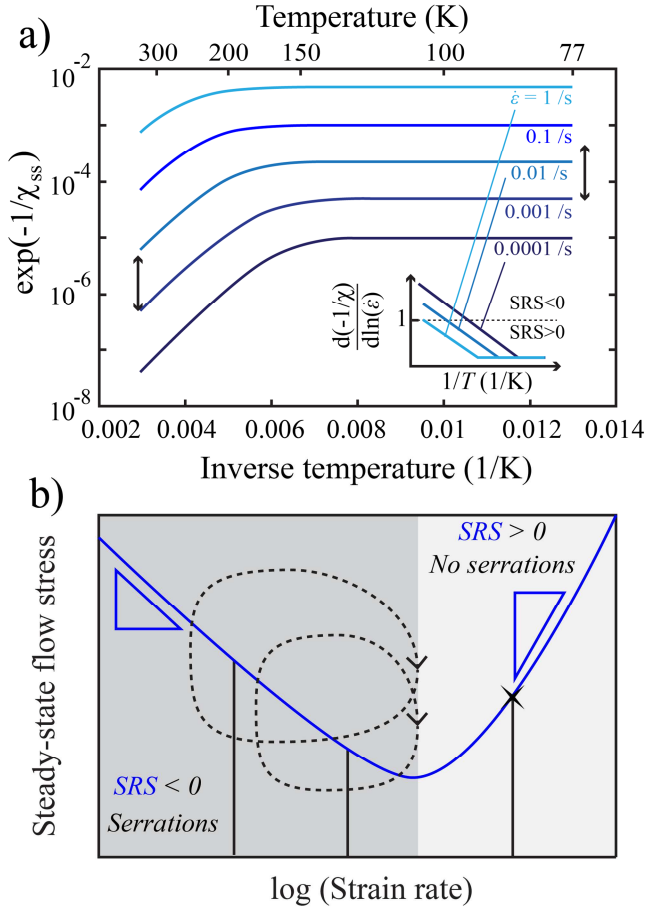
Figure 3-12: How flow-transition is predicted by model II. a) Plot of STZ density vs. inverse temperature for different strain rates. The inset shows the ratio of STZ density and strain rate as a function of inverse temperature. b) Schematic of rate-dependent strain-rate sensitivity. Three rates are indicated by drop lines. Below the transition, serrations appear, as illustrated by the trajectories.

For this reason, Equation 3-4 was modified by Daub *et al.* [138] using an additional, thermally activated relaxation term (model II):

$$\frac{d\chi}{dt} = \frac{\dot{\gamma}\sigma}{c_0\sigma_{\text{STZ}}}\left(1 - \frac{\chi}{\hat{\chi}(\dot{\gamma})}\right) - R_\chi\exp\left(-\frac{E_a}{k_{\text{B}}T} - \frac{\beta}{\chi}\right).$$

Equation 3-9

Here, R_χ is the effective-temperature relaxation rate, E_a is the activation energy for relaxation events, and β is the normalized energy for formation of zones that can relax. The authors numerically solved Equation 3-9 for the steady state, i.e. $\frac{d\chi}{dt} = 0$, to obtain the rate and temperature dependent steady-state effective temperature χ_{ss}.

The relaxation term at low temperatures, it turns out, is zero, and the rate-sensitivity is determined by $\hat{\chi} = \chi_{\text{w}}/\ln(q_0/\dot{\gamma}t_0)$, where χ_{w}, in this model, is set to be larger than unity, which is the usual case for intrinsically rate-strengthening material. This causes low-temperature flow to be non-serrated and complies with experimental results on positive SRS within the non-serrated flow regime [117]. At increased temperatures, the relaxation term comes into play. Its effect on the steady-state effective temperature eventually turns the rate-sensitivity negative, thereby causing a transition to serrated flow. While this is complicated to track down analytically, it can be well explained graphically by Figure 3-12a. For different strain rates, the exponential function of the inverse of the negative of the steady-state effective temperature (which is proportional to STZ density) is given as a function of the inverse thermal temperature. At very low temperatures, STZ density is independent of thermal temperature, and fully determined by the applied strain rate. Only as temperature increases, relaxation in Equation 3-9 becomes relevant and reduces STZ density. The temperature at which this transition happens is strain-rate dependent. Moreover, the smaller the activation energy for ageing, the lower the temperature where this transition occurs. At low temperatures

an increase in strain-rate of one decade causes a change in STZ density of less than one decade (black arrow to the right). Additional stress is required to maintain the applied strain rate, i.e. the system is rate-strengthening. At higher temperatures, the identical increase in strain rate produces an increase in STZ density of more than a decade (black arrow to the left). In consequence, less stress is needed to drive the system, i.e., it has become rate-weakening. This is further illustrated in the inset, showing how STZ density changes with strain rate as a function of inverse temperature. The SRS is positive below, and negative above unity. Note that this transition from strengthening to weakening is observed with χ_w fixed at a positive value. Figure 3-12b shows the transition in a graph of steady-state flow stress versus the logarithm of the applied strain rate. Flow behaviour at three different strain rates is illustrated. For rates at which the curve has a negative slope (negative SRS), flow is serrated, as indicated by the serration trajectories. For rates at which SRS is positive, stable flow is observed. While it is straightforward to determine the transition graphically from Figure 3-12, analytically only an approximate solution can be given, that directly relates the activation energy of the transition (or, equivalently of shear-band velocity) E_S to the activation energy of ageing E_A [138].

$$\frac{d\ln\dot{\gamma}_t}{d(1/T)} = \frac{E_S}{k_B} = -\frac{E_a}{k_B\left(1 + \frac{\beta}{b_\chi}\right)}.$$

Equation 3-10

The constant β is a typical energy scale for the formation of relaxation events and b_χ is a constant which is linked to the energy scale for the kinetically ideal effective temperature $\hat{\chi}$.

Model II was successfully used to reproduce experimental data

on ageing, the flow transition, and temperature-dependent steady-state stress. Effects of stiffness, however, were not considered. More to the point, the inertia M in Equation 3-5 was set to zero, motivated by the small sample mass. It is noted that this might, however, be an oversimplification, because this approach also ignores the inertia of involved machine leverage, which is typically of the order of considerable 10-100 kg. this point will be addressed in further research.

3.8.4. Summary of STZ modelling

Two models have been presented which investigate inhomogeneous flow by means of STZ theory. Model I interprets the flow transition as a stabilization of stick-slip instability via stiffness, while model II suggests that it is caused by an intrinsic change of rate-sensitivity due to temperature-dependent internal, structural-relaxation dynamics. Table 3-2 compares the two models and their predictions concerning flow phenomenology.

Both models successfully reproduce the flow transition and rate-weakening behaviour in the serrated flow regime. Both also correlate the activation energy for the transition to a material-specific energy scale. Model I, however, explains neither ageing dynamics

Table 3-2: Overview of the two models I (stiffness) and II (relaxation) and how they comply with experimental results of MG flow.

Phenomenon	Model I (stiffness)	Model II (relaxation)
Flow-transition	✓	✓
Size-effect on flow transition	✓	?
Ageing dynamics	✗	✓
Negative SRS during SF	✓	✓
Positive SRS during NSF	✗	✓
Transition activation energy depends on...	$kW_{STZ}^{2/3}$	E_a

nor the positive rate-sensitivity observed experimentally in the non-serrated flow regime. Model II, on the other hand, does not so far explicitly include the effects of critical stiffness and inertia.

3.9.   Summary

Well below T_g, MGs deform inhomogeneously, with plastic strain highly localized within thin shear bands: a process which creates shear steps on the specimen surface. Depending on strain rate and temperature, flow curves can be smooth or discontinuous (serrated). From the smooth flow curves we can determine relaxation energies via slide-hold-slide tests, whereas we obtain serration duration Δt, load drop ΔF and shear offset Δu_{pl} from serrated flow curves. Among the suggested mechanisms of strain-accumulation within the shear band, the model of a simultaneously shearing weakened material layer is most suitable to explain the experimental results. The shear-band velocities calculated in agreement with this model (scenario 4) in Figure 3-6) are thermally activated, as is the transition from serrated to non-serrated flow. In fact, the shear-band velocity determines how fast the externally applied strain rate must be to suppress serrated flow. In the framework of STZ modelling, the flow transition is associated with a stabilization of the stick-slip shear instability via either stiffness or a switching of strain-rate sensitivity from negative to positive, due to the temperature dependence of the underlying structural relaxation processes.

4. Aims of the thesis

"The aim of argument, or of discussion, should not be victory, but progress."

Joseph Joubert

The first part of this thesis aims i) to characterize the influence of alloy composition on shear-band dynamics in various glass-forming alloys; ii) to identify the physical origin of this composition dependence; and by that iii) to formulate novel design strategies to create MG alloys with improved mechanical stability. The second part of this thesis aims to resolve the long-standing question of temperature within active shear bands. The experiments carried out in this project aim also to facilitate a deepened understanding of the interplay between sample and testing setup.

5. Materials and methods

„Baby, I've been
Breaking glass in your room again.“

David Bowie

This chapter documents alloy production, characterization, sample preparation, details of mechanical testing and infrared-thermometry, and discusses the evaluation of the data gathered.

5.1. Production of metallic glasses

Table 5-1 gives an overview of the set of alloys that were success-fully produced in-house. The acronyms in the column titled "Route" refer to the applied processing method. These routes, i.e. IHIC for inductively heated and injection cast, MASC for mini-arc suction cast and FL for fluxed and water quenched, are described later in more detail. Unlike the majority of the alloys listed in Table 5-1, the composition $Zr_{65}Co_{25}Al_{10}$ was not taken from literature, but emerged from a side-experiment aiming at a full substitution of Cu by Co in the alloy $Zr_{65}Cu_{25}Al_{10}$. Credit for this idea goes to Dr. K. Laws.

Table 5-1: List of MG alloys produced in-house; their route of production (IHIC: inductively heated and injection cast, MASC mini-arc suction-cast, FL: fluxed and water quenched) and the reference to the original research article reporting on glass formation.

Alloy	Route	Ref.
$Au_{49}Cu_{26.9}Ag_{5.5}Pd_{2.3}Si_{16}$	IHIC	[148]
$Cu_{60}Zr_{20}Hf_{10}Ti_{10}$	MASC	[149]
$La_{67.5}Al_{15}Cu_{7.5}$	MASC	[150]
$La_{57.5}Al_{15}Cu_{27.5}$	MASC	[151]
$Ni_{61.5}Nb_{38.5}$	MASC	[152]
$Pt_{57.5}Cu_{14.7}Ni_{5.3}P_{22.5}$	FL	[153]
$Zr_{65}Co_{25}Al_{10}$	MASC	
$Zr_{90-x}Cu_xAl_{10}$ (x=25, 30, 35, 40, 45)	MASC	[24]
$Zr_{57.1}Co_{28.6}Al_{14.3}$	MASC	[154]
$Zr_{52.5}Cu_{17.9}Ni_{14.6}Al_{10}Ti_5$ (Vit105)	MASC	

The raw materials, their purity, shape and supplier, and a note on the element-specific cleaning procedure are compiled in Table 5-2. Using these starting materials, batches of the nominal compositions were weighed to sub-mg accuracy, corresponding to accuracies of < 0.02 at.% in elemental content.

Table 5-2: Raw materials with purity, shape (B: bar; R: rod; Pc: pieces; Pl: plate; Sl: slug; St: shots; C: coin; Pts: Pellets; CB: crystal bar), supplier and cleansing agent(s). Proportions of chemicals refer to volumes of standard-grade reagents.

El.	P (%)	S	Supplier	Cleansing agent
Ag	99.9	B	Credit Suisse	-
Al	99.999	R	Kryal	-
Au	99.99	B	UBS	-
Co	99.9	Pc	Alfa Aesar	HCl + Fe$_3$Cl (sat.)
Cu	99.998	R	Praxair MRC	HNO$_3$ (+Cu$_2$SO$_4$).
Hf	99.9	Pl	Haines & Maassen	HF:HNO$_3$:H$_2$O 1:1:10
La	99.88	Pc	Treibacher	Steel file
Nb	99.95	Sl	Alfa Aesar	-
Ni	99.95	St	Alfa Aesar	HNO$_3$
P	99.999	Pc	Cerac/Materion	-
Pd	99.95	C	Credit Suisse	-
Pt	99.95	B	UBS	-
Si	99.999	Pc	Cerac/Materion	-
Ti	99.995	Pts	Cerac/Materion	-
Zr	99.8	CB	MM&A	HF:HNO$_3$:H2O 1:1:10

5.1.1. Mini-arc suction casting (MASC)

This route applies to the alloys denoted as MASC in Table 5-1. The nominal compositions of the alloys (batch weights of approximately 20 g) were produced by melting the elements together in an Edmund Bühler Arc-Melter under a high-purity argon atmosphere (6N). More than ten cycles of melting and flipping of the pre-alloy lumps were performed in order to achieve maximum chemical homogeneity. With a hydraulic crusher, the pre-alloy lumps were portioned into pieces of 1.5-2 g. Shaping into rods was
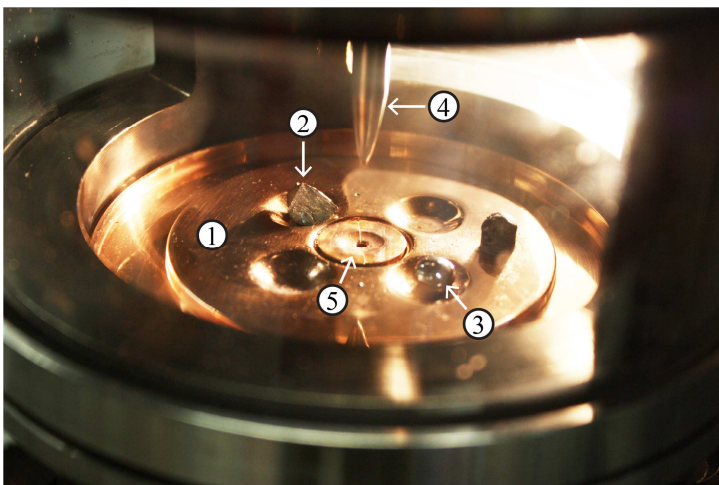
Figure 5-1: Mini-Arc chamber with water-cooled copper hearth (1), pre-alloy lump (2), titanium getter (3), anode (4), and exchangeable copper mould (5).

accomplished using an Edmund Bühler MAM 1 mini-arc melter with a built-in suction-casting setup (Figure 5-1). On a water-cooled copper hearth (1), a piece of pre-alloy (2, $Cu_{60}Zr_{20}Hf_{10}Ti_{10}$ in this case) and a piece of elemental titanium for oxygen gettering (3) were positioned. A high-purity argon atmosphere was created by first evacuating the chamber to high vacuum (5×10^{-5} mbar) with a turbo pump, and by carrying out three cycles of flushing the chamber with 6N argon and subsequent evacuation to pressures below 0.1 mbar. After the third cycle, the chamber was filled with 6N argon to an overpressure of 0.05 bar. An electric arc was ignited between the metal piece and the movable top anode made of tungsten (4), causing melting of the sample. The custom-designed, exchangeable copper mould (5) was connected to an under-pressure reservoir (Δp: -0.3 to -0.7 bar) by a valve. Upon opening this valve, the melt was sucked into the copper mould by the pressure difference and was cooled down very quickly. The moulds were rod

shapes of 2 mm, with the exception of $Zr_{65}Co_{25}Al_{10}$, for which 1.7 mm samples were cast due to the minimal glass-forming ability of the alloy.

5.1.2.   Inductive heating and injection casting (IHIC)

While pre-alloying of the Au-based alloy in the mini-arc setup was unproblematic, wetting phenomena impeded successful rod-casting by MASC. For this reason an alternative processing route using inductive heating was chosen. This shaping process is shown in Figure 5-2. a) A pre-alloy portion of 2.5-3 g (1) was fed into an aluminium-oxide crucible (2). Wrapped into molybdenum foil (3) to improve the coupling to the induction field, the crucible was
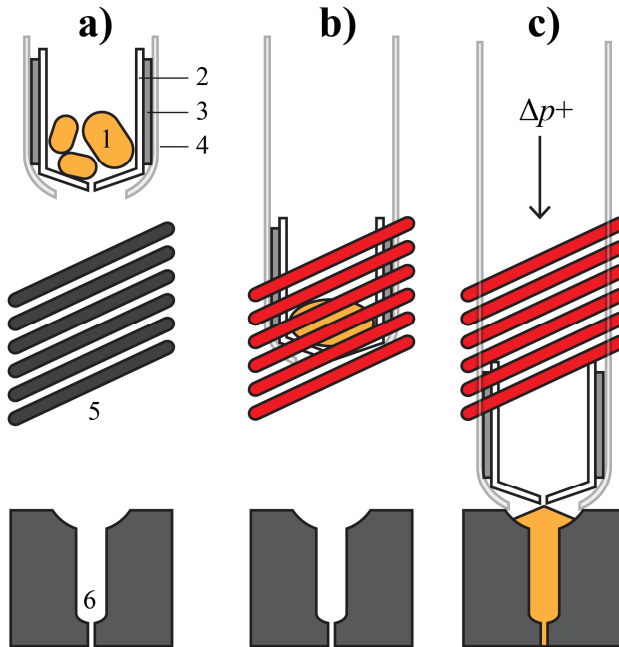

Figure 5-2: Inductive heating and injection casting (IHIC): 1) pre-alloy lumps; 2) Al_2O_3 crucible; 3) Mo-foil; 4) quartz-glass tube; 5) Cu coil; 6) Cu-mould. See main text for detailed description of the processing steps.

positioned at the end of an open quartz-glass tube (4), which was mounted in a vacuum chamber. The top end of the glass tube was connected to an over-pressure reservoir (+ 0.3 bar) by a valve. Within the chamber, a 6N argon atmosphere was created. To prepare the melting process (b), the crucible was positioned directly within the copper coil (5) by external handles, which allowed the adjusting of the vertical position of the glass tube. The inductive field was switched on and the crucible temperature was controlled by the generator power, which was increased incrementally by minutes until complete melting of the pre-alloy was observed. After a holding time of ca. 20 s, the tube was lowered to contact position with the copper mould (6), the valve between quartz tube and pressure reservoir was then opened and the melt was pushed into the mould (c).

5.1.3. Fluxing and water quenching (FL)

This method was applied to the alloy $Pt_{57.5}Cu_{14.7}Ni_{5.3}P_{22.5}$. When alloying major amounts of elemental phosphorus, temperature should be thoroughly controlled and not be unnecessarily high. This is firstly because of the high vapour pressure of phosphorus at temperatures above 350 K, which may threaten the integrity of the casting setup, and secondly due to the tendency of the element to resublime in its toxic, white allotrope form, which may cause contamination of the entire casting setup. For these reasons the use of the MASC is impeded, and an alternative two-step alloying route was chosen. First, pre-alloys of the metallic elements Pt, Cu and Ni were produced in the arc melter. Pre-alloy portions of 5 g were then sealed in bent quartz tubes together with the corresponding nominal composition of red phosphorus, in such a way that the pre-alloy was located at the one end of the tube, and the phosphorus at the other (Figure 5-3).
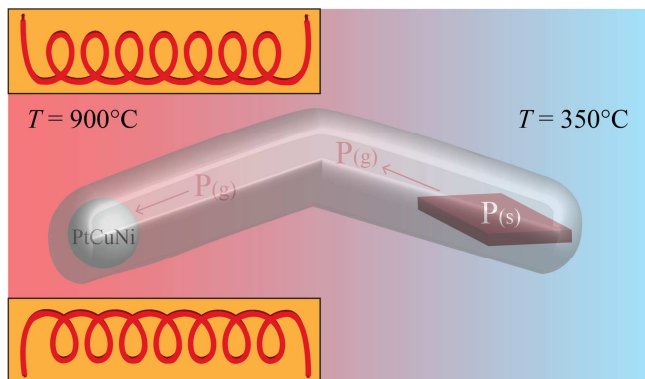
Figure 5-3: Alloying of Pt$_{57.5}$Cu$_{14.7}$Ni$_{5.3}$P$_{22.5}$. A pre-alloy portion of the metallic elements Pt, Cu and Ni and pieces of elemental red phosphorus are positioned at the two ends of a sealed quartz-glass tube. By partially inserting the tube into a furnace, a temperature gradient is installed.

This tube, with thermo-elements attached to both ends, was then partly inserted into an Isotech Pegasus 1200B furnace. By inserting the tube only partially, a temperature gradient was installed, such that the temperature at the metal lump increased to above 900°C while the temperature at the phosphorus end reached only about 350°C, i.e. a temperature at which phosphorus sublimes with a moderate vapour pressure. At the metal end, gaseous phosphorus was integrated into the alloy. After around 3 h, all of the elemental phosphorus had been transferred into the pre-alloy and the tube was quenched in water. After that the pre-alloy was shattered into small pieces and fed into a quartz tube of 2.5 mm diameter and a wall thickness of 0.5 mm. Under a boron-oxide cover flux, the alloy was repeatedly thermally cycled from 400 to 950°C. Cooling to the amorphous state was performed by water quenching.

5.2. Characterization

After casting, samples were ascertained as X-ray amorphous via diffraction experiments using a STOE STADI P Powder diffractometer (IP-PSD detector, Cu K$_\alpha$ radiation, 45 kV, exposure time 1 to 3 h) and checked for a glass transition via Differential Scanning Calorimetry (DSC) using a Netzsch DSC 404 C Pegasus (heating rates 10- 20 K/min).

Table 5-3: Glass transition temperatures of the alloys produced and their comparison to literature values. The heating rate is 20 K/min unless indicated otherwise.

Alloy	T_g (K)	T_g ref. (K)	Ref.
$Au_{49}Cu_{26.9}Ag_{5.5}Pd_{2.3}Si_{16}$	401	401	[148]
$Cu_{60}Zr_{20}Hf_{10}Ti_{10}$	722	725	[149]
$La_{67.5}Al_{15}Cu_{7.5}$	391	389	[150]
$La_{57.5}Al_{15}Cu_{27.5}$	402	404-408	[151]
$Ni_{61.5}Nb_{38.5}$	892	892	[152]
$Pt_{57.5}Cu_{14.7}Ni_{5.3}P_{22.5}$	502	508	[155]
$Zr_{65}Co_{25}Al_{10}$	688		
$Zr_{65}Cu_{25}Al_{10}$	635†	650-659*	↑
$Zr_{60}Cu_{30}Al_{10}$	654†	670-679*	
$Zr_{55}Cu_{35}Al_{10}$	674†	690-709*	[156]
$Zr_{50}Cu_{40}Al_{10}$	695†	710*	↓
$Zr_{45}Cu_{45}Al_{10}$	710†	720-729*	
$Zr_{57.1}Co_{28.6}Al_{14.3}$	734	742*	[154]
$Zr_{52.5}Cu_{17.9}Ni_{14.6}Al_{10}Ti_5$	680		

† measured at 10 K/min
* measured at 40 K/min

The XRD patterns and DSC traces are shown in Figure 5-4 and Figure 5-5, respectively. All alloys were found to be XRD-amorphous and to show a glass transition. The respective T_g values and a comparison to literature values are given in Table 5-3. While generally in good agreement, a systematic deviation is observed for

cases where the literature heating rate (40 K/min) was significantly greater than the heating rates applied in this study (10 K/min for the $Zr_{90-x}Cu_xAl_{10}$ alloy series, 20 K/min for $Zr_{57.1}Co_{28.6}Al_{14}$).
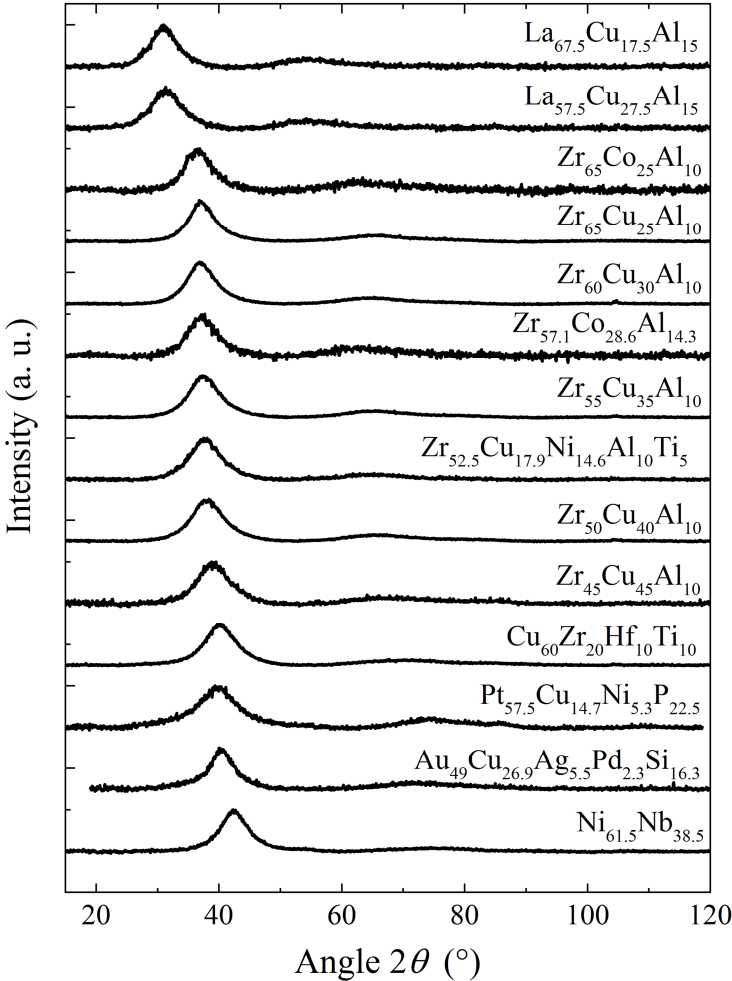

Figure 5-4: XRD patterns of the alloys produced in-house. The alloys are arranged according to the position of the amorphous shoulder.
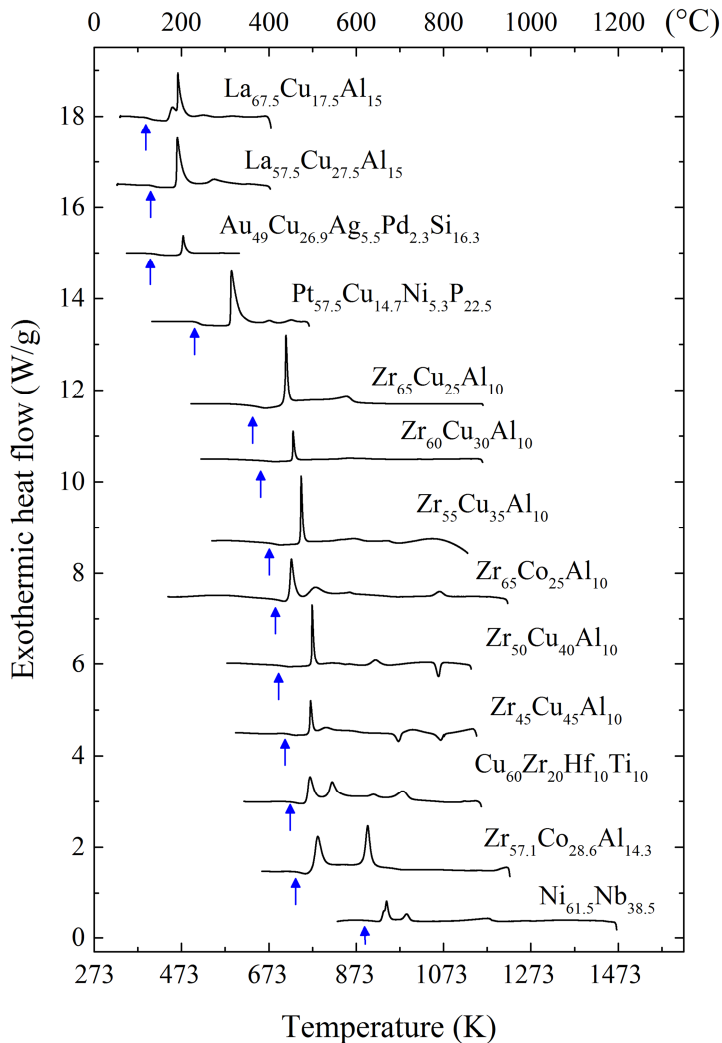
Figure 5-5: DSC traces up to the melting temperature T_m for the alloys produced. The glass transition temperature T_g is indicated by blue arrows. Alloys are sorted by their glass-transition temperature in ascending order.

In addition to the alloys produced in-house, wedges of $La_{61.54}Cu_{23.08}Al_{15.38}$ were provided by K. Laws from the University of New South Wales, Australia.

5.3. Specimen preparation

From the rods (an example is shown within an opened, exchangeable mini-arc mould (Figure 5-6a)), specimens with an aspect ratio of 1.6-2 were cut using a water-cooled Accutom precision saw. The top and bottom surfaces were made orthogonal by grinding and polishing. To avoid geometric constraints (compare with section 3.7), the samples were equipped with a small notch, oriented at 45° to the vertical axis, via Electric Discharge Machining (EDM) using a 100 µm wire (Cu-W alloy) on an Agema Puls machine. Note that the small notches, introduced here to force the shear band to initiate at the free lateral surface rather than at the contact points between sample and anvil, are
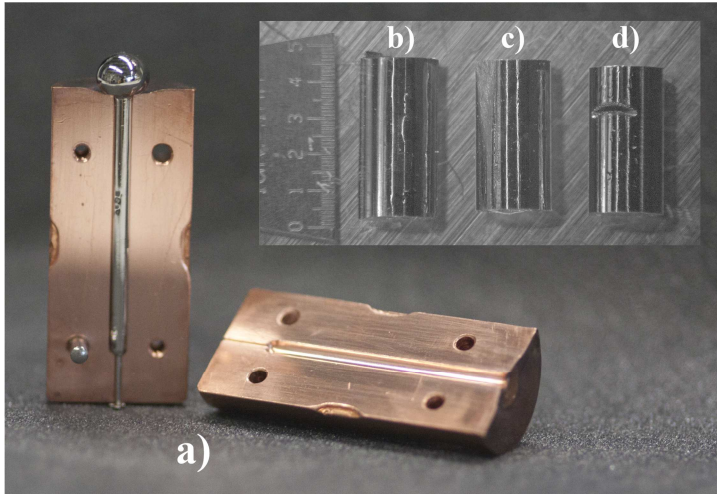

Figure 5-6: (a) Suction-cast rod of 2 mm diameter in an exchangeable mini-arc mould. Inset: specimen after cutting (b), grinding (c), and notching (d).

63

considerably smaller in length (factor >10) than the large notches used in studies on plasticity under complex stress states [157]. The inset to Figure 5-6 shows the different stages of sample production, i.e. b) after cutting, c) after orthogonalization of the top and bottom surfaces, and d) after notching. The dimensions of a notch were derived from its apparent length in light-microscopy images (Figure 5-7). In the projection of the sample observed through the optical microscope, the lengths x and y were measured. The opening angle 2α is described by trigonometry as $2\alpha = \arcsin(1 - x/r) + \arcsin(1 - y/r)$. The baseline of the notch is calculated as $2a = 2r\sin(\alpha)$. The area of the notch thus becomes $A_{\text{Notch}} = \alpha r^2 - a(\sqrt{r^2 - a^2})$. Typical notch areas cause a relative cross-section reduction of 3-8%.
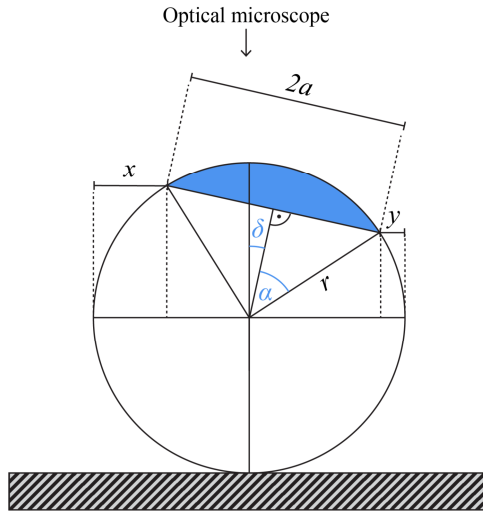

Figure 5-7: Calculating the notch area from lengths x and y assessed by light microscopy. δ is the angle of misalignment and α is half the notch opening angle. The schematic is adapted from Ref. [158].

5.4. Mechanical testing

Mechanical tests were performed on a screw-driven Schenck Trebel RMC 100 mechanical testing machine, with a stiffness of 1/10 nm/N. The major parts of the setup are shown in Figure 5-8. Deformation is applied to the bottom cross-bar (2) by a screw,
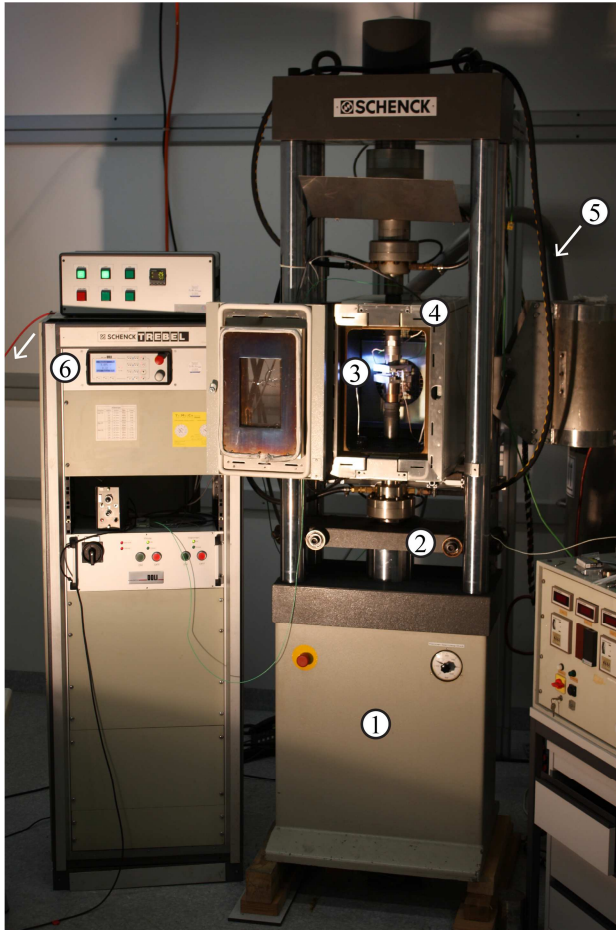

Figure 5-8: Mechanical testing setup. (1) Screw compartment; (2) moving cross-head; (3) sample stage; (4) environmental chamber; (5) connection to liquid nitrogen supply; (6) analogue-to-digital converter.

which is located in the bottom compartment (1). The position of the sample, i.e. between the anvils, is indicated by (3). A close-up of this part is provided in Figure 5-9. An EC2043 environmental chamber from Severn Thermal Solution (4) allows conducting tests to be carried out at temperatures from 93 K (-180°C) to 873 K (600°C). The cooling medium is liquid nitrogen. The connection between the chamber and the pressurized storage-vessel is marked with (5). The means to reach high temperatures is resistive heating. The raw data is converted from analogous to digital by a DOLI EDC580 interface (6). The accompanying software, Doli Test and Motion (V.4.3.04) enables the free programming of test procedures.

The sample stage is shown in greater detail in Figure 5-9. The sample (1) is positioned between two small hard-metal plates (2) which distribute the stress to the anvils. An aluminium
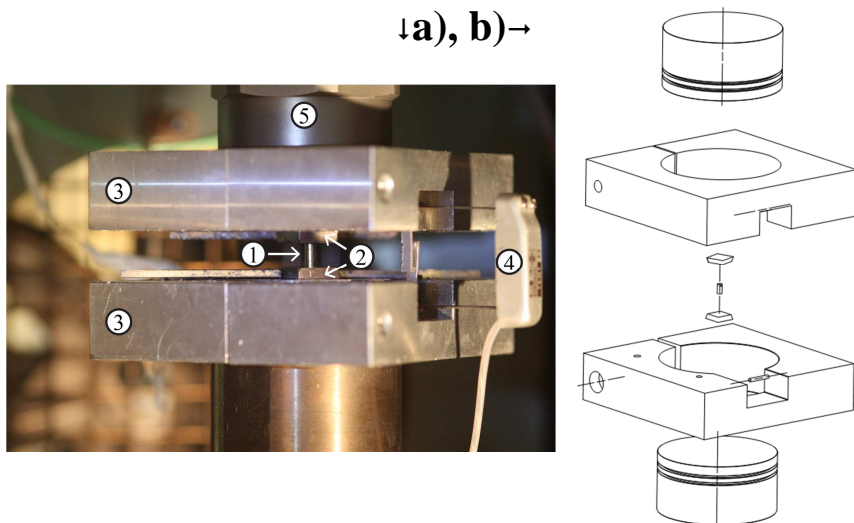
↓a), b)→

Figure 5-9: a) Close-up of the sample stage: (1) Compression sample; (2) hard-metal plates; (3) extensometer-attachment setup; (4) extensometer, and (5) piezo-load cell. b) CAD exploded view of the sample stage.

construction (3) attached to the crossheads makes possible the reproducible and stable attachment of an EXA20-50 Extensometer from Sandner Messtechnik (4). Above the top anvil, a piezo-electric load cell KIAG Swiss 9361 A (5) is inserted into the load line, allowing dynamic assessment of fast load changes. It is also noted that only dynamic piezo cells are capable of correctly recording fast serrations, while hydraulic or strain-gauge load cells cannot properly resolve dynamic load changes which occur over short periods. It is noted that the extensometer indeed bridges the anvils, i.e. measures the length change of sample and hard-metal plates. Due to their great stiffness (ca. 1 nm/N) the contribution of the latter is, however, negligible.

5.5. Shear-band properties from serrations

Figure 5-10a shows a typical sequence of serrations from measurements. A custom designed MatLab routine (V. R2010a) was deployed to evaluate the size and time of individual load drops (Figure 5-10b) and their conjugated displacement bursts (Figure 5-10c) via simple three-fold linear fitting, providing us with the three major serration parameters load drop ΔF, serration duration Δt and apparent length change Δu_0. From these quantities, the shear-band velocity, viscosity and temperature can be calculated. The upper resolution limit for shear-band velocities is on the order of 20 mm/s.
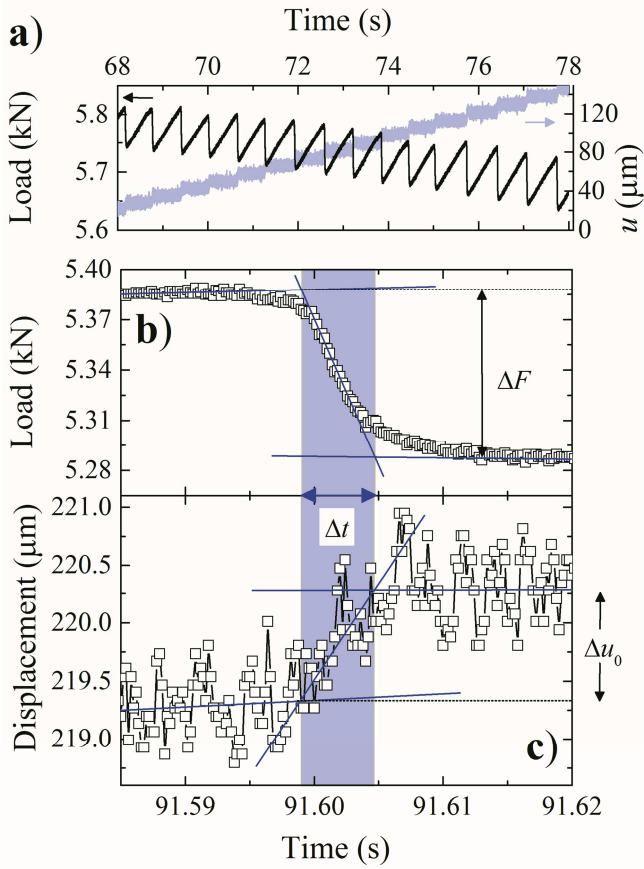
Figure 5-10: Assessment of serration properties. a) Serrations in load and displacement signal; b) close-up of a load drop including three-fold linear fitting to assess Δt and ΔF; c) close-up of the corresponding displacement jump, illustrating the determination of Δu_0.

5.6. Infrared thermometry

Room-temperature compression tests on $Zr_{57.1}Co_{28.6}Al_{14.3}$ were monitored using a high-speed infrared camera (IRCAM Equus 81k S/M) equipped with an InSb detector, which is sensitive to the wavelength interval from 2 to 5 µm. A fixed frame size of 64×32 pixels was chosen allowing a maximum frame-rate of 3750 fps. To ensure precise temperature measurement, the specimens were covered by a thin, high-emissivity carbon coating. The temperature measured by the camera was also calibrated using type K thermocouples before testing. Synchronisation of load and IR signal was established by triggered data acquisition using a custom-designed LabView routine.

5.7. Further experimental methods

A Hitachi SU-70 scanning electron microscope (SEM) was used to investigate shear-band patterns.

Finite Element Modelling (FEM) of elastically loaded MG specimens with pre-existing shear-steps was conducted using the software ANSYS Workbench 15.0.

6. Experimental results and discussion

"The world is full of obvious things,
which nobody by any chance ever observes."

Sherlock Holmes

6.1. Effects of geometry, size and stiffness

Properly measuring compositional effects on shear-band dynamics also means properly accounting for effects originating from the experimental setup and the sample geometry deployed. The first part of the results section explores possible "side-effects" on serrated-flow behaviour stemming from notching, varying system stiffness, sample size, and strain dependence of shear-band properties.

6.1.1. Shear banding in notched compression specimens

First an investigation was conducted into how shear banding is affected by sample notching, which, as outlined in section 5.3, is necessary to control the shear-band position. To do so, interrupted compression tests (strain rate = 10^{-3} s^{-1}) were performed on as-cast and notched $Zr_{65}Cu_{25}Al_{10}$ MG samples (Figure 6-1). At three to four different increments of plastic strain, the tests were paused. During these pauses, the samples were unloaded and the shear-band pattern was investigated in the SEM. Figure 6-1 shows flow curves of notched (a) and as–cast (b) specimens. While the peak engineering stress is unaffected by the notch, the strain at which it is observed – indicated by the black arrows – differs considerably. In the presence of a notch, the peak engineering stress is reached
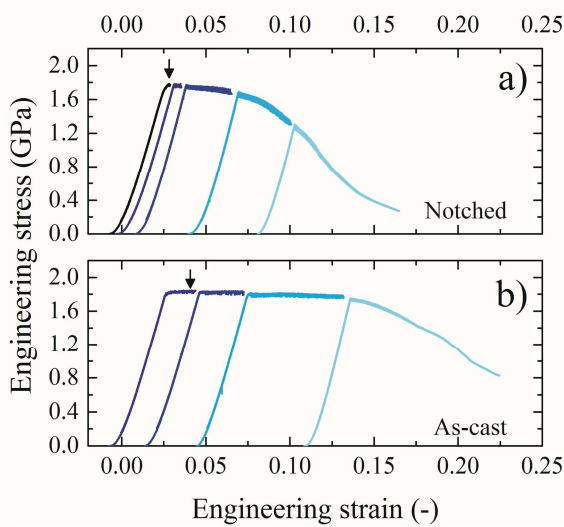
Figure 6-1: Interrupted flow curves of notched (top) and as-cast (bottom) $Zr_{65}Cu_{25}Al_{10}$ specimens.

right at the elastic-to-plastic transition, typically during the first major serrations. In the as-cast sample, on the other hand, modest apparent strain-hardening is observed beyond the yield point, shifting the peak stress to higher strains or, equivalently, later serrations. Beyond the peak stress, pronounced strain-softening is observed for the notched samples, while the flow plateaus in as-cast specimens up to a strain of 15%. Figure 6-2 shows SEM snapshots which were recorded prior to and after the interruptions of the compression tests shown in Figure 6-1. At the first interruption, we find one dominant shear band in the notched sample (f), while traces of multiple shear bands of considerable size cover the surface of the as-cast sample (Figure 6-2b). An increased shear-band density at the bottom left indicates an early contact between machine cross-head and the evolving shear step. The notched sample, on the other hand, is intersected by the dominant major

shear band at its lateral surface only (f), which allows the shear step to grow without constraint. Upon further straining, deformation is distributed over various shear planes in the as-cast sample (c-d), with a major shear band being established during the last stage only (d). The reduction in the cross-section area due to shear-offset formation is also to some extent compensated by the generation of a new load-bearing surface at the bottom left-hand corner of the sample, marked by a blue circle in Figure 6-2d. This is caused by the continuous pressing of the shear offset onto the bottom anvil. In the notched sample, deformation is primarily confined to the major shear plane throughout the whole test (f-i). With two freely developing shear offsets, the cross-section area decreases continuously.
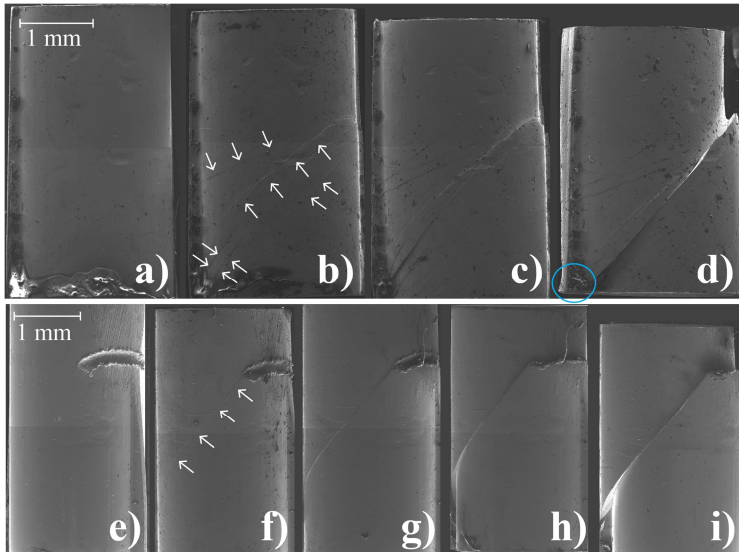

Figure 6-2: Shear-band evolution in the as-cast specimen (a-d) and in the notched specimen (e-i). Snapshots were taken prior to the test (a, e) and at the points of interruption (compare with Figure 6-1).
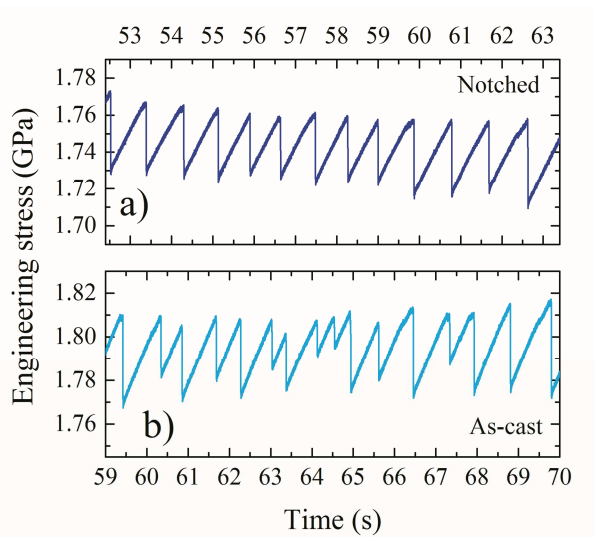
Figure 6-3: Appearance of serrated flow in notched (a) and as-cast (b) specimens.

An inspection of the flow curves at larger magnification reveals that the serrations of notched specimens have very regular shapes and sizes, whereas in the flow curves of the as-cast specimens serrations of varying sizes and alternating characteristics are observed (Figure 6-3). This behaviour is also well captured by stress-drop histograms (Figure 6-4). For notched samples the distribution density is of Gaussian type and peaks at around 46 MPa, while the distribution density of as-cast samples is bimodal, with a global maximum at 10 MPa and a local maximum at around 25 MPa. The emergence of a global maximum at lowest event sizes, as observed for constrained geometry in Figure 6-4b, typically results in a cumulative distribution function following a power law. Such behaviour is abundantly observed in systems deforming via avalanches of interacting, small, localized shear events [159].
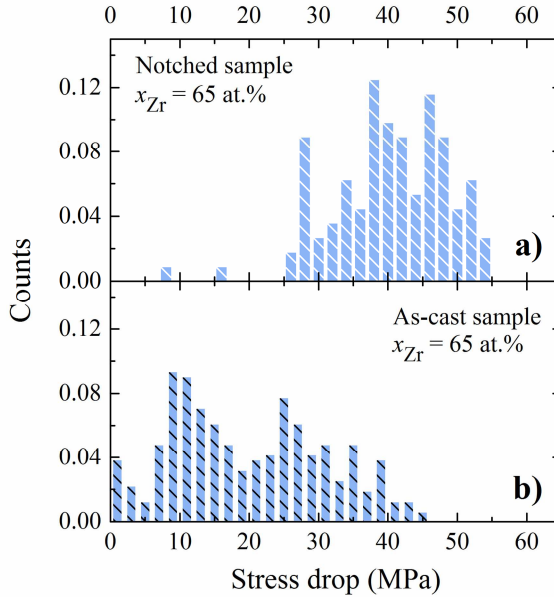
Figure 6-4: Stress-drop histograms for notched (a) and as-cast (b) $Zr_{65}Cu_{25}Al_{10}$ BMGs measured at room temperature.

A further impact of notching was found when investigating the properties of serrations as a function of plastic strain. Figure 6-5 compares the strain-dependent shear-band velocities (calculated with Equation 3-1) from an as-cast sample (open symbols) and a notched sample (solid symbols). The colour of the data points refers to the test section in which the velocities were obtained (compare with Figure 6-1). Initially, the shear-band velocities in notched and as-cast samples are similar, on the order of 0.5-2 mm/s. In both sample types, the shear-band velocity increases with increasing plastic deformation. It reaches a maximum at around 8% plastic strain and then decreases again. The increase in velocity is, however, much more pronounced in notched samples with peak speeds of 12 mm/s compared to only 6 mm/s in the as-cast samples. A further distinct
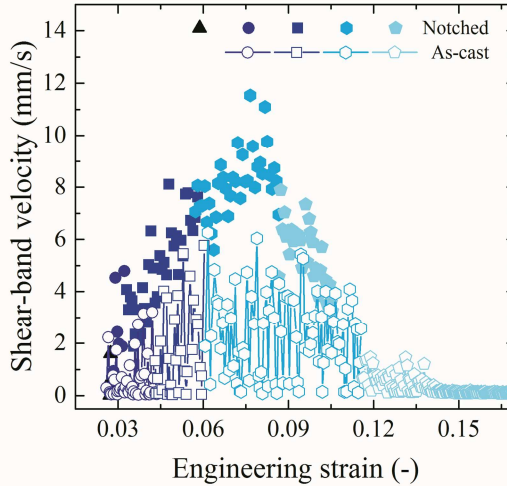
Figure 6-5: Strain-dependent shear-band velocity for as-cast and notched specimens. The different colours refer to the different loading stages in Figure 6-1.

difference between the two types of samples is the data scatter, which is more extensive in the as-cast specimens.

Discussion

Differences between notched and as-cast specimens

In notched samples, the formation of a major shear band with freely evolving shear steps at the intersections of the band with the lateral surface is promoted. Consequently, the cross-section area is incrementally reduced. This is well reflected by the strong apparent strain-softening of the corresponding flow curves. The reactivation of the major shear band is obviously preferred over the formation of new bands, and correlates with both regularly shaped and spaced serrations and a stress-drop distribution with one single global maximum. In un-notched samples shear bands are typically initiated at contact points between sample and anvil. Emerg-

ing shear offsets at these points cannot evolve freely and are arrested by geometric constraints. Therefore, re-activation of pre-existing bands is no longer preferred over the initiation of new bands. The formation of an additional load-bearing area at these regions of multiple shear-band initiation is also observed (compare also to Ref. [75]). This process counteracts the cross-section area reduction, thus contributing to the installation of a stress plateau in the flow curves. The irregular size and shape of the serrations can be attributed firstly to the alteration of initiation of new bands and reactivation of pre-existing bands, and secondly to the occurrence of non-system-spanning events in the presence of strong geometric constraints. These non-system-spanning – possibly even interacting – events are also believed to be the cause of the low-stress global maximum in the stress-drop histograms (Figure 6-4) [160].

The insight that shear-band re-activation is effectively suppressed by geometric constraints in as-cast samples may further help to understand the differently accentuated strain dependence of shear-band properties in the notched and as-cast specimens. Throughout the test, shear-band velocities in the as-cast specimens are comparable to those in the notched samples obtained at very early strains (Figure 6-5). The pronounced increase in shear-band velocity with strain in notched samples must thus be strongly linked to shear-band reactivation. The possible causes of strain-dependent shear-band dynamics are discussed in more detail in section 6.1.3.

In summary, notching was found to encourage the establishment of one major shear plane. By this, the boundary conditions of the compression tests become more reproducible, because effects of geometric constraint are suppressed. It was further found that

notching promotes i) a discrete elastic-to-plastic transition; ii) pronounced apparent strain-softening; iii) regularly shaped and spaced serrations and iv) pronounced strain-dependent shear-band velocities.

6.1.2. Stiffness and sample size

Other issues often raised when discussing the impact of the testing setup on plastic flow in metallic glasses are system stiffness and sample diameter [76, 77, 139]. Typically, the effects of both parameters are summarized in an effective stiffness term $k = [A(C_M + C_S)]^{-1}$, where A is the sample's cross-section area, and C_M and C_S are the compliances of machine and sample, respectively. Note that k has the units of GPa/mm, and therefore is a stiffness normalized by an area. In the following, the results of a small study on the effect of k on shear-band dynamics in the Zr-based metallic glass Vit105 are presented. Within this study, the stiffness k was modified firstly by varying C_M by the insertion of compliant modules into the load line of the testing machine, and secondly by testing samples of varying diameters.

In order to decouple effects of stiffness and diameter from effects of plastic strain (compare with the previous section), only the first five serrations after the peak stress were evaluated. Figure 6-6 summarizes the observed effects of k on serration properties. The different sample sizes (d = 2, 3 and 5 mm) are emphasized by accordingly sized data points. A weak, monotonous increase in the serration amplitude $\Delta\sigma_S = \Delta F/A$ with an increasing k is observed (Figure 6-6a). The effect is, however, strongly weighted by the low stress-drop amplitude (ca. 20 MPa) for the 5 mm sample. That being absent, a constant, k-independent behaviour could also be suspected. Concerning the serration duration Δt, no general scaling with k is observed (Figure 6-6b). While it is generally found that Δt
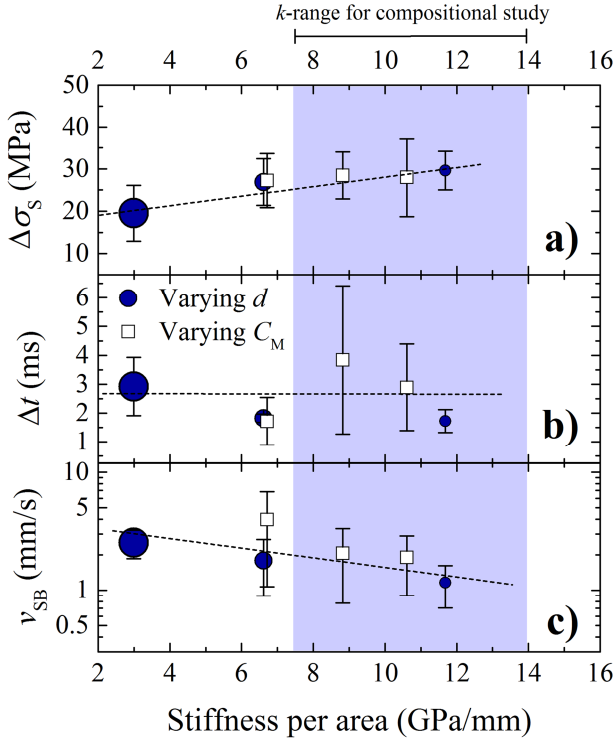
Figure 6-6: Serration size Δσ (a), duration Δt (b), and shear-band velocity v_{SB} (c) and their dependence on sample diameter d and machine stiffness C_M captured by the effective stiffness k. Lines are guides to the eye.

slightly decreases as the sample diameter is decreased, no corresponding trend for the machine-stiffness variation is revealed, because the variation in Δt appears to be of the same size as the data scattering. More general behaviour is observed for the shear-band velocity v_{SB} in Figure 6-6c. The shear bands tend to be faster in large samples and more compliant setups. The area shaded in blue marks the range of k-values that are covered in the compositional study (sections 6.2 and 6.3). We note that the variations in serration properties within that regime are on the order of the error

bars, and are thus, as we will see in the subsequent chapters, of minor importance compared to the impact of varying composition and temperature.

6.1.3. Strain-dependent serration properties

While the previous two sections investigated the influence of the experiment's starting conditions on shear-band behaviour, this section elaborates how experimental setup and sample material change during the course of an experiment, and how this might affect the measurement of shear-band properties. Particular interest is devoted to the apparent strain-dependence of shear-band velocities (Figure 6-5).

It was generally observed that shear-band velocities increase up to intermediate plastic strains and decrease thereafter. This behaviour is more pronounced in notched samples. Possible causes for this strain dependence of shear dynamics are discussed in the following, among them known triggers of changes in shear-band dynamics such as increase in temperature [130], decrease in system stiffness [76, 139], variations in chemistry [116] or density, and changes in stress state [161].

Temperature, stiffness and chemistry
Because of the repeated interruption of the compression tests, no strain-temperature correspondence can be assumed in our experiment. If temperature *was* the cause, the shear-band velocity shortly after every test interruption would be just as small as during the very first serration, which is not the case.

The system stiffness k monotonously increases with plastic strain (compare with section 3.7), thereby contributing to an overall *decrease* in shear-band velocity. However, as it increases by only 0.03% for a typical serration increment of 1 μm, the effect may be

considered too small to fully explain the slowing down of dynamics beyond intermediate strains. Furthermore, chemical segregation in shear bands is not typically observed [110].

A fragile stress state

The stress state inside the sample deviates increasingly from uniaxial as the inhomogeneous deformation proceeds. This effect is visualized by FEM modelling of the stress state within samples with pre-existing shear offsets (100, 450 and 1000 μm,) prior to shear band (re-)initiation (Figure 6-7). For this purpose, the FEM samples were strained elastically up to the point where the critical equivalent stress, 1.8 GPa, is reached over the full diameter (Figure 6-7a). The shear steps act as stress concentrators and induce a momentum onto the shear plane. Due to this momentum, the stress component acting normal to the shear plane, $\sigma_{s,n}$, well away from the stress concentrators, is found to decrease with increasing shear offset (Figure 6-7b-d). The effect is more pronounced in notched samples than in the as-cast specimens (e). Such a decrease of (confining) normal stress is assumed to facilitate faster shear banding. The degree of impact of this behaviour on shear dynamics is, however, difficult to judge, since i) the changes per serration are very small and ii) only little is known about normal-stress effects on the properties of active shear bands. Furthermore, stress-state effects are not restricted to the macroscopic scale, and the presence of local, residual stress fields can be expected. In fact, these fields are known to play an important role in the deformation process and can be quite large [162]. Based on these stresses, a hypothesis is formulated in the following by which both the strain-dependent increase *and* the subsequent decrease in shear-dynamics can be explained.
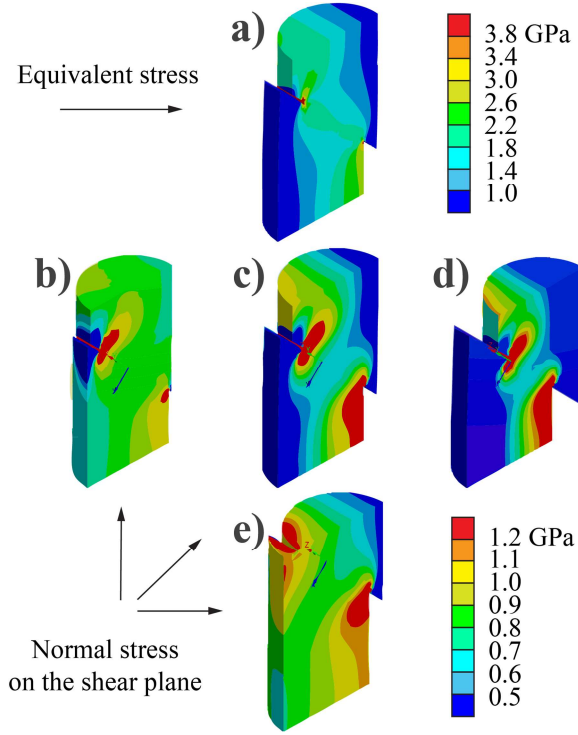
Figure 6-7: FEM visualizations of strain-dependent stress states in inhomogeneously deforming MG samples. a) Equivalent stress on the longitudinal section of a notched sample with a pre-existing 450 μm shear offset prior to shear-band initiation; b)-d) stress normal to the shear plane for notched specimens with shear offsets of 100 μm, 450 μm, 1000 μm and (e) for an as-cast specimen with a 450 μm shear offset.

Figure 6-8a shows the load trace for a sequence of two serrations, and Figure 6-8b-d shows the schematics of the corresponding MG cylinder at three different plastic strains. Red and blue circles represent zones of hypothetical compressive and tensile residual stresses, respectively. The orientation and shape of the initiating shear band S_1 (white, b) is influenced by local stresses. It will not be a smooth, flat layer, but more of a wavy, curved body, well aligned with the plane of largest shear stresses P_1 (pink line in

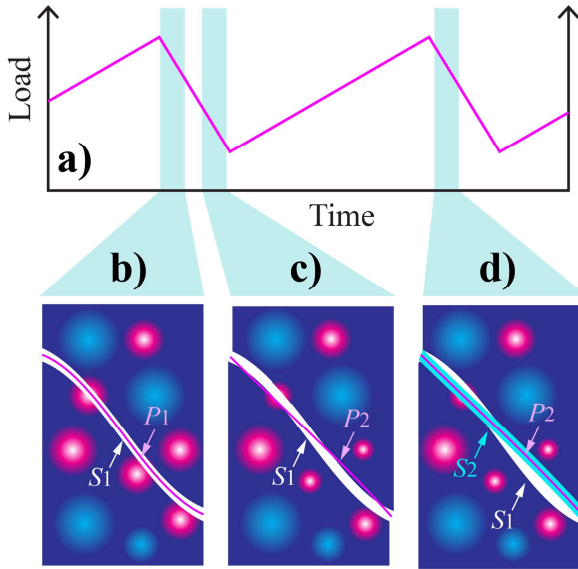**Figure 6-8: Local stresses as a possible cause of strain-dependent shear-band velocities. a) Load-time signal for a sequence of two serrations; b-d) schematics of a deforming MG cylinder at three different strains. Red and blue circles represent compressive and tensile residual stresses, respectively. S_1 and S_2 are shear bands, P_1 and P_2 denote planes of largest shear stress.**

Figure 6-8b). As the first serration cycle proceeds, the local stress state changes due to the deformation-induced partial relaxation of the residual stresses around the shear band. The plane of largest shear stress P_1 is reoriented accordingly, becoming P_2 and deviating from S_1 (Figure 6-8c). This misalignment hampers the reaching of high shear velocities and acts as an internal constraint. Upon the reaching of the second serration peak, another shear band S_2 (teal) is initiated, well aligned with the reoriented plane of maximum shear stress P_2 (Figure 6-8d). This band consists to a large extent, but not exclusively, of pre-deformed material. It is noted that due to their small thickness and proximity, the shear bands S_1 and S_2 might not be discernible in SEM images. With each serration, the

local stresses are relaxed more, and the change of P during one slip phase becomes progressively smaller. By that, the deceleration effect is minimized and, consequently, the shear-band velocity is increased.

The above-mentioned process of stress-state homogenization is counteracted by the effects of strain-induced microstructural damage, be it in the form of cracks, voids or nanocrystals. These defects on the one hand cause a re-heterogenization of the local stress states, but, on the other hand, weakening of the material may cause an overall decrease in elastic energy density within the sample. Both processes are expected to promote slower shear banding. Since damage will only become important at large plastic strains, it is a good explanation for the slow-down of dynamics at post-intermediate strains.

In summary, the bell-shaped strain-dependent shear-band dynamics is best explained by the competing processes of local stress-state homogenization, which is dominant at lower strains, and damage-induced stress-state re-heterogenization and material weakening, which is dominant at larger strains. Doubtless the solidity of this working hypothesis should be probed by future experimental studies.

6.2. Shear-band dynamics in the Zr–Cu–Al system: an intra-system study[2]

This section explores the compositional dependence of shear-band dynamics within the MG forming system $Zr_{90-x}Cu_xAl_{10}$ (x = 25, 30, 35, 40, 45). This particular system was chosen for several reasons. The first is its similarity to the Zr-based alloy Vit105 ($Zr_{52.5}Cu_{17.9}Ni_{14.6}Al_{10}Ti_5$), subject of many preceding studies on MG serrated flow [117, 129, 130, 163]. A close similarity is becoming obvious when regarding Ni as a topological substitute for Cu (Ni and Cu have similar atomic radii) and Ti as a chemical substitute for Zr (Ti and Zr belong to the same group in the periodic table), i.e. $(Zr,Ti)_{57.5}(Cu,Ni)_{32.5}Al_{10}$. Second, with the number of constituents reduced to three, fewer interactions between the species have to be considered, and the system is closer to the binary glass-forming alloys of the Cu–Zr system, the atomic structures of which have been intensively studied by computational methods [33, 164-166]. Third, the formation of bulk glassy and plastic samples has been reported over a wide range of compositions [156].

6.2.1. Experimental results on serrated flow

Figure 6-9 shows the engineering stress-strain curves for the compositions studied at 243 K.

---

[2] Corresponding publications:

(1) P. Thurnheer, R. Maaß, S. Pogatscher, J. F. Löffler, Compositional dependence of shear-band dynamics in the Zr–Cu–Al metallic glass system. *Appl. Phys. Lett.* **104**, 101910 (2014). [Figs. 6-9 - 6-12; Tab. 6-1]

(2) P. Thurnheer, R. Maaß, K. J. Laws, S. Pogatscher, J. F. Löffler, Dynamic properties of major shear bands in Zr–Cu–Al bulk metallic glasses, *Acta Mater.* **96**, 428-436 (2015). [Figs. 6-13 - 6-18, Tabs. 6-2 – 6-3]
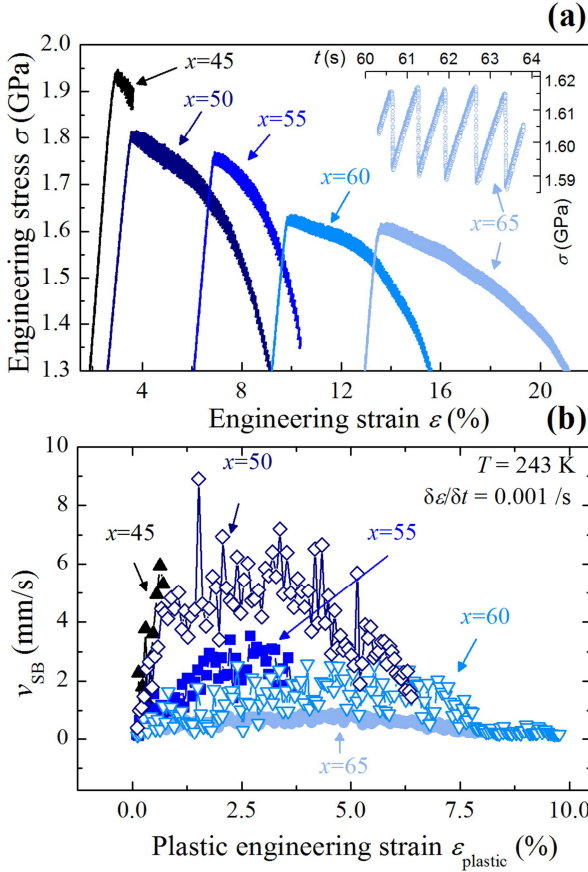
Figure 6-9: (a) Flow curves for Zr$_x$Cu$_{90-x}$Al$_{10}$ at 243 K. The inset shows a close-up of the serrated flow regime for the alloy with $x = 65$. (b) Shear-band velocities obtained from the flow curves in (a) as a function of plastic engineering strain $\varepsilon_{plastic}$.

It is notable that the data in Figure 6-9a exhibit no apparent strain hardening or constant flow-stress plateau. Indeed, all curves show pronounced strain softening, which we attribute to the geometrically unhindered propagation of a major shear band initiated at the notch. Further, the strength decreases with increasing Zr-

content, following the same trend as the glass transition temperature. This is in general agreement with the existence of a universal yield criterion in metallic glasses [7]. As an example, the inset to Figure 6-9a displays a stress-time trace for a series of serrations in $Zr_{65}Cu_{25}Al_{10}$, indicating a very regular spacing that is observed across all compositions. In Figure 6-9b the shear-band velocities, derived from the same curves as presented in Figure 6-9a, are depicted as a function of plastic engineering strain which is defined to be zero where the maximum stress is reached, coinciding well with the elastic-plastic transition. The shear-band velocity as a function of plastic strain shows semi-circular behaviour, spanning almost one order of magnitude in v_{SB} (compare also with section 6.1.3). Due to limited malleability, this velocity-strain scaling is not observed for $Zr_{45}Cu_{45}Al_{10}$ at 243 K. At this stage it is clear that both a strain and compositional dependence of v_{SB} is found. The non-monotonic trend of v_{SB} as a function of strain cannot be straightforwardly characterized with a single parameter. We have thus explored five different methodologies, which are: i) an average velocity from 0 to 0.25% plastic strain, termed v_{SB-1}; ii) an average velocity from 1-1.5% plastic strain, called v_{SB-2}; iii) an average velocity of all values centered symmetrically (+/- 0.25%) around the maximum shear-band velocity, termed v_{max}; iv) averaging all values from zero plastic strain to the maximum shear-band velocity, called v_{mean}; and finally v) the slope of a linear fit of the increasing regime up to the maximum velocity (v_{fit}). Figure 6-10 summarizes the calculated shear-band velocities (at 243 K) for all five approaches taken, and demonstrates the robustness of the analysis method: irrespective of the strain regime, the shear-band velocity decreases with increasing Zr-content. The same trend is observed for v_{fit}. In the following we focus our analysis on v_{SB-1}, motivated by the ability to also capture the dynamics of $Zr_{45}Cu_{45}Al_{10}$.
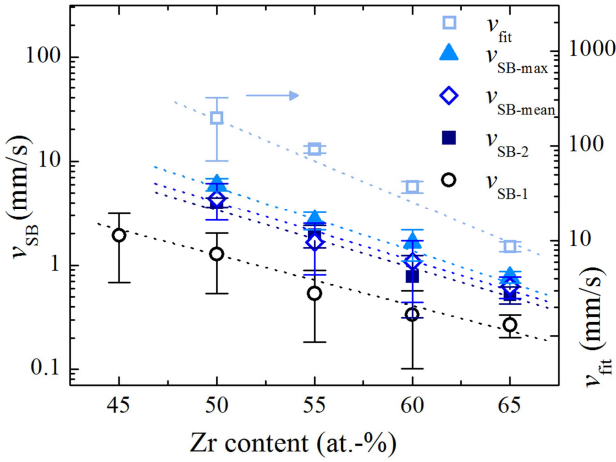
Figure 6-10: Compositionally dependent shear-band dynamics at 243 K, assessed according to five different one-parameter description methods. Lines are guides for the eye.

As a next step, the temperature dependent shear-band velocity for all alloy compositions was investigated. Figure 6-11a plots v_{SB-1} as a function of the Zr-content for T = 223, 243, 263 and 283 K. For all temperatures studied, the shear-band propagation velocity decreases with increasing Zr-content. Note that for x = 45 and 50 a ductile-to-brittle transition is observed at about 243 K, and therefore v_{SB-1} could not be evaluated at larger T. Such ductile-to-brittle transitions below T_g have already been reported for Vit105 [167] and for a series of gold-based metallic glasses [73]. The temperature-dependent shear-band velocity can now be converted into shear-band viscosities (Figure 6-11b, as an example for T = 243 K) via [168]

$$\eta_{SB} = \tau \, w / v_{SB} \, ,$$

Equation 6-1
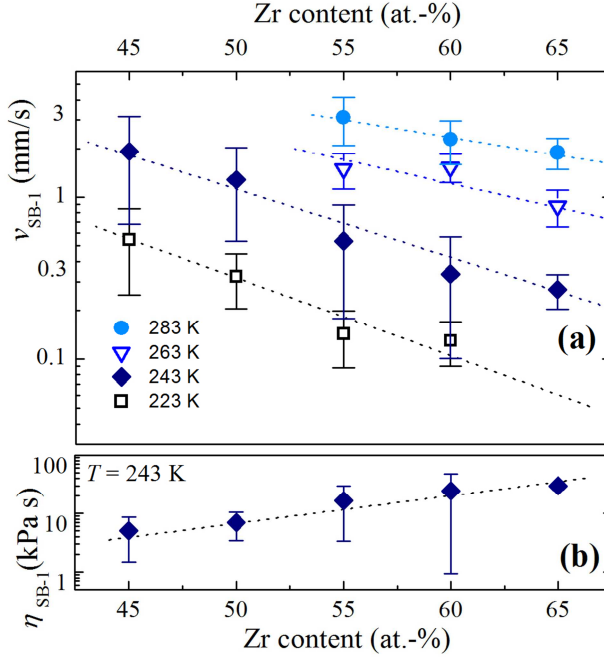
Figure 6-11: (a) Shear-band velocity v_{SB-1} at different temperatures as a function of the Zr-content. (b) Shear-band viscosity at 243 K as a function of the Zr-content. Lines are guides for the eye.

where τ is the shear stress, i.e. $\frac{\sigma_y}{2.01}$, and w is the shear-band thickness, here taken as 10 nm [100, 101, 169]. We have seen that with increasing Zr-content, τ (or σ) decreases (Figure 6-9). The change in this direct stress term over the tested compositions is, however, small compared to the pronounced decrease in $v_{SB.}$. The result of Equation 6-1 is thus a shear-band viscosity proportional to an increasing Zr-content (Figure 6-11b). The material within the shear band thus becomes increasingly viscous with an increasing amount of Zr.
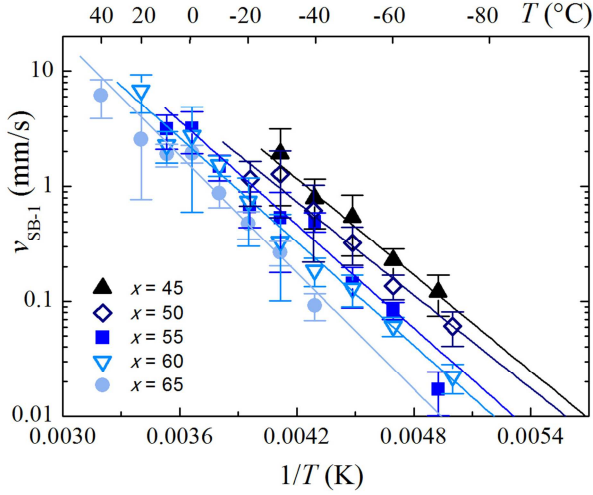
Figure 6-12: Arrhenius representation of the temperature dependence of v_{SB-1}. Lines are fits using a simple Arrhenius-type function.

In agreement with earlier work [120, 130], it was found that the shear-band velocity obeys an apparent Arrhenius behaviour for all alloys. Figure 6-12 displays v_{SB-1} as a function of $1/T$, where the velocities cover almost four orders of magnitude ranging from 0.01 to 10 mm/s over the temperature regime tested. The experimental data are fit with an Arrhenius-type function, for which the resulting lines are also shown in Figure 6-12. We note that the trend in Figure 6-12 is true for any of the five parameters presented in Figure 6-10. Table I summarizes the apparent activation energy, E_{SB-1}, obtained from v_{SB-1}, and an average value, $\bar{E}$, obtained by averaging the apparent activation energies of all evaluation methods. The standard deviation, $\bar{\sigma}$, and the mean fitting error, $\bar{\Delta}$, for $\bar{E}$ are also given.

Table 6-1: Apparent activation energy E_{SB-1}, average activation energy $\bar{E}$, standard deviation $\bar{\sigma}$, and averaged fitting error $\bar{\Delta}$ as a function of the Zr-content x. The data for Vit105 were obtained from Refs. [10,12].

x (at.-%)	E_{SB-1} (eV)	$\bar{E}$ (eV)	$\bar{\sigma}$ (eV)	$\bar{\Delta}$ (eV)
45	0.28 ± 0.09	0.28	-	0.09
50	0.26 ± 0.05	0.29	0.03	0.03
55	0.30 ± 0.03	0.28	0.02	0.02
60	0.30 ± 0.02	0.32	0.02	0.03
65	0.35 ± 0.04	0.35	0.01	0.03
Vit105		0.32	-	0.01

Due to the limited ductility of the $Zr_{45}Cu_{45}Al_{10}$ alloy only v_{SB-1} was used to analyze $\bar{E}$ for that composition. We find that the activation energy ranges from 0.28 to 0.35 eV. Over the entire range of Zr-content, a slight increase in the activation energy is seen, predominantly manifested by $x = 60$ and $x = 65$. For comparison Table I also includes the apparent activation energy for shear-band propagation velocities derived for Vit105 [120, 130].

The experimental data outlined above thus demonstrate a slow-down of the shear-band dynamics of $Zr_xCu_{90-x}Al_{10}$ MGs with increasing Zr-content. Despite the scatter, the corresponding activation energies for the shear-propagation process exhibit an overall trend towards an increasing barrier against sliding with increasing Zr-content. Before searching for the origin of this compositional trend, it is instructive to investigate which of the factors in Equation 3-1 and Equation 3-2, i.e. the stress drop $\Delta\sigma_S = \Delta F/A$ or the event duration Δt, are responsible for the slowdown in kinetics with increasing Zr-content at a given temperature.

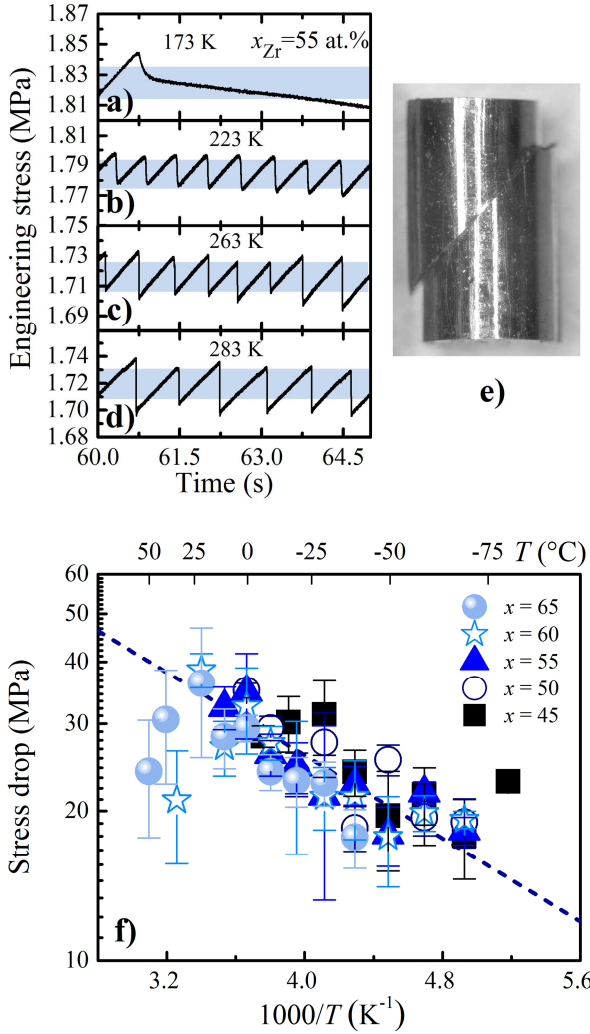**Figure 6-13: (a-d)** Plastic parts of flow curves of $Zr_{55}Cu_{35}Al_{10}$ BMGs (x_{Zr} = 55 at.%) as a function of temperature *T*. **(e)** Stereo-micrograph of a $Zr_{55}Cu_{35}Al_{10}$ BMG deformed to >10%. **(f)** Stress-drop size as a function of $1/T$ for $Zr_xCu_{90-x}Al_{10}$ BMGs (*x* = 45 – 65)

Figure 6-13a-d summarizes the stress-time behaviour as a function of temperature between 173 K and 283 K for the case of x_{Zr} = 55 at.%. The transition from non-serrated to serrated flow occurs below 223 K; this is addressed in more detail below. With a further increase in temperature the subplots b-d show that the serration size increases slightly. To visualize this effect, a blue area is superimposed which represents a height of 1% in flow stress. Figure 6-13e shows a stereo-micrograph of an x_{Zr} = 55 at.% specimen which was plastically deformed to beyond 10%. The plastic strain is concentrated within a single shear band (as in all samples tested in this study). Note that the sample remains in one unfractured piece.

Figure 6-13f summarizes the stress-drop magnitude as a function of inverse temperature for all alloy compositions tested. It was found that the stress drops increase with increasing temperature, with some deviation from this trend at the highest temperatures for x = 60 and x =65. In general, the compositional effect on stress-drop size is small. The monotonically increasing part of the data can be represented by an Arrhenius trend line (see dashed line in Figure 6-13f) with an activation energy of 0.05 eV. At this stage this weak thermal activation can only be regarded as a trend, but the subsequent analysis strengthens the representation chosen in Figure 6-13.

In contrast to the stress-drop size, a clear compositional dependence is observed for the time scale of stress drops at a given temperature. This is shown in Figure 6-14a for a temperature of 243 K. The influence of composition is pronounced: events for x = 65 occur within tens of milliseconds at a rate of approximately 4 GPa/s, whereas for x = 45 a serration slip cycle is accomplished within milliseconds and the dynamics attain rates of over 20 GPa/s. The event duration is thermally activated (Figure 6-14b),

with energies spanning a range of 0.19 eV ($x = 45$) to 0.28 eV ($x = 65$).
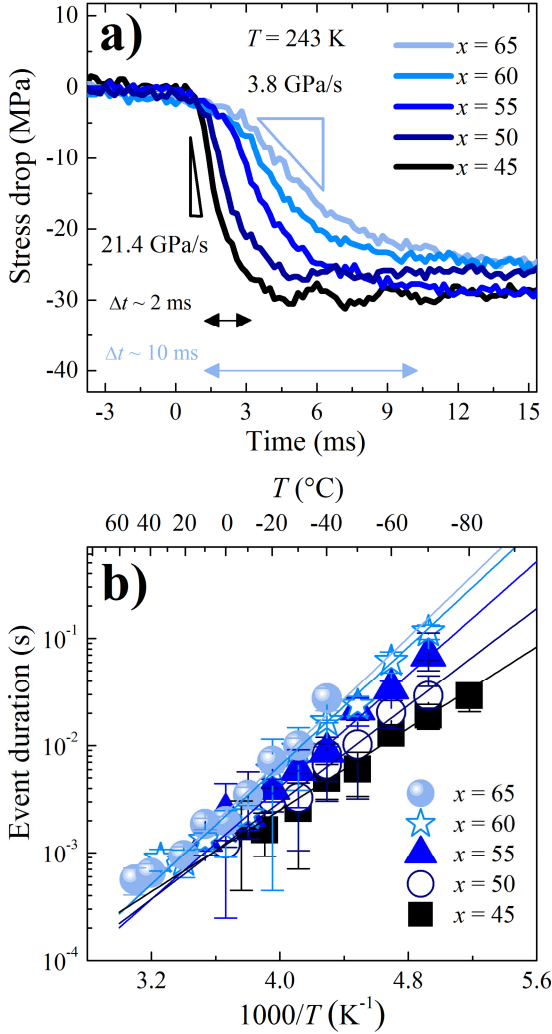
Figure 6-14: Stress drops at 243 K as a function of time for Zr$_x$Cu$_{90-x}$Al$_{10}$ BMGs ($x = 45 – 65$); drop rates and event durations Δt are indicated. (b) Arrhenius representation of the event duration for Zr$_x$Cu$_{90-x}$Al$_{10}$ BMGs.
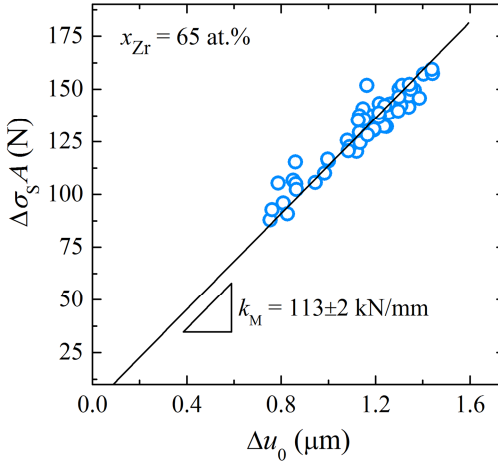
Figure 6-15: Correlation between stress drop size, $\Delta\sigma_S$, and apparent displacement jump, Δu_o, for $Zr_{65}Cu_{25}Al_{10}$ measured at room temperature. The solid line is a linear fit for the data.

As an alternative to investigating the stress-drop size, it is equally instructive to evaluate the simultaneously occurring displacement jump Δu_o. This value represents the elastic reaction of the machine to the drop in stress. It is connected to the stress drop via the relation $\Delta u_0 = \Delta\sigma_S A/k_M$, where A is the sample cross-section and k_M is the machine stiffness (see Figure 6-15 as an example).

The total plastic displacement jump is only obtained after adding a correction term, $\Delta u_{corr} = \Delta\sigma_S A/k_S$, which accounts for the partial elastic recovery of the sample itself, with k_S being the sample stiffness. The total displacement accumulated within a serration is thus $\Delta u_{pl} = \Delta u_0 + \Delta u_{corr} = \Delta\sigma_S A(1/k_M + 1/k_S)$ (see also Equation 3-1). Being thus linearly dependent on each other, the contribution of Δu_o to the dynamics can be fully captured with $\Delta\sigma_S$, with the advantage that $\Delta\sigma_S$ has a higher signal-to-noise ratio.

Following this individual analysis of $\Delta\sigma_S$ and Δt, Figure 6-16 reveals their mutual dependence on each other. Figure 6-16a plots $\Delta\sigma_S$ as a function of $\log(\Delta t)$ for $x = 45, 55, 65$. The testing temperature is indicated via a color code, ranging from blue (193 K) over pink to yellow (313 K). Generally there is a clear correlation, with large stress drops occurring within short durations. With increasing temperature and/or decreasing Zr content, the dynamics shift to shorter time scales, as indicated by the arrows. Using the data displayed in Figure 6-13 and Figure 6-14 it is now possible to distinguish between the effects of time scales and event size (either expressed in $\Delta\sigma_S$ or Δu_{pl}) for the compositional range studied here.

To this end, Figure 6-16b plots the apparent activation energies in a stack column bar plot, with the smaller activation energy for stress drop, $E_S(\Delta\sigma)$, added to the larger activation energy for event duration, $E_S(\Delta t)$, resulting in the total activation energy E_S. A slight trend of an increase in energy barrier with an increase in Zr content is observed. It is also observed that 80-90% of the apparent activation energy arises from the thermal activation of the time scale and only 10-20% from the stress-drop size. As expected from the proportionality of shear-band velocity and $\Delta\sigma_S/\Delta t$, we find that the sum of the two energetic contributions agrees well with the overall activation energies (i.e. activation energies for the shear-band velocity v_{SB}) obtained for the Zr–Cu–Al system (Table 6-1).
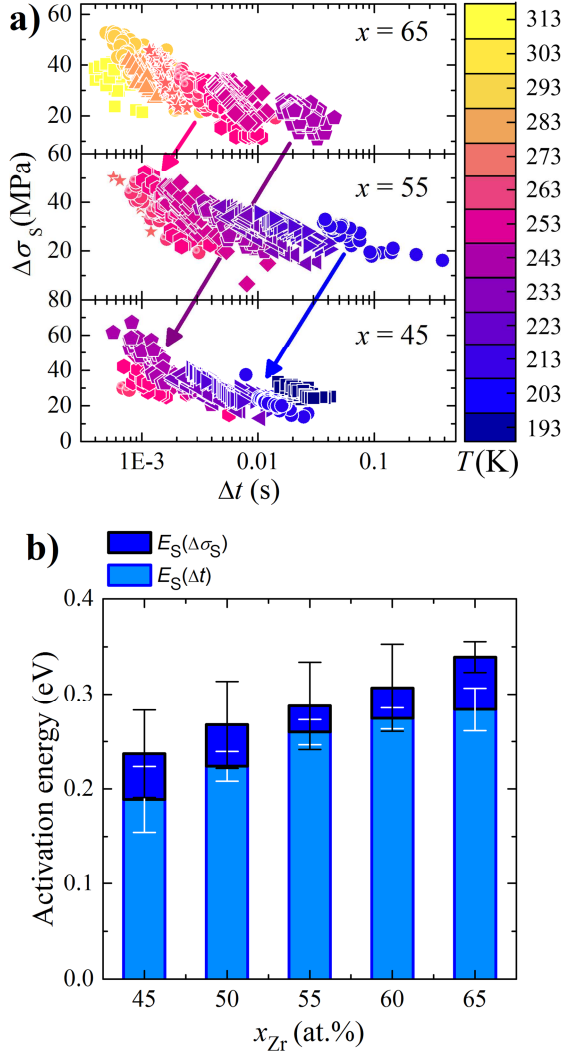
Figure 6-16: (a) Stress-drop size vs. event duration for *x* = 45, 55 and 65. The temperature of the various tests is given by the colour code. Large stress-drops Δσ$_S$ occur within short durations Δ*t*. (b) Compositional dependence of apparent activation energies displayed in a stack column plot, summing activation energies for event duration (*E*$_S$(Δ*t*), light blue) and stress-drop size (*E*$_S$(Δσ$_S$), dark blue). In their sum, they account for the activation energies of the shear-band velocities.

6.2.2. Experimental results on non-serrated flow

Besides serrated flow, shear-band dynamics in the non-serrated flow regime were also assessed via slide-hold-slide tests. Figure 6-17 summarizes the results of the slide-hold-slide experiments. Figure 6-17a shows the aging response for $x_{Zr} = 60$ at.% ($\dot{\varepsilon} = 10^{-3}$ s^{-1}, $T = 173$ K, $t_w = 10$ s) as an example. During the hold phase (dashed region) the stress relaxes markedly, by 14 MPa. Upon reloading, a stress overshoot of $\Delta\sigma_a = 12$ MPa relative to flow stress occurs (indicated by a double arrow). Moderate strain softening is observed (30 MPa per 1% strain) over the full stress-strain curve. Figure 6-17 b shows the compositional dependence of the stress overshoot $\Delta\sigma_a$ after a waiting time of 10 s at 173 K. A clear inverse trend emerges, where $\Delta\sigma_a$ is more than three times larger for $x_{Zr} = 45$ at.% compared to $x_{Zr} = 65$ at.%.
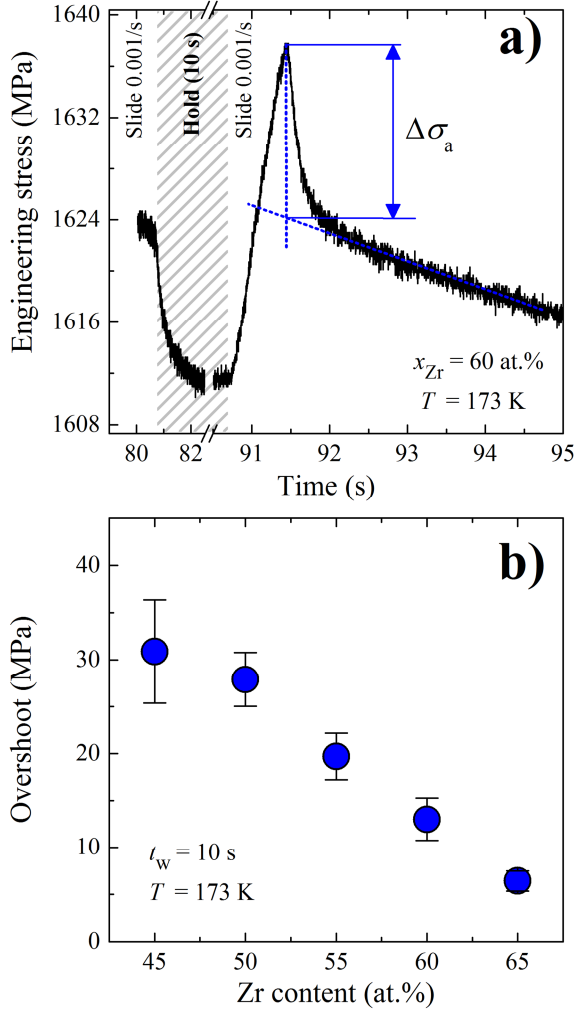
Figure 6-17: (a) Aging experiment of $Zr_{60}Cu_{30}Al_{10}$ ($x_{Zr} = 60$ at.%) at 173 K with a waiting time t_W of 10 s. **(b)** Compositional dependence of $\Delta\sigma_a$ at fixed experimental conditions ($T = 173$ K, $\dot{\varepsilon} = 10^{-3}$ s^{-1}, $t_W = 10$ s).

6.2.3. Experimental results on flow-transitions and ductility

The range of experiments carried out during this study enables us to draw a representative composition-temperature map which includes information on flow mode and malleability (Figure 6-18). Each data point corresponds to tests carried out according to the specifications given by the coordinates (composition, temperature) and a strain rate of 10^{-3} s^{-1}. The symbols contain additional information about the apparent flow mode. Circles indicate non-serrated flow and squares indicate serrated flow. In addition, the degree of symbol-filling refers to the observed malleability ranges displayed in the legend: full symbols indicate a malleability greater than 10%; less filling indicates a range of intermediate malleability; and crosses symbolize conditions under which negligible malleability(<1%) was observed. The crosses thus indicate a transition
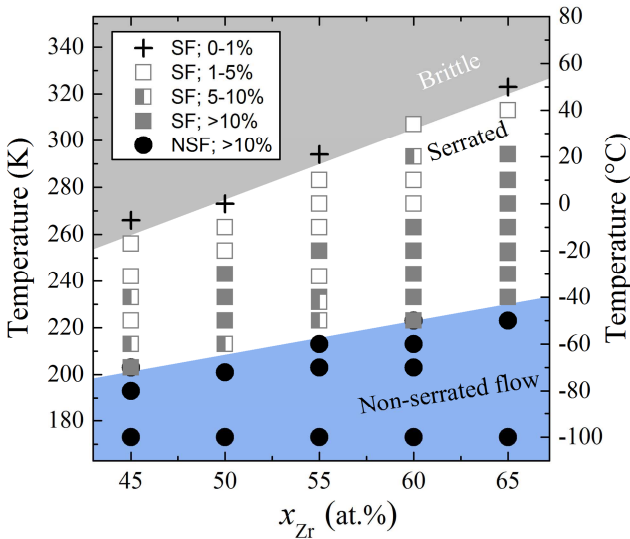
Figure 6-18: Temperature-composition map indicating deformation mode (circles: non-serrated flow, squares: serrated flow) and malleability; the latter ranges from > 10% (full symbols) over 1-10% (half-filled and empty symbols) to < 1% (crosses).

from ductile to brittle behaviour. The map shows that the transition from non-serrated to serrated flow, T_T, occurs in a temperature regime ranging from 203 to 223 K, shifting to higher temperatures for Zr-rich alloys. The results for malleability show a transition at moderately low temperatures (263 K) for Zr-lean alloys, rising to above room temperature (323 K) for alloys with higher Zr content.

6.2.4. Discussion

The above results clearly demonstrate the strong influence of composition on the dynamics of shear-band propagation and relaxation in BMGs. These first experimental insights into a topic that links mechanical stability and composition are summarized phenomenologically below and then discussed on the basis of short- and medium-range order, bond strength, and elastic constants.

Table 6-2: Overview on composition dependence of shear-band dynamics.

Parameter	Zr ↑
$\Delta\sigma_a$	↓
Δt	↑
$\Delta\sigma_S$, Δu_{pl}	→
v_{SB}	↓
η_{SB}	↑
E_S	↑
T_T	↑
T_{DTB}	↑
T_g	↓

General trends in shear-band dynamics with changes in alloy composition

First, we discuss the trends in dynamics revealed in the present intra-system study of $Zr_xCu_{90-x}Al_{10}$ BMGs with respect to Table 6-2. Apart from a decrease in T_g, seven dependencies with increasing Zr-content are observed: i) the stress overshoot $\Delta\sigma_a$ during shear-band aging decreases; ii) the serration duration Δt increases; this, together with iii) an almost constant stress-drop size $\Delta\sigma_S$ or slip-size magnitude Δu_{pl}, leads to iv) a decreasing shear-band velocity (v_{SB}) and v) an increasing shear-band viscosity η_{SB}; vi) the activation barrier E_S for shear-band propagation increases slightly; and vii) both the transition temperature from non-serrated flow to serrated flow, T_T, and from ductile to brittle behaviour, T_{DBT}, shift to higher temperatures.

These observations are self-consistent. A weaker aging response (i.e. a smaller stress overshoot $\Delta\sigma_a$) indicates a larger barrier for structural relaxation. Pronounced thermally-activated relaxation has been suggested as being responsible for lowering the strain-rate sensitivity (SRS) when temperature is increased or strain rate decreased, eventually turning it negative [163, 167]. Using a detailed theoretical approach [138] it has meanwhile been demonstrated that upon lowering the strain rate, the required athermal driving stress decreases while relaxation processes are dynamically less suppressed. Therefore an additional stress contribution that works against relaxation is required to maintain the applied strain rate. With the relaxation processes becoming more and more dominant (at increased temperatures or decreased strain rates), the increase in required thermal stress upon a further lowering of the strain rate will eventually overcompensate the drop in required athermal stress. This leads us to observe that the system becomes

slower at higher stresses, generating the effect of a negative SRS. The temperature at which this transition from positive to negative SRS occurs at a given strain rate (e.g. $10^{-3}s^{-1}$) defines the transition temperature, T_T, from non-serrated to serrated flow. A greater activation energy shifts the flow transition to higher temperatures, agreeing with the compositional trend seen in Table 6-2, where $\bar{E} = E_S$ increases with an increase in Zr content (see also Figure 6-16).

The shear-band velocity, in turn, is closely linked to this transition (see e.g. Figure 3-8). It provides an upper boundary for how high the applied strain rate must be to suppress the relaxation processes enough to turn the SRS from negative to positive values. Accordingly, the difference between applied strain rate and shear-band velocity is the smallest for measurement conditions near the flow transition. This means that when comparing different compositions at a given temperature and strain rate, shear bands are slowest in the alloy with T_T closest to the testing temperature, i.e. in the Zr-rich alloys (see Figure 6-18). Finally, the activation energy of that transition, E_S, is expected to be directly connected to the activation energy for aging, because it is that barrier that is linked to structural freezing [136], which in turn represents the later fraction of a shear-banding cycle. In fact, it has been shown theoretically (see Appendix D in Ref. [138]) that E_S is about three times the activation energy for aging E_a in Vit105.

There are also various indications of a thermally-induced ductile-to-brittle transition within the Zr–Cu–Al BMG system. In particular, brittle failure occurs at higher T if the Zr content is large. This coincides with the slower shear dynamics observed and points to a dynamic contribution to embrittlement, which is a concept well established in literature [77, 78]. Whereas we find the dynam-

ic quantities to accord with each other, we observe, however, that a slower shear-band dynamics correlates with a lower glass-transition temperature. At a given temperature shear bands in alloys with x = 65 at.% are the slowest, although the homologous temperature T/T_g is the highest, indicating that T_g is an insufficient parameter for predicting trends in the dynamics of shear bands.

The same also holds for viscosities obtained directly in the super cooled liquid regime [170]: they follow a compositional trend opposite to the shear-band viscosities displayed in Figure 6-11b; i.e. the equilibrium viscosities in the super cooled liquid range are lowest for Zr-rich alloys. Clearly, absolute viscosity values should not be directly compared, because the shear-band viscosity describes a transient, nanoscopically confined state. However, if the effective temperature rise upon yielding was the same for all alloys, one would expect that the mere compositional trend of shear-band viscosity would be identical to that found in equilibrium. Our measurements show that this is not the case, pointing to an effective temperature rise ΔT_e that is indeed composition-dependent, meaning that shear bands in Zr-poor alloys undergo a larger ΔT_e. From that consideration, the immediate question emerges, whether different alloys share a common effective-temperature base line. In other words, does ΔT_e represent a structural change that transforms similar initial configurations (glassy states) to greatly differing activated configurations (liquid-like shear bands), or does it rather represent a transformation from initially disparate configurations towards structurally more similar activated states? Fictive temperatures of glasses at rest are expected to be very different because of production history and composition-specific medium-range order (interconnectivity). In an active shear band, on the other hand, the pre-history of the production is erased due to the high shear rate, and also medium-range order degenerates, such
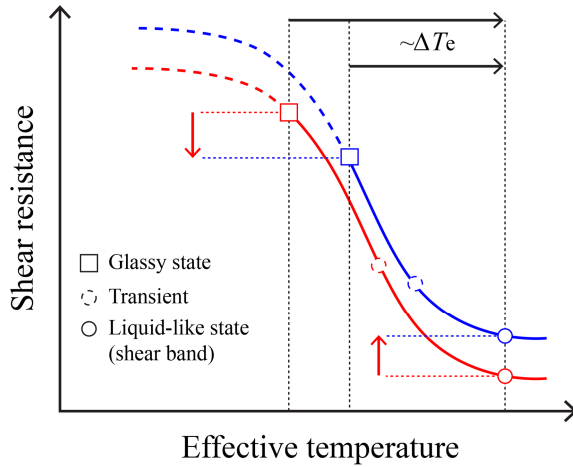
Figure 6-19: Composition-dependent effective-temperature rises.

that the "dual" structure of hard and soft zones becomes homogenised. These points clearly support the second scenario, i.e. an effective- temperature jump transforming disparate "ground states" into a comparable agitated structural state. This perception is illustrated schematically in Figure 6-19 for two different alloys (red and blue) via an ideal dependence of shear resistance on structural state for two different compositions, red and blue, here described by the effective temperature. At low effective temperature the shear-resistance is high, while it is low at high effective temperatures. The offset between the curves is due to the different compositions. In the glassy state (squares), the effective temperatures of the two alloys differ considerably. If we assume identical cooling histories, this difference originates mostly from the topological limit of effective medium-range order packing. In the example of Figure 6-19, the glassy structure of the red alloy is packed more densely. As a consequence, the shear resistance is larger in the red alloy than in the blue one, although the blue curve is generally shifted towards higher shear resistances. Upon shear-band initia-

tion, medium-range order is degenerated and effective temperature is increased to comparable values (circles). At this effective temperature, which is then more or less the same for both alloys, the blue alloy shows the larger resistance towards shear. The idea depicted in Figure 6-19 thus neatly explains why Zr-lean glasses show a larger yield stress (i.e. larger shear-resistance of the glassy structure) but a lower resistance towards shear in the liquid-like shear-band state. The discrepancy between viscosities of the super cooled liquid and of the shear-band indicates that medium-range order may still be well pronounced in the super cooled liquid state.

This entire consideration implies the existence of a structure-property relation between shear-band dynamics, i.e. the energy E_S, and the structure of the agitated shear-band state. This idea is investigated in the following.

Chemical and topological aspects of shear-band dynamics in $Zr_xCu_{90-x}Al_{10}$

This section attempts to relate the shear-band dynamics and its decrease with increasing Zr content to the structure of the glass. Basics on MG structure were introduced in section 2.3. To briefly summarize, the MG structure is viewed as a rigid backbone of interconnected, efficiently packed clusters, enclosing islands of decreased density and less efficient packing. The disorder of the structure is greater in an active shear band than in the matrix. This is caused by the net effect of driven disordering processes and counteracting structural relaxations, i.e. processes governing the re-establishment of the quasi-equilibrium structure. A simple but powerful treatment of such a balance in inhomogeneous BMG deformation has been provided by Spaepen [41], where the two counteracting processes are stress-induced generation of free volume (i.e., free volume that is produced by squeezing an atom into a

sub-sized atomic hole) and annihilation of that free volume by a small series of diffusive jumps. The easier these diffusive jumps are, the faster the structural relaxation and the faster the shear-band velocities. The size of the energy barrier for annihilating free volume by diffusive jumps naturally depends on local chemistry, or more precisely on the bonding strength between an atom in a potential jumping site and its immediate neighbourhood. It can therefore be inferred that structural relaxation, and thus shear-band dynamics, will be slow where strong bonding exists.

We will now test this hypothesis for the compositions studied in this work. The activation barrier for diffusive jumps will differ for each species (Zr, Cu, Al). In the following we focus on the activation barrier for diffusion of copper, for several reasons. (i) Cu, with a radius of 126 pm, is the smallest atomic species in the system; thus it can annihilate free volume by jumping into sites that are inaccessible for larger Zr or Al atoms – or, in other words, the probability of finding a Cu atom in a potential jumping site is larger for Cu than for the other species. (ii) Copper has a valence electron number of 1 e$^-$/atom compared to 4 e$^-$/atom for Zr and 3 e$^-$/atom for Al [171], i.e. the contribution of Cu to a bond is expected to be almost ideally metallic, thus non-directional, which allows Cu to diffuse through the material relatively freely. iii) In quantifying solidity and liquidity in MD simulated binary Cu–Zr, Ding et al. [34] showed that all Cu atoms not involved in icosahedra are centring motifs with a decreased solidity index compared to Zr-centred clusters; consequently, in a shear band, where the backbone is degraded, the probability of Cu rearranging in a non-affine way is greater than for Zr. iv) Another recent MD study [33], simulating structural relaxation, revealed that Cu-centred icosahedra become the dominant Cu-centred motif much more quickly than Zr-centred Kasper-polyhedra, which also indicates that Cu

diffusion is faster than Zr diffusion. In fact, an increased diffusivity of Cu in MD simulations of Cu–Zr binary metallic glass has also been reported [172]. Assuming a similar difference in atomistic dynamics between Cu and Zr in the ternary Zr–Cu–Al system as in the binary Cu–Zr glass [(iii), (iv)], the above-mentioned four points provide a good working hypothesis for the identification of diffusive rearrangement of copper as the dominant process for structural relaxation in shear bands of the Zr–Cu–Al BMGs tested here.

We now elaborate on how the bonding strength between a Cu atom and its immediate surroundings depends on composition. A fully comprehensive understanding of the non-directional metallic bonding in alloys can be achieved by ab-initio calculations, but this is beyond the scope of this project. Instead we apply a simple treatment of bonding energies for different bonding pairs. Here the relevant bonding pairs for a Cu-centered cluster are Cu–Cu, Cu–Zr, and Cu–Al. The fractions $c_{i,j}^{s}$ of the species in the first coordination shell determine the extent to which the strength of each bonding pair will contribute to the total bond energy. With the picture of typical clusters representing the majority of the structure, and with the assumption that there is no chemical short-range order, the local fractions of the species within such a cluster are expected to equal the alloy's nominal compositions c_j [28]. Consequently, the first coordination shell around copper will be slightly depleted in copper, since the centre Cu atom has to be left out of the calculations of shell concentration. The shell concentration can be determined as the partial coordination number [28] of a specific element i around the central copper atom, divided by the total coordination number of copper, $N_{Cu,tot}$, i.e.:

$$c_{Cu,Zr}^{s} = \frac{(N_{Cu,tot}+1)c_{Zr}}{N_{Cu,tot}} \, ,$$

$$c_{Cu,\,Al}^{s} = \frac{(N_{Cu,tot}+1)c_{Al}}{N_{Cu,tot}} \, ,$$

$$c_{Cu,\,Cu}^{s} = \frac{(N_{Cu,tot}+1)c_{Cu}-1}{N_{Cu,tot}} \, ,$$

<div align="right">**Equation 6-2**</div>

where c_j is the nominal composition of element j.

For simplicity, we approximate the coordination numbers according to those predicted by the ELAP model, acknowledging that these will slightly overestimate the packing efficiency of the disordered shear-band structure. A further aspect we must consider when assessing the bonding energy of Cu to its neighbours is the fact that a large atom has more neighbours (large $N_{i,tot}$) than a small atom, which means that its contribution to one specific bond is comparatively smaller. We account for this by weighting the local concentrations of the species in the first coordination shell by the inverse of their respective total coordination number:

$$c_{Cu,i}^{s,eff} = \frac{c_{Cu,i}^{s}\dfrac{1}{N_{i,tot}}}{\sum_{m=i,j,k} c_{Cu,m}^{s}\dfrac{1}{N_{m,tot}}} \, .$$

<div align="right">**Equation 6-3**</div>

These effective concentrations reflect the share of each bonding pair type (for Cu: Cu–Cu, Cu–Zr, and Cu–Al) in the character of the total bond. Coordination numbers and effective concentrations are given in Table 6-3.

Table 6-3: Zr fraction x_{Zr}; activation energy for Δt, $E_{s}(\Delta t)$; total coordination number around copper $N_{Cu,tot}$; partial coordination numbers around copper $N_{Cu\text{-}j}$; total coordination numbers $N_{j,tot}$; and effective concentrations $c_{Cu,j}^{s,eff}$ for for j = Cu, Zr and Al.

x_{Zr} (at.%)	$E_{s}(\Delta t)$ (eV)	$N_{Cu,tot}$	$N_{Cu\text{-}Cu}$	$N_{Cu\text{-}Zr}$	$N_{Cu\text{-}Al}$	$N_{Zr,tot}$	$N_{Al,tot}$	$c_{Cu,Cu}^{s,eff}$	$c_{Cu,Zr}^{s,eff}$	$c_{Cu,Al}^{s,eff}$
45	0.19 ± 0.03	10.95	4.37	5.37	1.19	15.088	13.242	0.472	0.421	0.107
50	0.22 ± 0.02	10.81	3.73	5.91	1.18	14.892	13.074	0.414	0.477	0.109
55	0.26 ± 0.01	10.69	3.09	6.43	1.17	14.703	12.914	0.354	0.535	0.111
60	0.27 ± 0.01	10.57	2.47	6.94	1.16	14.518	12.760	0.291	0.596	0.113
65	0.28 ± 0.02	10.45	1.86	7.45	1.15	14.34	12.61	0.226	0.659	0.115

As the Zr content increases, the total coordination numbers decrease by about 5% for all species. The effective compositions of copper, zirconium and aluminium follow the nominal compositions very closely. This happens mostly because the decreased concentration of Cu in the 1st coordination shell of a copper atom (Equation 6-2) is effectively compensated by the larger contribution of Cu atoms to specific bonds due to the fact that they have the smallest total coordination number (Table 6-3). For the $Zr_xCu_{90-x}Al_{10}$ BMG system this means that the bonding character around Cu, $c_{Cu,j}^{s,eff}$, is essentially represented by the nominal composition. The results in Table 6-3 imply that the compositional effect on the bonding of Cu to its surrounding atoms is equivalently described as a shift of bond character from Cu–Cu like to Cu–Zr like as the Zr content increases.

Having simplified the compositional effect to a question of Cu–Cu and Cu–Zr bonds, our task is now to compare the bonding strengths of these two bonding pairs. The mixing enthalpy of -23 kJ/mol [59] between Cu–Zr is a first indication that Cu–Zr bonds are stronger than Cu–Cu bonds. However, the mixing enthalpy is not an absolute value. It only describes how the energy of Cu–Zr bonds compares to the averaged energy of Cu–Cu and Zr–Zr bonds. Thus a comparison of energies between Cu–Cu bonds and Cu–Zr bonds is only possible when it is known how the energies of like bonds, i.e. Cu–Cu and Zr–Zr, compare to each other. This information can be obtained by comparing the heats of formation of the pure components. With 609 kJ/mol for Zr [173], this value is almost double that of Cu (337.4 kJ/mol). Thus the average energy of Cu–Cu and Zr–Zr bonds has already exceeded the Cu–Cu bond strength. Combined with the negative mixing enthalpy, it is thus very reasonable to consider a Cu–Zr bond to be stronger than a

Cu–Cu bond. On this basis, we conclude that the activation energy for diffusive jumps of Cu in Zr-lean compositions is considerably less than in Zr-rich compositions, because of the substitution of Cu–Zr bonds by weaker Cu–Cu bonds in the Zr-lean alloys. This explains why structural relaxation, and thus shear-band dynamics, in the Zr-lean alloys is faster.

At this point we should note that we have not yet taken applied stress into consideration. Presumably, stress around a squeezed-in atom will lower the migration enthalpy of its neighbours and bias their movement towards regions of lower stress, thus promoting structural relaxation. For Zr–Cu–Al this means that relaxation in Zr-lean alloys is further facilitated because the yield stress increases with decreasing Zr content (see Figure 6-9). Hence we find that faster shear-band dynamics in Zr-lean compositions is promoted by both (i) a decrease in bonding strength of the fastest diffusor to its nearest neighbours and (ii) an increase in stress-assistance to relaxation processes. Further, the yield stress is connected to the shear modulus G by the universal yield criterion for BMGs [7]. Expecting a lower G for Zr-rich compositions also agrees with the theory of elastic modulus inheritance [47], because $G_{Zr}<G_{Cu}$. Thus, a trend of decreasing dynamics with decreasing shear modulus emerges for the system investigated in this study. This direct correlation of shear-band dynamics and shear modulus is interesting, because a low shear modulus is also correlated with increased BMG plasticity in Refs. [46, 81, 82, 85]. This indeed matches our observed increase in the ductile-to-brittle transition temperature, T_{DTB}, with increasing Zr content (Figure 6-18), and thus decreased shear modulus and slower shear-band dynamics.

6.2.5. Summary

In summary, we have investigated the shear-band dynamics of the $Zr_xCu_{90-x}Al_{10}$ (x = 45 – 65) BMG system over a temperature range of 173 K to 323 K, which includes the non-serrated to serrated flow transition and a well-defined transition from malleable to brittle behaviour. The shear-band dynamics becomes slower with increasing Zr content, characterized by a higher activation barrier for Zr-rich compositions. No scaling with the glass transition temperature is observed. Instead, the trends in shear-band dynamics can be attributed to a change in overall bonding strength between the fastest diffusor, Cu, and its nearest neighbours. This bonding strength is found to decrease with decreasing Zr content, because the bonding contribution of strong Cu–Zr bonds progressively decreases at the cost of an increasing contribution of weaker Cu–Cu bonds. Given that the Zr-rich alloys (x = 60 and x = 65) are the most ductile within the alloy system investigated, we conclude that the lower shear modulus, in combination with the lower atomic mobility of the smallest species (Cu), enhances stable shear-band propagation and thus plastic flow in Zr-rich glasses.

6.3. Shear-band dynamics in different alloy systems: an inter-system study[3]

In this study we investigated a series of bulk MGs with extended malleability in order to obtain a consistent picture of the influence of topology and chemistry on the dynamics of shear banding. We
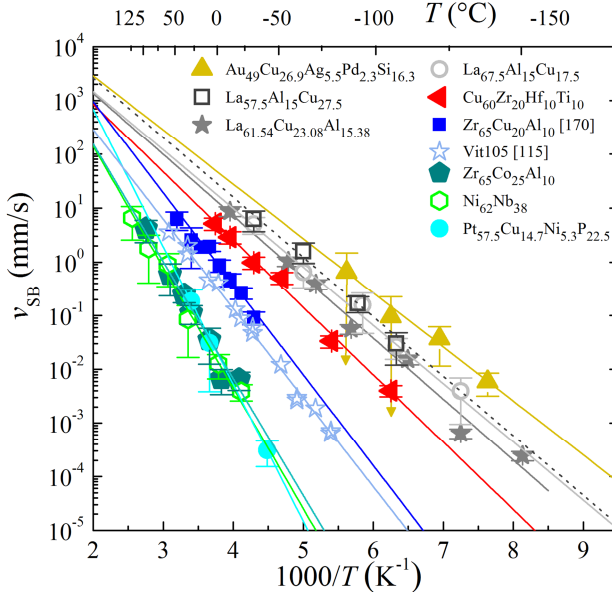
Figure 6-20: Arrhenius plot of the shear-band velocity for a series of MGs with different base metals. The two yellow arrows represent error bars exceeding the logarithmic scale of the y-axis.

achieved this by extending our work on Zr-based MGs [120, 174] to a large variety of MGs with different base elements, including $Au_{49}Cu_{26.9}Ag_{5.5}Pd_{2.3}Si_{16.3}$, $Cu_{60}Zr_{20}Hf_{10}Ti_{10}$, $La_{57.5}Cu_{27.5}Al_{15}$,

---

[3] Corresponding publication:

(1) P. Thurnheer, R. Maaß, K. J. Laws, J. F. Löffler. How topology and chemistry determine shear stability in metallic glasses (in preparation).

$La_{61.54}Cu_{23.08}Al_{15.38}$, $La_{67.5}Cu_{17.5}Al_{15}$, $Ni_{62}Nb_{38}$, $Pt_{57.5}Cu_{14.7}Ni_{5.3}P_{22.5}$, and $Zr_{65}Co_{25}Al_{10}$. We show that this set of alloys covers a ΔE_S range of 0.31 eV, which allows us to thoroughly assess the influence of E_S on the mechanical properties of MGs for the first time. Figure 6-20 shows the temperature- and composition-dependent shear-band velocities of the alloys investigated. These velocities range from 10^{-4} to 10 mm/s in the temperature range investigated, and activation energies E_S range from 0.18 eV for $Au_{49}Cu_{26.9}Ag_{5.5}Pd_{2.3}Si_{16.3}$ to 0.51 eV for $Pt_{57.5}Cu_{14.7}Ni_{5.3}P_{22.5}$. The point of intersection of the different fits in Figure 1 with the ordinate at $1/T = 0$ is located at values which are on the order of 0.5 to 5 km/s, i.e. in the range of phonon velocities. This upper limit can be converted into a viscosity using the relation $\eta = \sigma_y w/(2v_{SB})$, where σ_y is the uniaxial yield stress and w is the shear-band thickness. With $w \approx 15$ nm [109] and $\sigma_y \approx 2$ GPa, η_{SB} ranges from 3×10^{-3} to 3×10^{-2} Pa s, which are values that agree well with experimental data for the high-temperature limit of viscosity η_0 [175]. As a consequence of this similar upper velocity limit to all compositions, the alloy with the smallest activation energy shears fastest at a given temperature. It is noted that in this study, room-temperature plasticity was only encountered for alloys with $E_S \geq 0.3$ eV. Because the underlying atomistic mechanisms which govern shear-band dynamics have been convincingly attributed to relaxation processes [136], the data in Figure 6-20 provide evidence that the relaxation rate and its barrier energy E_S depend strongly on chemistry. Table 6-4 lists the current results (E_S) together with those of previous work [120, 176], plus additional data from literature for the alloys $Co_{78}Si_{10}B_{12}$, $Ni_{70}Fe_8Si_{10}B_{12}$ and $Pd_{78}Cu_6Si_{16}$ (all Ref. [116]) and $Zr_{65}Cu_{15}Ni_{10}Al_{10}$ (Ref. [139]). In order to have a consistently evaluated set of E_S values we re-evaluated the data in Fig. 4 of Ref. [139], which produced an activation energy of 0.37 eV for $Zr_{65}Cu_{15}Ni_{10}Al_{10}$ rather than the reported 0.56 eV.

Table 6-4: Activation energy of the shear-band velocity E_S for various MG alloys.

Alloy	$-E_S$ (eV)
$Au_{49}Cu_{26.9}Ag_{5.5}Pd_{2.3}Si_{16.3}$	0.2 ± 0.01
$Co_{78}B_{12}Si_{10}$	0.48 ± 0.05 [116]
$Cu_{60}Zr_{20}Hf_{10}Ti_{10}$	0.25 ± 0.01
$La_{67.5}Cu_{17.5}Al_{15}$	0.22 ± 0.009
$La_{61.54}Cu_{15.38}Al_{23.08}$	0.23 ± 0.005
$La_{57.5}Cu_{27.5}Al_{15}$	0.22 ± 0.02
$Ni_{70}Fe_8B_{12}Si_{10}$	0.46 ± 0.05 [116]
$Ni_{62}Nb_{38}$	0.44 ± 0.03
$Pd_{78}Si_{16}Cu_6$	0.35 ± 0.04 [116]
$Pt_{57.5}Cu_{14.7}Ni_{5.3}P_{22.5}$	0.51 ± 0.09
$Zr_{65}Co_{25}Al_{10}$	0.43 ± 0.03
$Zr_{65}Cu_{15}Ni_{10}Al_{10}$	0.37 ± 0.04 [139]
$Zr_{65}Cu_{25}Al_{10}$	0.35 ± 0.03 [176]
$Zr_{60}Cu_{30}Al_{10}$	0.32 ± 0.03 [176]
$Zr_{55}Cu_{35}Al_{10}$	0.28 ± 0.02 [176]
$Zr_{52.5}Cu_{17.9}Ni_{14.6}Al_{10}Ti_5$	0.32 ± 0.001 [120]
$Zr_{50}Cu_{40}Al_{10}$	0.29 ± 0.03 [176]
$Zr_{45}Cu_{45}Al_{10}$	0.28 ± 0.09 [176]

Where known, the uncertainties in E_S reflect the error of the Arrhenius fit. If this deviation is not known, a typical error of $\pm 10\%$ is assumed. The question now emerges as to what property of the strain-softened flowing shear-band material determines the general trend in Figure 6-20 and therefore shear-stability in MGs.

Shear stability or plasticity in MGs has been brought into relation with a set of various glass properties, such as the glass transition temperature T_g, the alpha transition energy E_α, the Poisson's ratio v, the potential energy barrier for shear-transformation zones W_{STZ}, and the liquidus temperature T_l. The correlation of the acti-

vation energy E_S with these "usual suspects" is investigated in the following. For this purpose, the alloy-specific mechanical and thermo-physical properties are compiled in Table 6-5 and Table 6-6. If values for the exact compositions were not available, values of a very close composition were used (see column: alternative alloy).

Table 6-5: Mechanical properties of the alloys; i.e. the Poisson's ratio *v*, the shear modulus *G* and the yield stress σ_y. If the corresponding property of an investigated alloy was not known, the property of a close composition (alternative alloy) was used.

Alloy	*v* [46]	*G* [46] (GPa)	Alternative alloy	σ_y (GPa)	Alternative alloy
$Au_{49}Cu_{26.9}Ag_{5.5}Pd_{2.3}Si_{16.3}$	0.406	26.5		1.32	
$Co_{78}B_{12}Si_{10}$	0.31	75	Pure Co	3.45[177]	$Co_{72.5}Si_{12.5}B_{15}$,
$Cu_{60}Zr_{20}Hf_{10}Ti_{10}$	0.369	36.9		1.95	
$La_{67.5}Cu_{17.5}Al_{15}$	0.33	13.4	$La_{66}Al_{14}Ni_{10}Cu_{10}$	0.6	
$La_{61.54}Cu_{23.08}Al_{15.38}$	0.33	13.4	$La_{66}Al_{14}Ni_{10}Cu_{10}$	0.7	
$La_{57.5}Cu_{27.5}Al_{15}$	0.33	13.4	$La_{66}Al_{14}Ni_{10}Cu_{10}$	0.64	
$Ni_{70}Fe_8B_{12}Si_{10}$	0.31	76	Pure Ni	3.6[178]	$[(Ni_{80}Fe_{20})_{0.75}B_{0.2}Si_{0.05}]_{96}Nb_4$
$Ni_{62}Nb_{38}$	0.385	66.3	$Ni_{60}Nb_{35}Sn_5$	3.2	
$Pd_{78}Si_{16}Cu_6$	0.411	32.9		1.57[46]	$Pd_{77.5}Si_{16.5}Cu_6$
$Pt_{57.5}Cu_{14.7}Ni_{5.3}P_{22.5}$	0.42	33.3		1.4	
$Zr_{65}Co_{25}Al_{10}$	0.364	33.9	$Zr_{56}Co_{28}Al_{16}$	1.7	
$Zr_{65}Cu_{15}Ni_{10}Al_{10}$	0.355	30.3		1.45[179]	$Zr_{62.55}Cu_{17.55}Ni_{9.9}Al_{10}$
$Zr_{65}Cu_{25}Al_{10}$	0.375	28.4	$Zr_{65.025}Al_{10}Cu_{14.85}Ni_{10.125}$	1.6	
$Zr_{60}Cu_{30}Al_{10}$	0.374	29.8	$Zr_{60.525}Cu_{19.35}Ni_{10.125}Al_{10}$	1.65	
$Zr_{55}Cu_{35}Al_{10}$	0.369	31.7	$Zr_{55}Al_{10}Ni_5Cu_{30}$	1.75	
$Zr_{52.5}Cu_{17.9}Ni_{14.6}Al_{10}Ti_5$ (Vit105)	0.37	31.8		1.8	
$Zr_{50}Cu_{40}Al_{10}$	0.37	31.8	$Zr_{52.5}Cu_{17.9}Ni_{14.6}Al_{10}Ti_5$	1.8	
$Zr_{45}Cu_{45}Al_{10}$	0.364	36.3		1.95	

Table 6-6: Thermo-physical properties of the alloys; i.e. the glass transition temperature T_g, the liquidus temperature T_l, the fragility index m, the fragility parameter D^* and the alpha-transition energy E_α. If a property of an investigated alloy was not known, the property of a close composition (alternative alloy) was used. If only one of the parameters m or D^* was found in literature, the other one was obtained by applying the analytic conversion between the two parameters according to [180]. These cases are marked with the symbol [†].

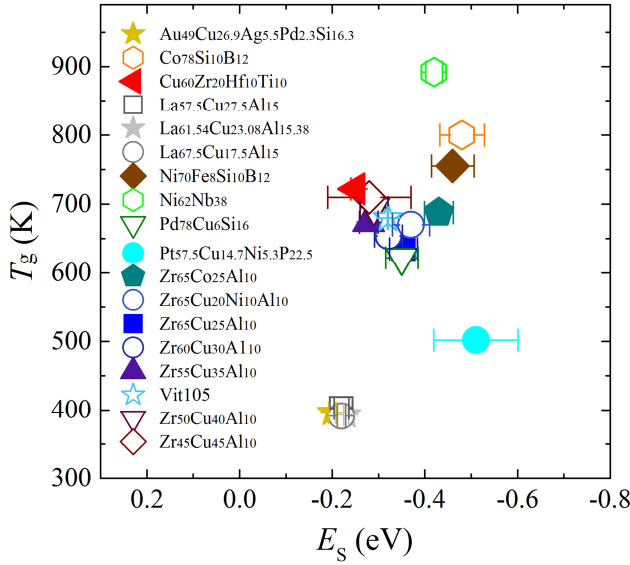| Alloy	T_g (K)	T_l (K)	m	D^*	Alternative alloy	E_α (kJ/mol)
$Au_{49}Cu_{26.9}Ag_{5.5}Pd_{2.3}Si_{16.3}$	401	644[148]				
$Co_{78}B_{12}Si_{10}$	800[177]	1352[181]			$Co_{72.5}B_{15}Si_{12.5}/Co_{70}Fe_5Si_{15}B_{10}$	
$Cu_{60}Zr_{20}Hf_{10}Ti_{10}$	722	917				
$La_{67.5}Cu_{17.5}Al_{15}$	391	713				
$La_{61.54}Cu_{23.08}Al_{15.38}$	393	751	43[180]	$21.8^\dagger$	$La_{55}Al_{25}Cu_{20}$	140.43
$La_{57.5}Cu_{27.5}Al_{15}$	402	721				
$Ni_{70}Fe_8B_{12}Si_{10}$	755[178]	1381[178]			$[(Ni_{0.8}Fe_{0.2})_{0.75}B_{0.2}Si_{0.05}]_{96}Nb_4$	
$Ni_{62}Nb_{38}$	892	1223	$121^\dagger$	5.6[175]	$Ni_{59.5}Nb_{40.5}$	896.91
$Pd_{78}Si_{16}Cu_6$	622[182]	812[183]	73[180]	11.1[180]		377.32
$Pt_{57.5}Cu_{14.7}Ni_{5.3}P_{22.5}$	502	547	$52^\dagger$	16.4[184]		216.06
$Zr_{65}Co_{25}Al_{10}$	688	1050				
$Zr_{65}Cu_{15}Ni_{10}Al_{10}$	670	895	35[180]	$31.02^\dagger$	$Zr_{65}Al_{7.5}Ni_{10}Cu_{17.5}$	194.87
$Zr_{65}Cu_{25}Al_{10}$	635	938				
$Zr_{60}Cu_{30}Al_{10}$	654	956				
$Zr_{55}Cu_{35}Al_{10}$	674	935				
$Zr_{52.5}Cu_{17.9}Ni_{14.6}Al_{10}Ti_5$ (Vit105)	680	874	$52^\dagger$	17[175]		293.84
$Zr_{50}Cu_{40}Al_{10}$	695	892				
$Zr_{45}Cu_{45}Al_{10}$	710	896				

Figure 6-21: Activation energy E_S vs. glass-transition temperature T_g.

i) Glass transition temperature: Results based solely on one alloy system suggested that there is a linear correlation between T_g and E_S [176]. A summary of both parameters for all alloys investigated (Figure 6-21) illustrates, however, that this is not generally the case. Because the shear-band material is believed to be in the structural state of an undercooled liquid above T_g [185], rather than at the gelation point of the glass [186], different physical origins for T_g and E_S are in fact expected.

ii) *Alpha transition energy*: MG plasticity was related with the alpha transition barrier energy E_α in Ref. [187]. It was found there that $E_\alpha = mk_BN_aT_g$, i.e. E_α is the product of the fragility index m, the Boltzmann constant k_B, the Avogadro constant N_a and the glass transition temperature T_g. The fragility index is only known for a limited number of alloys [175, 180], which includes six
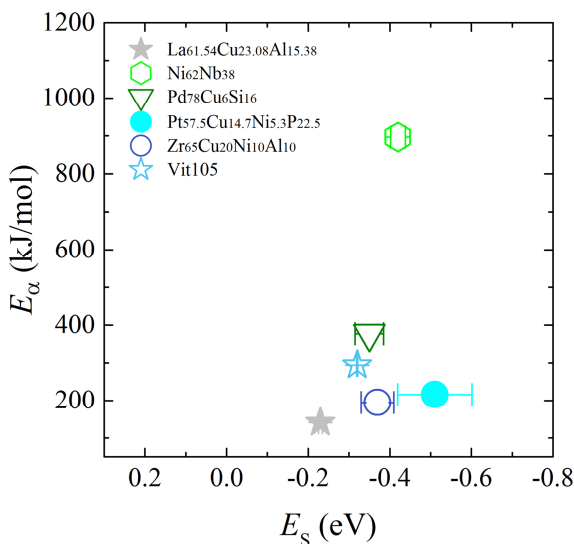
Figure 6-22: Alpha transition E_α vs. activation energy E_S.

compositions close to the alloys tested in this study. Although the numbers of alloys are limited, the available values make a strong correlation between E_α and E_S unlikely (Figure 6-22). This can again be understood by the structural dissimilarity of the processes involving shear-band propagation and equilibrium high-temperature flow

iii) With the Poisson's ratio v scaling with toughness, v describes how far shearing is preferred over cracking in both amorphous and crystalline alloys [46, 82, 83, 188]. In crystalline alloys, where toughness is linked to dislocation dynamics, the ratio of shear- to bulk-modulus, G/K, is a monotonically decreasing function of v. If v is small enough, spontaneous emission of dislocations from crack tips is possible, which causes the cracks to blunt and thus to toughen the material [83]. In MGs, a critical v has been
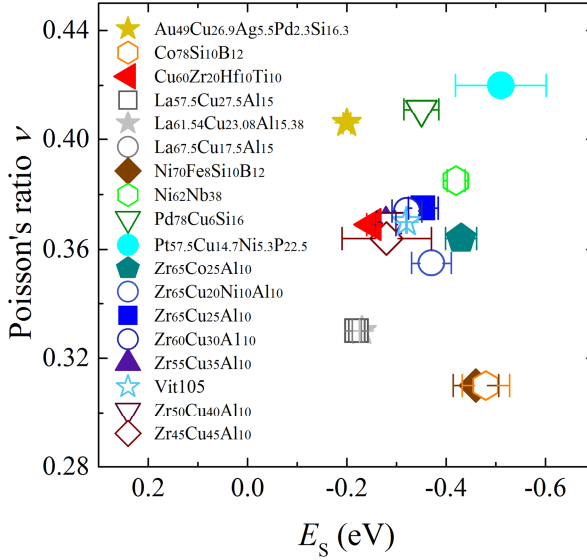
Figure 6-23: Poisson's ratio ν vs. activation energy E_S.

identified above which shear bands can form instead of cracks [82]. However, in the case of an already initiated, flowing shear band, the role of ν (or G/K) is less obvious, because both shear- and bulk-modulus within the activated, liquid-like shear band are clearly different from those of the bulk material. It is thus not surprising that there is no direct correlation between ν and E_S for the MGs tested (Figure 6-23).

Besides their inability to capture trends in shear dynamics, each of the above three parameters, T_g, E_α and ν, describes processes of flow initiation rather than flow itself. In other words, they are linked to the stability of the *glassy state*, whereas shear dynamics reflects the stability of the *(supercooled) liquid-like* state of the shear-band material. Because a shear band may be regarded as the result of STZ percolation, it is also important to evaluate a poten-

tial correlation between E_S and the typical energy scale for the rearrangement of such units; i.e. the STZ barrier energy..

iv) STZ barrier energy: This quantity is typically given for an ellipsoidal inclusion within a rigid matrix as $W_{STZ} = (8/\pi^2)G\gamma_C^2\zeta\Omega$ ([7, 55]), where G is the shear modulus of the glass, γ_C is the yield strain, ζ is a geometric constant, and Ω_{STZ} is the STZ volume, which is the volume of a group of 20-100 atoms. Table 6-7 lists the mean atomic radius $\bar{r}$, the STZ volume Ω_{STZ} calculated as $\Omega_{STZ} = 4\pi/3 \times (2.88 \times 2 \times r_{mean})^3$ and the resulting potential energy for STZ rearrangement W_{STZ}.

Table 6-7: Mean atomic radius $\bar{r}$, STZ volume Ω_{STZ} and potential energy for STZ rearrangement W_{STZ}.

| Alloy	$\bar{r}$ (pm)	Ω_{STZ} (nm)^3	W_{STZ} (eV)
$Au_{49}Cu_{26.9}Ag_{5.5}Pd_{2.3}Si_{16.3}$	133.1	1.89	0.55
$Co_{78}B_{12}Si_{10}$	119.1	1.35	1.12
$Cu_{60}Zr_{20}Hf_{10}Ti_{10}$	137.2	2.07	0.84
$La_{67.64}Cu_{17.5}Al_{15}$	169.9	3.89	0.58
$La_{61.54}Cu_{15.38}Al_{23.08}$	167.0	3.73	0.55
$La_{57.64}Cu_{27.5}Al_{15}$	163.3	3.49	0.52
$Ni_{70}Fe_8B_{12}Si_{10}$	119.8	1.37	1.16
$Ni_{62}Nb_{38}$	132.5	1.86	1.37
$Pd_{78}Si_{16}Cu_6$	135.3	1.98	0.72
$Pt_{57.5}Cu_{14.7}Ni_{5.3}P_{22.5}$	128.4	1.69	0.62
$Zr_{65}Co_{25}Al_{10}$	148.1	2.60	0.97
$Zr_{65}Cu_{15}Ni_{10}Al_{10}$	148.3	2.61	0.87
$Zr_{65}Cu_{25}Al_{10}$	148.3	2.61	0.82
$Zr_{60}Cu_{30}Al_{10}$	146.7	2.53	0.83
$Zr_{55}Cu_{35}Al_{10}$	145.1	2.44	0.86
$Zr_{52.5}Cu_{17.9}Ni_{14.6}Al_{10}Ti_5$	145.1	2.44	0.86
$Zr_{50}Cu_{40}Al_{10}$	143.5	2.36	0.83
$Zr_{45}Cu_{45}Al_{10}$	141.9	2.29	0.92
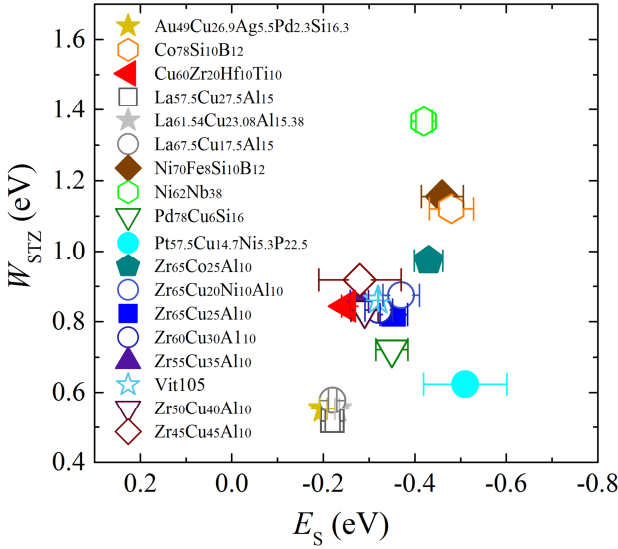
Figure 6-24: W_{STZ} vs. activation energy E_S.

In a plot of W_{STZ} over E_S (Figure 6-24), some clustering of data indeed becomes apparent and E_S tends to increase with increasing W_{STZ}. However, the inverse behaviour is observed among the Zr-based alloys and $Pt_{57.5}Cu_{14.7}Ni_{5.3}P_{22.5}$ represents a significant outlier to this trend. The relative weak correlation may be attributed to the fact that beyond yielding (i) the prerequisite of a rigid matrix is no longer met and (ii) the elastic constants of the flowing liquid-like material are fundamentally different from those of the glassy state.

iv) A very natural parameter describing the stability of a liquid independently of the elastic constants of the glassy solid is the liquidus temperature T_l. Indeed, Figure 6-25 reveals even more pronounced data clustering than that observed with W_{STZ}, and generally E_S tends to increase with increasing T_l; but again,
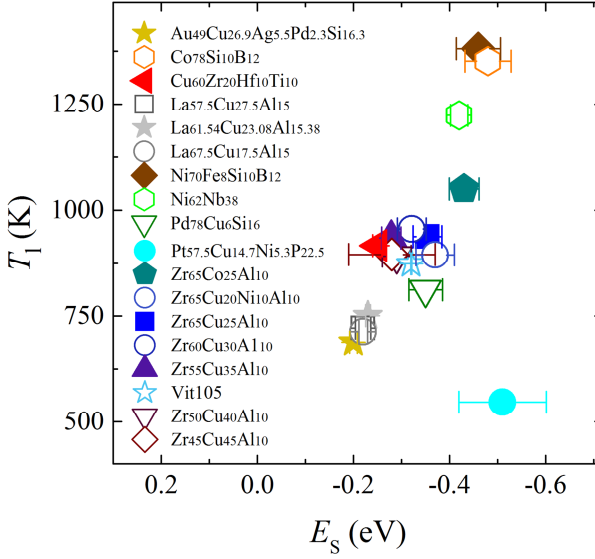
Figure 6-25: Liquidus temperature T_l vs. activation energy E_S.

$Pt_{57.5}Cu_{14.7}Ni_{5.3}P_{22.5}$ represents a significant outlier. The modest correlation indicates a connection between E_S and a cohesive energy on the part of the liquid-like shear-band material.

As such, the two most prominent fundamental parameters which have been brought forward to describe the mechanical stability of MGs (v and W_{STZ}) exhibit no trivial relation to the shear stability reflected by E_S (see Figure 6-23 and Figure 6-24), which is also the case for the quasi-static equilibrium parameters T_g and E_α (Figure 6-21 and Figure 6-22). The strongest, but still non-universal correlation is found between E_S and T_l (Figure 6-25), which, however, is a mean-field value that does not consider any of the properties of the local structure.

If the above parameters are inadequate for describing shear stability, the question arises as to which fundamental physical param-

eters remain which are relatively insensitive to the high local strain rate and the confinement effects in the nanoscale shear bands. If we accept the classical view that a local plastic transition (an alpha process or an STZ) involves atomistic jump processes [189] which may be facilitated by the presence of structural and topological heterogeneity in the flowing band, the most fundamental and straightforward parameter is any generalized energy barrier in the framework of thermally activated flow. Here the activation barrier of a stress-assisted structural transition can be expressed as $Q = H - \tau\Omega$, where H is the activation energy at zero load, τ is the shear stress, and Ω is the involved activation volume. A good estimate for H may be gained by considering how strongly the atoms in the shear band are bound to their immediate surroundings. In other words, the local atomistic dynamics in the activated shear-band material is expected to scale with the prevailing bond strengths of typical short-range ordered building blocks. A quantitative way to determine the topology of these building blocks for systems with more than three components is given in Ref.[190], which is an improved version of the ELAP model. Based on this model, namely by applying Equation 2-2 and Equation 2-4, typical dominant structural motifs can be assigned to each constituent in each of the alloys investigated here.

Table 6-8: Iterative calculation of partial coordination numbers in the alloy $Zr_{65}Cu_{25}Al_{10}$; $R = r_{solute}/r_{solvent}$.

Iteration	R	$N_{Cu, tot}$	$N_{Cu,Al}$	$N_{Cu,Cu}$	$N_{Cu, Zr}$
1	0.849629	10.59564	1.159564	1.898909	7.537164
2	0.83774	10.45577	1.145577	1.863942	7.446248
3	0.837583	10.45392	1.145392	1.86348	7.445049
4	0.837581	10.4539	1.14539	1.863474	7.445033
5	0.837581	**10.4539**	**1.14539**	**1.863474**	**7.445033**

An example calculation for the iterative determination of the coordination numbers around the element Cu in the alloy $Zr_{65}Cu_{25}Al_{10}$ is shown in Table 6-8. The atomic radii required by this method are listed in Table 6-9, together with values of heats of formation ΔH_f, which will be used in a later step. Table 6-10 provides the resulting species-specific total coordination numbers.

We acknowledge at this point that atomistic modelling suggests that the structure within a shear band is somewhat depleted in typical motifs [112, 113], but nevertheless basic topological properties, such as the fact that large atoms are coordinated by more neighbours than small ones, also remain in the flowing state. The effect of topology on the structure in a shear band is thus assumed to be representative of the short-range ordered structure at rest.

Table 6-9: Element radii and heats of formation ΔH_f were taken from Ref. [191] (r) and Ref. [173] (ΔH_f) unless otherwise indicated. For phosphorus, the covalent radius and the heat of formation of the most stable allotrope, black phosphorus, was used.

Element	r (pm)	ΔH_f (kJ/mol)	Element	r (pm)	ΔH_f (kJ/mol)
Ag	144	284.9	Nb	143	726
Al	141	330	Ni	126	430
Au	143	366	P	107[†]	341[*]
B	88	565	Pd	142	378
Co	125	425	Pt	139	565
Cu	126	337.4	Si	110	450
Fe	125	414	Ti	142	473
Hf	158	619	Zr	158	609
La	187	431			

[†] value for covalent atomic radius from Ref. [192].
[*] value for the stable allotrope, black phosphorus [193].

Table 6-10: Topology of various MGs. $\bar{r}$ is the mean atomic radius and $N_{\text{1-5,tot}}$ are the total coordination numbers around the constituents 1-5 in order of appearance in the alloy name.

Alloy	$\bar{r}$ (pm)	$N_{1,\,tot}$	$N_{2,\,tot}$	$N_{3,\,tot}$	$N_{4,\,tot}$	$N_{5,\,tot}$
$Au_{49}Cu_{26.9}Ag_{5.5}Pd_{2.3}Si_{16.3}$	133.1	14.5	12.55	14.6/14.1*	14.36	10.16
$Co_{78}B_{12}Si_{10}$	119.1	14.1	9.1	12.22		
$Cu_{60}Zr_{20}Hf_{10}Ti_{10}$	137.2	12.14	15.7	15.7	13.87	
$La_{67.5}Cu_{17.5}Al_{15}$	169.5	14.93	9.15	10.23		
$La_{61.54}Cu_{23.08}Al_{15.38}$	165.9	15.31	9.35	10.46		
$La_{57.5}Cu_{27.5}Al_{15}$	163.3	15.59	9.49	10.63		
$Ni_{70}Fe_8B_{12}Si_{10}$	119.8	14.13	14	9.04	12.14	
$Ni_{62}Nb_{38}$	132.5	12.62	14.56			
$Pd_{78}Si_{16}Cu_6$	135.3	14.09	9.99	12.33		
$Pt_{57.5}Cu_{14.7}Ni_{5.3}P_{22.5}$	129.2	14.5	12.97	12.97	9.89†	
$Zr_{65}Co_{25}Al_{10}$	148.1	14.37	10.39	12.63		
$Zr_{65}Cu_{15}Ni_{10}Al_{10}$	148.3	14.34	10.45	10.45	12.61	
$Zr_{65}Cu_{25}Al_{10}$	148.3	14.34	10.45	12.61		
$Zr_{60}Cu_{30}Al_{10}$	146.7	14.52	10.57	12.76		
$Zr_{55}Cu_{35}Al_{10}$	145.1	14.7	10.69	12.91		
$Zr_{52.5}Cu_{17.9}Ni_{14.6}Al_{10}Ti_5$ (Vit105)	145.1	14.7	10.69	10.69	12.91	13.05
$Zr_{50}Cu_{40}Al_{10}$	143.5	14.89	10.82	13.07		
$Zr_{45}Cu_{45}Al_{10}$	141.9	15.09	10.94	13.24		

* coordination numbers not accounting for/ accounting for chemical short-range order.

† coordination number assuming P–P self-avoidance.

Chemical short-range order (CSRO) has so far not been taken into account by our model, except where there are reports on selective atom pair avoidance as for $Pt_{57.5}Cu_{14.7}Ni_{5.3}P_{22.5}$ and $Au_{49}Cu_{26.9}Ag_{5.5}Pd_{2.3}Si_{16.3}$. In the former, P–P self-avoidance, as in Pd–Cu–Ni–P, may be expected [194]. For the Au-based alloy we note that, unlike most transition metals involving Pd, Cu, Co, Ni and Fe, neither Au nor Ag form stable intermetallic compounds with Si. Positive heats of mixing between Au and Si have indeed been reported for the solid state [195], contrasting with tabulated values [196]. This positive heat of mixing may well result in Au–Si and Ag–Si avoidance in the metallic glass structure, which would agree with reports on monolithic Si being one of the competing crystalline phases in glass formation of Si-containing Au-based alloys [197]. Consequently, the emergence of additional typical motifs within these glasses, i.e. the emergence of silicon-free Au- or Ag-centred clusters, becomes probable. The relative fraction of these motifs is difficult to assess, but the alloy offers the possibility to estimate how CSRO affects the topology, and consequently Q. For this reason, we calculated the topology of the Au-based alloy for two cases, i.e. in the absence of CSRO and in the simple case of complete Ag–Si avoidance (Table 6-10). These two cases will serve as upper and lower limits for our calculation of Q.

Having calculated typical structural motifs, the next step is to attribute typical bonding energies to each atomic species. How this is done is illustrated schematically in Figure 6-26. The centre atoms of two interpenetrating clusters form a bond. The cones emerging from the two atoms illustrate each atom's contribution to the shared bond. The size of the cone scales with the atomic volume as $1/N_{i,tot}$, which is illustrated by the black sphere and cone on the bottom of Figure 6-26.
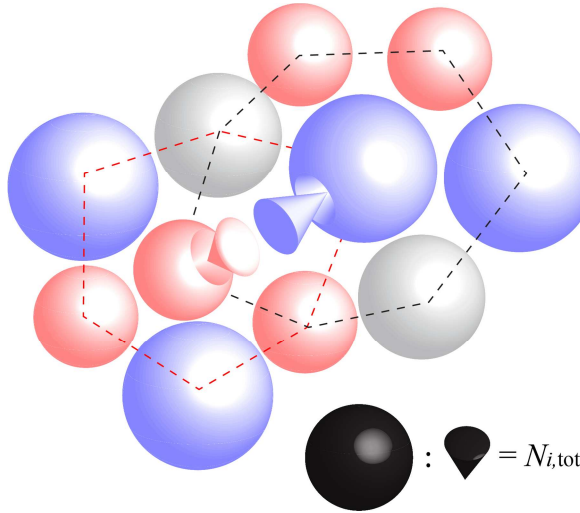
Figure 6-26: A bond between two nearest neighbours Cu (red) and Zr (blue) in a ternary alloy with Al (grey) is schematically depicted. The energy contribution of both atoms to the shared bond is weighted by the inverse of the species-specific total coordination numbers $N_{i,\text{tot}}$, illustrated by the emerging cones. The smaller atom Cu is coordinated by fewer atoms (6) than the larger atom Zr (7). Therefore, Cu contributes more to the energy of the next-neighbor bond than Zr. The size of the cone scales with the atomic volume like $1/N_{i,\text{tot}}$ (see illustration in black on the bottom right).

For the calculation of typical bonding energies, we approximate the bond energy between two atoms A and B by using the mixing enthalpy ΔH_{mix} of an ideal solution [198]: $\Delta H_{\text{mix}} = W X_{A} X_{B}$, where X_{A} and X_{B} are the relative mole fractions and $W = N_{a} z \left(\varepsilon_{AB} - \frac{1}{2}(\varepsilon_{AA} + \varepsilon_{BB}) \right)$, with N_{a} the Avogadro constant, z the number of bonds per atom, and ε_{AB}, ε_{AA}, and ε_{BB} the interaction energies between unlike atoms AB or like atoms AA or BB. In the simple case of a parabolic dependence of ΔH_{mix} on composition, we obtain $W = 4\Delta H_{\text{mix}}^{50-50} = N_{a} z \left(\varepsilon_{AB} - \frac{1}{2}(\varepsilon_{AA} + \varepsilon_{BB}) \right)$, which we can then solve for the interaction energy of an unlike bond: $\varepsilon_{AB} =$

$\frac{4\Delta H_{\mathrm{mix}}^{50-50}}{N_a z} + \frac{1}{2}(\varepsilon_{\mathrm{AA}} + \varepsilon_{\mathrm{BB}})$. Because metallic bonds are delocalized, we approximate the number of bonds per atom, z, by half the average of the total coordination numbers of the two atoms participating in that bond, i.e., $z = \frac{1}{2}\left(\frac{N_{\mathrm{A,tot}}}{2} + \frac{N_{\mathrm{B,tot}}}{2}\right)$. The division by two accounts for bonds being shared by atom pairs. With the strength of a bond between like atoms, e.g. A atoms, given as $\varepsilon_{\mathrm{AA}} = \Delta H_{\mathrm{f}}^{\mathrm{A}} / \left(N_a \frac{N_{\mathrm{A,tot}}}{2}\right)$ [199], i.e. as two times the heat of formation $\Delta H_{\mathrm{f}}^{\mathrm{A}}$ divided by the Avogadro constant times the total coordination number of species A, the bond energy of unlike bonds becomes

$$\varepsilon_{\mathrm{AB}} = \frac{1}{N_a}\left(\frac{\Delta H_{\mathrm{f}}^{\mathrm{A}}}{N_{\mathrm{A,tot}}} + \frac{\Delta H_{\mathrm{f}}^{\mathrm{B}}}{N_{\mathrm{B,tot}}} + \frac{8\Delta H_{\mathrm{mix}}^{50-50}}{\frac{1}{2}(N_{\mathrm{A,tot}} + N_{\mathrm{B,tot}})}\right).$$

Equation 6-4

In total, the bonding energy of an atom i to its immediate surroundings is the sum of the individual bond energies: $\varepsilon_i = \sum_{m=i,j,k,..} N_{i,m}\varepsilon_{im}$, where $N_{i,m}$ is the partial coordination number of type m atoms around the centre atom i. For the example given by the Cu-centred hexagonal cluster in Figure 6-26 (red dashed cluster), ε_i equals three times the energy of a Cu–Zr bond plus two times the energy of a Cu–Cu bond plus one time the energy of a Cu–Al bond. Expressed as a molar quantity, we obtain the species-specific bonding energy $H_i = \frac{N_a}{2}\varepsilon_i$. The division by two is again necessary to avoid double counting of bonds. By these means, we can quantify the bonding energy as a molar quantity H_i for each species in each of the alloys investigated. For the calculations, we used heats of mixing tabulated by Takeuchi and Inoue [196], and the heats of formation are compiled in Table 6-9. Following Spaepen [41], we approximate the activation volume Ω by the physical volume of the centre atom of the motif under investiga-

tion. It then becomes possible to attribute a species-specific barrier energy of $Q_i = H_i - \tau\Omega_i$ to every species i in the alloys, depending on topology, chemistry and shear stress $\tau \cong \sigma/2$. These species- and alloy-specific energies are presented in spectrum-type plots in Figure 6-27 and Figure 6-28.
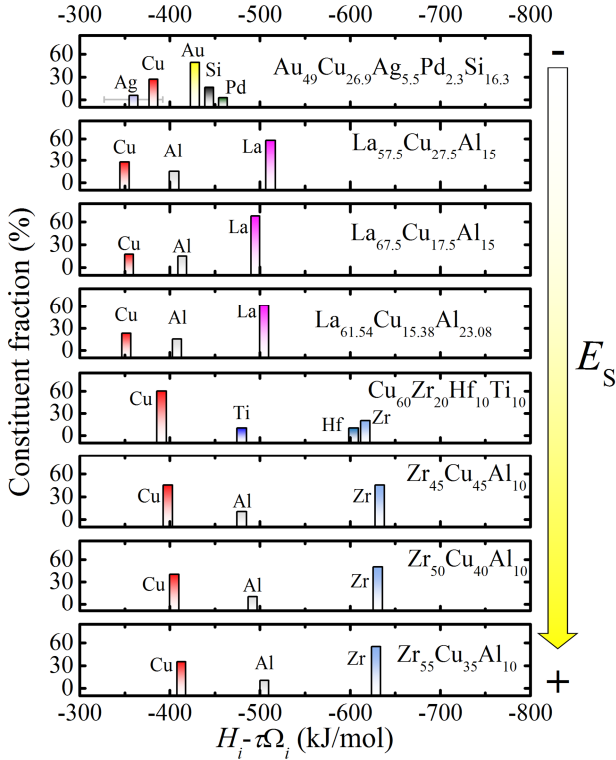

Figure 6-27: Constituent-specific energies Q_i for seven different MG alloys. The column height reflects the macroscopic compositions of each constituent.
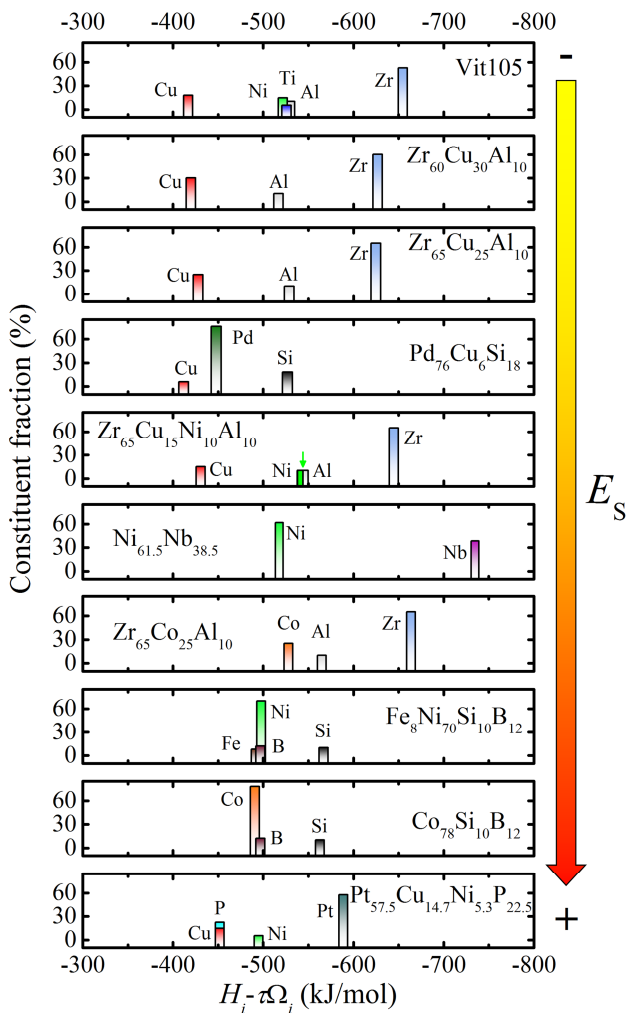
Figure 6-28: Spectrum-type plots of species-specific energies, continued. In $Zr_{65}Cu_{25}Ni_{10}Al_{10}$, fractions and energies of Al ($x = 10\%$, $Q = -545$ kJ/mol) and Ni ($x = 10\%$, $Q = -543$ kJ/mol) overlap almost fully, and are thus drawn beside each other for clarity.

Within one composition, bonding energies range from as small as ca. 100 kJ/mol for $Pd_{78}Cu_6Si_{16}$ to as great as 220 kJ/mol for $Zr_{65}Cu_{15}Ni_{10}Al_{10}$ (see Figure 6-27 and Figure 6-28). We observe here

that copper has particularly weak bonds with its neighbours in many alloys, whereas Zr, Pt and Nb tend to form strong bonds with their immediate surroundings. Comparing the E_S of different alloys, it appears that bonding energies are shifted to more negative values with increasing E_S (top to bottom).

The final step of the calculation is to define a mean species-specific energy to generate more quantitative results. To this end, we assign one single energy value to each alloy. This representative value can be obtained by describing the net effect of the different activation barriers as a superposition of the individual contributions, i.e.,

$$t_0 \exp\left(\frac{-Q_{\text{mean}}}{k_B T}\right) = \sum_{i=A,B,C...} x_i t_0 \exp\left(\frac{-Q_i}{k_B T}\right)$$

Equation 6-5

with atomic fractions x_i. The alloy-specific mean energy thus becomes

$$Q_{\text{mean}} = -k_B T \ln\left(\sum_{i=A,B,C...} x_i \exp\left(\frac{-Q_i}{k_B T}\right)\right)$$

Equation 6-6

In the following we use a temperature T of 300 K, but it is noted that the variation of Q_{mean} with temperature is smaller than 1% per 100 K. Figure 6-29 plots the calculated energies Q_{mean} versus the experimentally assessed activation energies for shear-band velocity, E_S. Here we arrive at the important result that a robust correlation can be found between the calculated characteristic bond energy Q_{mean} and the experimentally assessed barrier energy E_S. It is observed clearly that large activation energies E_S, i.e. slow shear-band dynamics, correspond to high energies Q_{mean}, i.e. strong

bonds and low stresses. The trend in Figure 6-29 is much more robust than those of E_S with T_l or W_{STZ} (Figure 6-24 and Figure 6-25). This is demonstrated in particular by the fact that Q_{mean} captures two main aspects of shear-band dynamics which could not be understood with the latter two parameters. Firstly, the results for the Zr-based glasses accord well with the behaviour generally observed for Q_{mean}, reflecting an increase in dynamics with a decrease in Zr content which was not observed for W_{STZ} and T_l. Secondly, $Pt_{57.5}Cu_{14.7}Ni_{5.3}P_{22.5}$ deviates much less from the general trend, where the remaining offset can be ascribed to the fact that the model developed here does not fully account for effects of non-metallic constituents such as phosphorus.
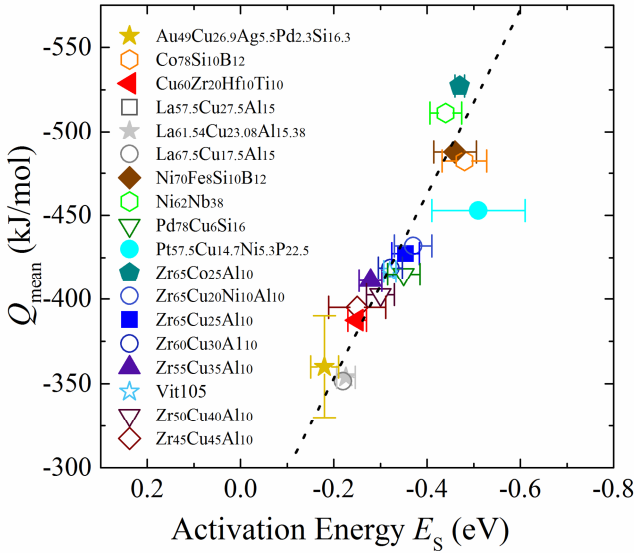

Figure 6-29: Correlation between the experimentally assessed activation energy E_s and the calculated characteristic bond energy Q_{mean}. The x-error bar represents the uncertainty of the Arrhenius-fitting of the activation energies. The large y-error bar for the Au-based alloy originates from uncertainties concerning chemical short-range order. The dashed line is a guide for the eye.

In this context, it is also interesting to note that the other two alloys which slightly deviate from a monotonous Q_{mean}-E_S scaling, $Co_{78}Si_{10}B_{12}$ and $Ni_{70}Fe_8Si_{10}B_{12}$, are, besides $Pt_{57.5}Cu_{14.7}Ni_{5.3}P_{22.5}$, the only ones within the data set that have atomic fractions of metalloids and/or non-metals exceeding 20 at.%. This points at large non-metals fractions being a possible promoter of increased shear-stability; a feature which is not captured in our present model.

This robust correlation between E_S and Q_{mean}, and thus this newly gained insight into shear stability of MGs, can now be implemented in design strategies for glassy alloys with improved mechanical properties. Given that fast shear-band dynamics contributes to MG embrittlement [77, 78], we propose that the new parameter Q_{mean} derived here, which represents shear-band stability, can be used to tailor MG plasticity. In combination with the well-known Poisson's ratio criterion [82], it now becomes possible to present a strategy for the design of new MGs which are both tough *and* have a high shear stability.

To this end, Figure 6-30 presents the relevant parameters ΔH_f [173] (which largely determines Q_{mean}), the Poisson's ratio ν [200] and the shear modulus G for any potential base element. This choice is based on the knowledge that the elastic constants of MGs are generally inherited from the base metal [47], and that a large ΔH_f of the base metal is a solid prerequisite for stable shear flow in MGs. It is thus expected that Figure 6-30 will allow us to identify the most suitable base element for a ductile MG; the best candidates are located in the first quadrant (green area) of Figure 6-30. The lower x-bound is set by the previously determined critical Poisson's ratio of 0.32 [81, 82] (a measure of stable shear-band initiation over crack formation), and the y-threshold is given by large bonding energies (identified as stable shear criterion),

which we define as resulting from $\Delta H_f \approx 370$ kJ/mol – a value located between Pd (378 kJ/mol), known for forming ductile glasses, [188] and Au (366 kJ/mol), known to form room-temperature brittle glasses [73]. While the range of shear moduli observed in the area of interest is relatively broad, i.e. from 30-150 GPa, the atomic radii lie predominantly in an intermediate size regime of 132-158 pm.

Figure 6-30 shows clearly that the well-known base metals for achieving ductile MGs (Pd [188], Pt [153], Zr [13], Ti [201], and Hf [202]) are all found in the relevant (green) quadrant. Additional promising candidates identified are Ta, Nb, Rh, and V.
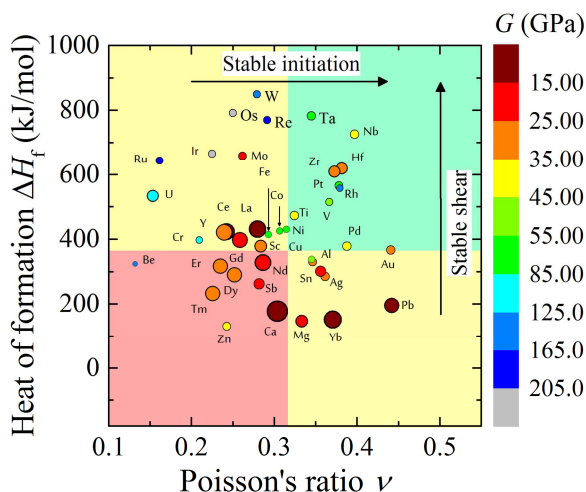

Figure 6-30: Heat of formation ΔH_f versus Poisson's ratio v for selected elemental metals. The shear modulus G is indicated by a colour code and the size of the symbols represents the atomic radii qualitatively. The elements most promising as base materials for MGs with pronounced plastic properties are located in the first quadrant, indicated by a green background colour. This quadrant combines a Poisson's ratio greater than 0.32 and a heat of formation greater than 370 kJ/mol.

Among these elements, Nb and Rh show the most promising combination of high Poisson's ratio and bonding energy. In fact, the formation of glassy ribbons with extraordinarily high bending ductility has been reported for binaries of these elements with silicon [203, 204]. Similarly, Mg- and Ca-based MGs, which are intensively studied glass-forming systems and known to be brittle [205, 206], are far outside the top-performing regime of a ΔH_f-ν combination, which is predominantly due to the weak bonding strength not causing stable shear.

In summary, we thoroughly investigated the activation energies for shear-band propagation of an extended set of MGs with different base elements. From an evaluation of the thermally-assisted flow we were able to capture the composition-dependent barrier height for shear banding in dependence on topology and chemical bond strengths. We find that Poisson's ratio, STZ barrier, T_g, T_l, and the alpha transition energy are not sufficient to explain the trends of the barrier energy E_S with chemistry. Indeed, we show that the activation barrier for a stress-assisted structural transition, $Q_i = H_i - \tau\Omega_i$, or the related characteristic bond energy Q_{mean}, respectively, correlate very well with the experimentally assessed barrier energy E_S. Based on this universal correlation we are able to identify various key properties which are responsible for stable shear flow in MGs. In particular, we illustrate that stable shear banding, i.e. slow shear-band dynamics, is observed in alloys which show a combination of (i) high heats of formation; (ii) large negative mixing enthalpies; and (iii) low shear stress or shear modulus. In addition, as known from literature, the Poisson's ratio must be greater than 0.32 for shearing to occur. This study thus identifies an important set of parameters which need to be tuned for the development of ductile bulk metallic glasses, and its results enable us to demonstrate that the most promising ductile MGs

would be based on the elements Pd, Pt, Zr, Ti, Hf, Ta, Nb, Rh, or V. The systematic development of an extended series of ductile bulk metallic glasses would be a breakthrough in this area of research.

Concluding remarks

Here, a potential alternative perspective should be presented, where a close relation of STZ barrier energy W_{STZ} and activation energy E_S can be found. In the context of the results and discussions outlined above, two questions may emerge that need to be addressed in more detail. First, does the model possibly contradict itself, when it attributes *weaker* bonds to alloys with *higher* yield stress, e.g. within the Zr–Cu–Al system? Second, can the model presented be in agreement with STZs as the dominant underlying mechanism for plastic deformation? The first question is addressed immediately, and, as will be seen, leads also to an answer for the second question.

In general, the true shear strength of a material corresponds to a fraction of its theoretical strength, which is proportional to the shear modulus G. Regarding interatomic bonding potentials (potential wells), the shear modulus is linearly related to the bonding energy H and the volume of an individual flow unit Ω, by $G \propto H/\Omega$. With $H \propto G\Omega$, H is in fact an integral part of Eshelby's equation for the rearrangement energy of an STZ (Equation 2-5). With W_{STZ} and Q_{mean} thus essentially describing a similar physical process, namely an internal energy opposing shear, the question arises why the latter matches E_S and the former does not. The reason must lie in the parameters G and Ω and whether they properly describe the local properties of an STZ. In literature, it is widely agreed that STZs consist of about 100 atoms. Shear moduli, on the other hand, are reported to depend strongly on the measurement technique: moduli assessed by *in-situ* X-ray diffraction tend to be

larger than those measured by the classical method that deploys ultrasonic elastic waves [207]. The reason for this difference is the fact that XRD probes the property of local atomic shells, while the ultrasonic method provides a mean-field averaged value [207]. For the determination of STZ properties, the properties of the atomic shells are naturally more important. The inability of W_{STZ} to explain trends in E_S may well originate from shear moduli of STZs which differ considerably from mean-field ultrasonic values typically tabulated in data sets on MG mechanical properties [46, 208]. Because of the lack of a large data set of XRD-derived shear moduli, the possibility of obtaining these properties via calculations is explored in the following. Cheng *et al.* [209] suggested that the mean-field value of elastic constants measured by the ultrasonic method is split into two contributions, one of "elemental" and one of "configurational" origin, i.e. $G = G_e + G_c$. The configurational contribution G_c is always negative, because glasses are less stiff than their crystalline counterparts, and is also closest to zero in a most efficiently packed glass. The difference between the mean-field modulus and the atomic-shell modulus might thus be mostly allocated to G_c, and we thus should focus on G_e, i.e. the elemental contribution, to assess the shear modulus of an individual STZ. In Ref. [209], G_e is calculated as the average of the results of two different rules-of-mixtures, which use the molar volumes V and the atomic fractions f as weighting factors, i.e.,

$$G_e = \sum_{i=1}^{n} \frac{G_i f_i V_i}{\bar{V}}, \quad G_e = \left(\sum_{i=1}^{n} \frac{f_i V_i}{G_i \bar{V}} \right)^{-1},$$

<div align="right">**Equation 6-7**</div>

where $\bar{V}$ is the average molar volume. With this type of weighting, it becomes obvious that G_e depends on topology: if small atoms

(with smaller V) contribute less to the total modulus than large atoms do, this is *per se* a form of topological weighting. These rules-of-mixtures might be improved by shifting the weighting factors from atomic volumes of pure substances towards actual total coordination numbers $N_{i,\text{tot}}$, which we have already calculated in Table 6-10. By doing so, meaning by exchanging V and $\bar{V}$ by N and $\bar{N}$ in Equation 6-7, we obtain a new shear modulus which we call G_{SRO}, where SRO stands for short-range order, because it comprises properties of efficient local atomic packing. From that perspective, the equation for the total shear modulus might be rewritten as $G = G_{\text{SRO}} + G_{\text{MRO}}$, allocating all mean-field effects (rigid interconnected backbone and softs spots) to the medium-range order (MRO). Using G_{SRO} rather than G in Equation 2-5, we are thus able to exclude MRO effects in the calculation of W_{STZ}.
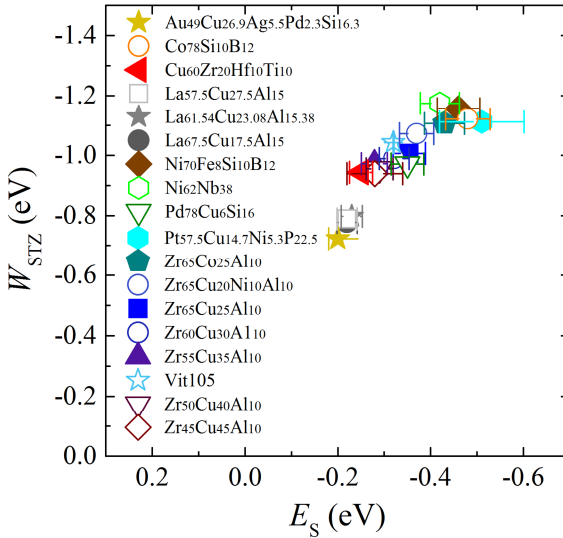

Figure 6-31: Short-range order STZ rearrangement energy W_{STZ} calculated from G_{SRO} as a function of the activation energy E_{S}.

Figure 6-31 shows the correlation between this new W_{STZ} and E_S. Indeed, a very good correlation between W_{STZ} and the activation energy E_S emerges, and even a good match between the energy scales is found with both parameters expressed in electron volts. Using $W_{STZ}(G_{SRO})$, Equation 2-5 now not only aims at the description of the same property as Q_{mean}, but in fact gives the same result: stable shear goes along with strong bonding in the short-range order structure. By finding this correlation, the questions that rose in the beginning of this section can now be answered. Firstly, the apparent contradiction of strong materials having weak bonds emerges from ultrasonically assessed moduli which represent a mean-field value rather than a property of the local STZ environment. Secondly, with the occurrence of a similar dependency of Q_{mean} (Figure 6-29) and W_{STZ} (Figure 6-31) with E_S, we can well conclude that our results fully comply with STZs as the important underlying dynamic mechanism.

6.4. Time-resolved measurements of shear-band heating during inhomogeneous flow[4]

This section aims to contribute experimental evidence to resolve the long-standing question of shear-step generation, and with that, shear-banding temperature (see section 3.4). We believe that improving direct temperature measurement during serrated flow is a promising approach to reaching this goal. A direct assessment of shear-band temperature during inhomogeneous flow has so far been impeded by the small size of the shear band and the short time scale of its operation, both of which lie significantly below the resolution limits of standard experiments such as IR thermography, normally used to resolve issues of local heating in materials science [210-212]. First IR studies of MG deformation [213-215] focused on fatigue and tension, reporting temperature jumps of 3 K in regions of shear-band activity. Whereas this observation allows the measurement of the total amount of released heat, the true shear-band temperature at the time of its operation could only be reconstructed using sophisticated calculations that are, as we have learned above, highly dependent on the choice of the deformation model (Figure 3-6). Wang et al.[213], e.g., assumed instantaneous heating (scenario 1 in Figure 3-6), which led to the estimation of a temperature rise within the shear band of about 1200 K, i.e. a temperature jump that would effectively cause melting of a layer around ten times thicker than the actual shear band.

In this study, we present the results of high-acquisition rate IR thermography on stable serrated flow in $Zr_{57.1}Co_{28.6}Al_{14.3}$ MG. With

---

[4] Corresponding publication:

(1) P. Thurnheer, F. Haag, J. F. Löffler, Time-resolved shear-band heating during inhomogeneous deformation of metallic glasses, Acta Mater. **115** (2016) 468-474.

this method we have been able to probe an experimental time scale which lies between the time scales postulated by models 1 (phonon time scale) and 4 (serration time scale) in Figure 3-6. Such improved resolution was obtained firstly by using cutting-edge IR technology, and secondly by choosing a Zr–Co–Al alloy, which has particularly slow shear-band dynamics [216].

Figure 6-32 illustrates the localized heating and subsequent cooling of a line-shaped region, extending from the notch at an angle of ≈45°, that appeared in the IR thermographs during stable serrated flow. The frame number for each snapshot (framerate 2500 fps = 0.4 ms per frame) is indicated. An improvement of contrast was achieved by subtracting a background image, which was obtained by an average of the last ten images prior to the onset of heating. Two different sequences of events are observed in Figure 6-32. For most of the serrations (ca. 70%, Figure 6-32a), the line-shaped heat source appears within a single frame (f = 1-2). Within the course of the next milliseconds, the band widens and the temperature in the centre increases (f = 3-10, heating rate 260 K/s). Thereafter, the temperature peaks (f =14, $\Delta T \approx 2$ K) and the apparent band starts to cool down slowly, as heat is conducted away towards the anvils. For other serrations (Figure 6-32b), the line shape is established via an apparent propagating front over up to 4 subsequent frames (f =1-4). The temperature difference across the front amounts to about 0.15 K, and the heating rate on the established part of the apparent band is about 50 K/s. When it reaches the other side of the sample, the temperature of the apparent band simultaneously increases further along the band (f = 5-10, heating rate 230 K/s), until it reaches a peak temperature of $\Delta T \approx 2$ K (f =14) at a delay of about 10 frames (= 4 ms). Afterwards cooling occurs analogous to the event shown in Figure 6-32a. Almost all heat created by an event is conducted away prior to the onset of a sub-
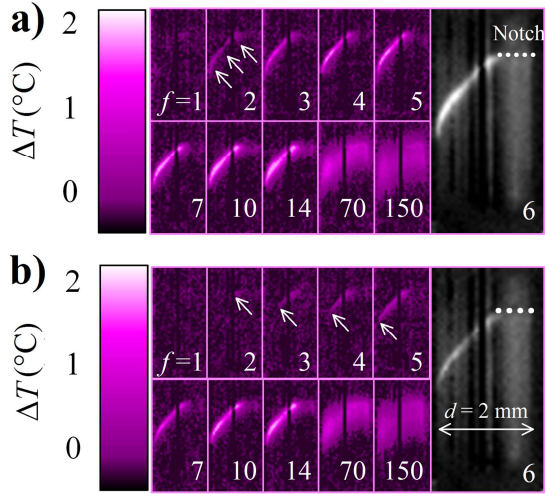
Figure 6-32: Localized heating during serrated flow. a) Instantaneous appearance of the shear band, and b) propagating heat front. f indicates the frame number, whereby 1 frame is measured within 0.4 ms.

sequent event. In other words, the sample temperature prior to a subsequent heating event is constant. The observed temperature rises involves some degrees Celsius, agreeing well with literature [217].

The sample-spanning line of pixels at which heating was initially observed is assumed to contain the major shear band. By averaging over these pixels, i.e. the apparent shear band, we can quantify the evolution of the apparent shear-band temperature over time. Figure 6-33a shows the temporally synchronized signals of stress (black) and apparent shear-band temperature (magenta). The plot is divided into three parts. The first part shows that the first major temperature increase correlates with the first major serration, i.e. with the reaching of peak stress. The few minor events that can be identified before reaching peak stress are attributed to diffuse,
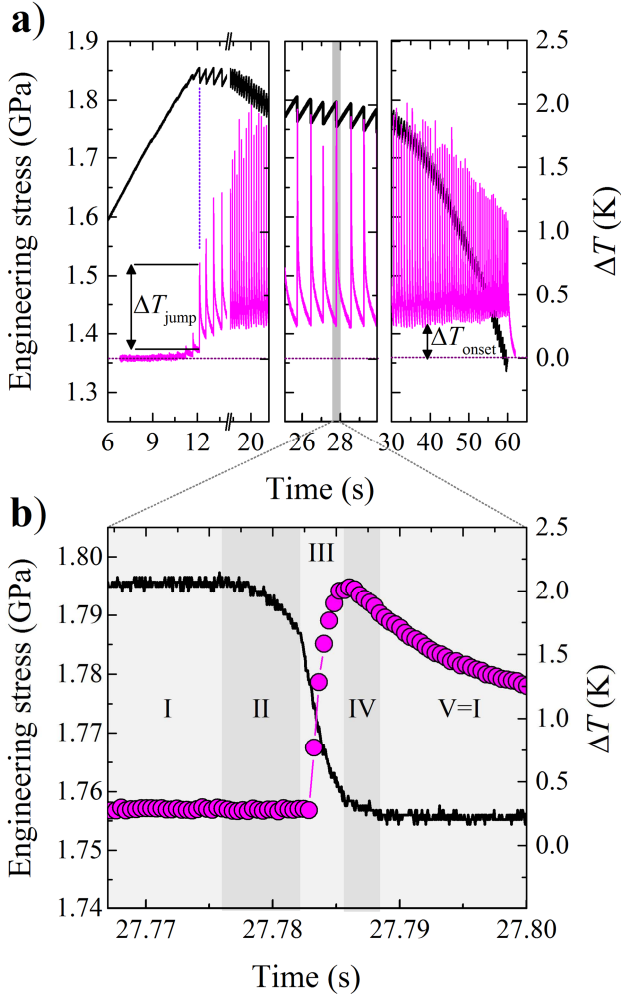
Figure 6-33: Serrated flow curve and temperature of the apparent shear band as a function of time. a) Throughout the experiment, each temperature jump corresponds to a single serration. **b)** Close-up of an individual serration. In the stress signal, the different stages (I) slow loading, (II) transition to unloading, (III) fast unloading, (IV) arrest and (V) reloading (= I) are identified. A significant temperature rise is only observed in stage III.

non-system spanning events which, we believe, are due to a slight inhomogeneity of the stress state. Apart from the temperature jumps ΔT_{jump}, a temperature increase during the first serration events causes a background temperature rise $\Delta T_{onset} \approx 0.2°C$, which also remains at larger strains. The middle part of Figure 6-33a demonstrates clearly that each serration coincides with one temperature jump. The third part finally gives the remaining flow curve for the sake of completion. The temperature jumps are largest in the intermediate time regime, which is equal to an intermediate strain regime of about 5-15% because of the constant strain rate.

Figure 6-33b resolves the correlation of a single flow serration with the apparent shear-band temperature during an "instantaneously appearing" event (Figure 6-32a). Five stages can be distinguished during the course of a flow serration. Stage (I) represents the end of the elastic loading, i.e. the "stick" part of the serration cycle. In a second stage, (II), stress starts to drop at a moderate rate without inducing a resolvable temperature increase (it is noted that the apparent heat front appearing in the other type of serrations (Figure 6-33b) occurs here, causing a minor temperature increase of below 0.2°C). In stage (III), the stress drop rate increases suddenly and coincides with the onset of the temperature jump, which is resolved within at least 8 frames. Reaching the bottom stress level (IV), the drop rate is reduced and transits towards the slow reloading phase (V). On average, temperature jumps ΔT_{jump} are on the order of 1.1°C and maximum temperature jumps are about 1.9°C. The onset temperature difference, i.e. the temperature difference at the coordinates of the apparent band prior to a serration event, is about 0.2°C, which is around 10% of the peak value.

Discussion

Shear-band heating is observed as starting either simultaneously on the apparent shear plane or, with less probability, to form over a propagating front. It is found that front propagation, which causes only a small temperature increase, coincides with stage II in the stress serration, i.e. with a transient state between the slow stick stage (I) and fast slip phase (III). In serrations of the "instantaneous" type, no temperature rise is monitored in stage II. For both types of serrations, significant heating starts only upon entering stage (III), i.e. the stage at which the AE shear-band initiation signal is also located [132]. We may thus differentiate between some diffuse pre-initiation phase (II), and the pronounced, fast shearing phase (III). In the following, we focus on the latter.

The fact that the temperature of the apparent major shear band peaks only towards the end of a serration strongly supports the idea that the time scale for temperature rises equals that of the serrations. However, there remains the issue of limited spatial resolution, because we do not directly measure the temperature of the shear band, but the temperature of an apparent band whose thickness is equal to the resolution of the IR thermographs. Naturally, it takes some time for the heat to diffuse from the true shear plane over the distance of the method's resolution, which is $w = 80$ μm for our setup. Thus only a comparison between the measured data and the predictions of the various models will allow us to make a strong statement regarding the time scales involved in heating and thus about the mode of shear-step formation and shear-band temperature. With model (2) having been discarded (see introductory part) and model (3) having been identified as the result of geometrically-induced artefacts, we restrict ourselves to comparing the experimental results with the predictions of models (1) and (4), i.e.

the phonon-shear-front propagation model (1) and the serration-simultaneous shearing model (4); see Figure 3-6. In both scenarios, the true shear band is approximated by an infinitely large plane with zero thickness.

According to Ref. [119], the time- and coordinate-dependent temperature jump caused by a constant heat source over an event duration Δt is given by

$$\Delta T_{\text{const}}(x, t, q_s) = \frac{q_s}{2c_p\alpha}\left(\sqrt{\frac{4\alpha t}{\pi}}\exp\left(\frac{-x^2}{4\alpha t}\right) - x\,\text{erfc}\left(\frac{x}{\sqrt{4\alpha t}}\right)\right),$$

<div align="right">**Equation 6-8**</div>

where ΔT is the temperature jump, $c_p \approx 3 \times 10^6$ J m^{-3} K^{-1} is the specific volume heat capacity, $\alpha \approx 2 \times 10^{-6}$ m^{2}s^{-1} is the thermal diffusivity, t is the time, x is the distance from the heat source and q_s is the heating rate, which is given as $q_s = H/\Delta t$, i.e. the amount of released heat H per area divided by Δt. The released heat is [78, 218].

$$H = 0.5\sigma_y\Delta u_{\text{pl}},$$

<div align="right">**Equation 6-9**</div>

where σ_y is the yield strength.

In the case of model (1), the time scale of observation (milliseconds) is much greater than the time scale of assumed event duration (nano- to microseconds). Therefore, the time-dependent temperature jumps at the time scale of observation can be approximated well by instantaneous heating, as in Ref. [78]:

$$\Delta T_{\text{inst}}(x, t) = \left(\frac{H}{2c_{\text{p}}\sqrt{\pi\alpha}}\right)\frac{1}{\sqrt{t}}\exp\left(\frac{-x^2}{4\alpha t}\right).$$

<div align="right">**Equation 6-10**</div>

For model (4), with an input time scale on the same order of magnitude as the time scale of observation Δt, Equation 6-10 is used as a direct starting point which we will refer to as model (4a). This model has two limitations, however, which we account for in the following to obtain an improved model (4b). First, Equation 6-8 is only valid as long as the heating source is active. It can therefore not be used to model temperature evolution for periods longer than Δt. This limitation can be overcome by calculating the temperature evolution once the heating source is switched off, which gives

$$\Delta T_{\text{off}}(x, t_{\text{off}}, H_i) = \int_{\xi=0}^{d} \Delta T_{\text{inst}}(x - \xi, t_{\text{off}}, H_i(x - \xi, \Delta t, q_s))d\xi,$$

<div align="right">**Equation 6-11**</div>

where ξ is a space variable, d is the distance at which the temperature rise becomes insignificant (in our case $d = 500$ μm), t_{off} is the time elapsed since the source was switched off, and $H_i(x, t_0, q_s) = \int_{\xi}^{\xi+\Delta\xi} \Delta T_{\text{const}}(x, \Delta t, q_s)c_{\text{p}}d\xi$, i.e. the heat content just prior to switch-off, discretized in spaces $\Delta\xi$. In other words, the thermal profile just before switch-off is converted into a discrete heat profile, and the components are then treated as instantaneous heat sources according to Equation 6-10, which, added together, will provide the total temperature at a given coordinate and time. The second limitation of Equation 6-8 is that constant heating rate has the tendency to oversimplify the problem, as acknowledged in Ref. [119]. Having recorded stress drops with high acquisition rates,

we are, however, also able to overcome this limitation and to directly calculate a time-dependent heating rate from the derivative of the stress signal during a serration. This is achieved by combining Equation 3-2 and Equation 6-9, which gives

$$q_s(t) = \frac{1}{2}\sigma(t)\frac{d\sigma}{dt}A(C_M + C_S),$$

where A is the sample cross-section, and the yield stress σ_y in Equation 6-9 has been substituted by the time-dependent stress during a serration, $\sigma(t)$. Equation 6-12 allows us to predict a temperature evolution proportional to the decrease in potential energy of the machine-sample assembly. The time- and space-dependent temperature jump for model (4b), which we call "proportional heating", thus becomes

$$\Delta T_{\text{prop}}(x, t) = \int_{\tau=0}^{t} \Delta T_{\text{off}}\Big(x, \tau - \Delta\tau, H\big(x, \Delta\tau, q_s(\tau)\big)\Big)\, d\tau,$$

where $\Delta\tau$ is the discrete time step of the numerical integration. Equation 6-13 thus represents the sum of all contributions to the total temperature jump caused by the heat sources q_s that were active for durations $\Delta\tau$ at times $\tau \leq t$, each of which can be calculated with Equation 6-11, i.e. with the above-mentioned switched-off source method.

We will now test these two scenarios, instantaneous versus proportional heating, on the serration displayed in Figure 6-34a. The time-dependent heating rate per area – a heat flux density, to be precise – is shown in Figure 6-34b.
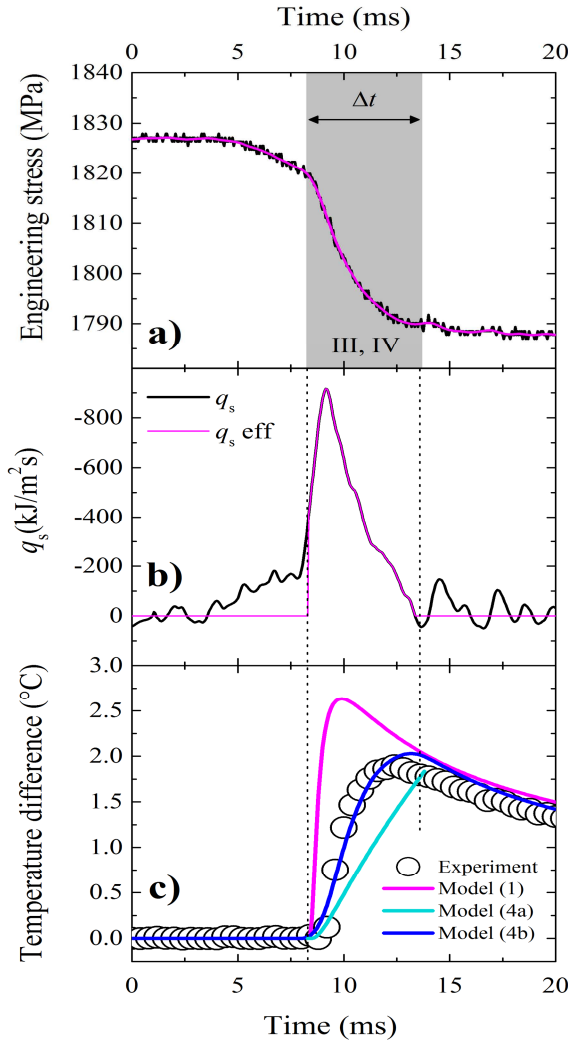
Figure 6-34: a) Raw and smoothened stress-drop data; b) raw and effective heat flux density as a function of time; c) comparison of the experimental temperature trace (circles) with the predictions of model (1) (phonon shear-front propagation, magenta), model (4a) (serration-simultaneous shear with a constant heating race, cyan), and model (4b) (serration-simultaneous shear with a heating rate proportional to the elastic-energy release, blue).

For the calculations we used an effective heating rate which is set to zero except for serration stages III and IV. The time at which stage III starts is also used as a time reference for the positioning of the curve obtained for models (1) and (4a).

Figure 6-34c shows how the experimentally determined shear-band temperature compares with the various model predictions evaluated at $x = 80$ µm. Shear-step generation according to model (1) (magenta) generates a rapid temperature increase upon shear-band initiation when entering stage III. Here, the maximum of the temperature jump (2.6°C) is reached within 1.6 ms. Thus model (1) not only overestimates the temperature jump but also the time-dependent heating rate. Converse behaviour is observed for shear-band heating at a constant rate (model (4a), cyan), where the heating rate is underestimated at the beginning of the serration and slightly overestimated towards the end of the event. Thus, while model (4a) provides realistic values for the temperature jump it fails to match the time-dependent heating of the apparent band. Clearly, model (4b), which describes heating as proportional to the elastic-energy release, matches the experimental data best. Both the time-dependent heating rate (slope) and the peak temperature are reproduced very accurately by the simulation. This is observed throughout the set of 80 serrations. Having now accounted for thermal diffusion from the shear plane to the apparent band, which has the thickness of one pixel, we can therefore conclude that the temperature trace observed cannot be caused by the process described by model (1). Instead, Figure 6-34c provides strong evidence that the shear step is mostly caused by simultaneous shear (Figure 3-6, model 4), which occurs at the time scales obtained by high-acquisition rate instrumented mechanical testing.

Figure 6-35 now addresses the emerging question of true shear-

band temperature. To this end, Figure 6-35a shows the histograms of the experimentally recorded temperature jumps. The apparent band temperatures simulated by models (1) and (4b) are shown by the open columns in Figure 6-35b and c, whereas the solid columns in these figures refer to the temperatures obtained when the models are evaluated at $x = 0$, i.e. right at the position of the shear plane. In the current calculation, Equation 6-8 with $t = \Delta t = 10^{-8}$ s
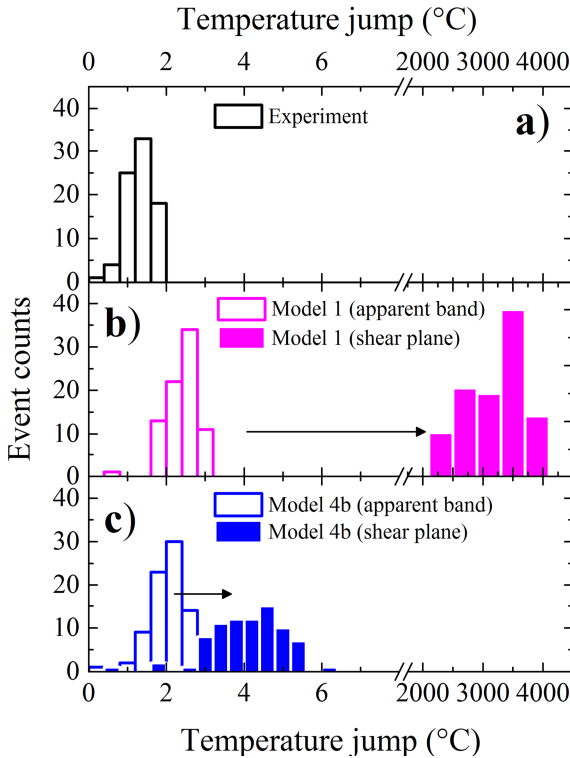

Figure 6-35: Histograms of shear-band temperatures. (a) Experimentally measured temperature jumps of the apparent shear band (which has the size of a pixel); (b) temperature jumps simulated by model (1) for the apparent band (open columns) and for the shear plane (solid columns); and (c) temperature jumps simulated by model (4b) for the apparent band (open columns) and for the shear plane (solid columns).

was used for model (1). While model (1) predicts shear-band temperature rises of 2000 to 4000°C, model (4b) predicts only moderate rises of 2-6°C for the actual shear plane. Because model (4b) was found to agree best with the experimental data in terms of the heating time of the apparent band (Figure 6-34c), we can clearly conclude that temperature rises during shear banding are very moderate. These results may conclude the long-standing debate about the dynamics of shear banding and the resulting temperature increase.

In summary, we have reviewed the current models of shear-step generation during inhomogeneous deformation and carried out time-resolved shear-band heating experiments on Zr–Co–Al MGs during compressive stable, serrated flow. We measured maximum temperature jumps of 1-2°C for an apparent band of 80 μm thickness and were able to show clearly that each temperature rise coincides with the end of the slip phase in a flow serration. Accounting for thermal diffusion and comparing the experimental results with two of the reviewed deformation models, namely shear-band heating at time scales of elastic wave propagation (model (1): phonon-shear-front propagation) and shear-band heating at time scales of flow serrations (model (4): serration-simultaneous shear), we find strong evidence for the validity of model (4). Using this model, our results then provide evidence that shear-band heating in metallic glasses is less than 2-6°C during stable serrated flow. More pronounced shear-band temperature jumps may be expected for larger samples with higher stress levels and increased shear-band dynamics, as may be concluded from an evaluation of Equation 6-12. In general, however, model (4) adequately describes shear-band dynamics in metallic glasses, and temperature rises during shear banding are very moderate. Our findings may conclude a long-standing debate in this area of research.

7. Summary and outlook

"Somewhere, something incredible is waiting to be known"

Carl Sagan

In the first part of this project, we learned, firstly, that Arrhenius behaviour of the shear-band velocity is a general feature of MGs, and not a peculiarity of the Zr-based glass Vit105; secondly, that the activation energy emerging from that behaviour shows a characteristic dependence on alloy composition, which differs clearly among different systems, but is also resolvable within single MG systems; and thirdly, that this activation energy is reflected well in the bonding energy of atoms, which comprise alloy and constituent-specific topological configurations within the glass structure.

In the second part, first results on time-resolved shear-band heating during individual flow discontinuities in a stable deforming MG were obtained. These agree well with the common perception that shear is accumulated in a simultaneous mode throughout the duration of a discontinuity as assessed from the load signal, therefore providing experimental support for the fact that stable shear banding typically reaches maximum temperature rises of only 5°C.

Knowing that the duration of a discontinuity in fact represents the shear-band velocity, the results of the two parts of this thesis condense naturally into the formulation of a future research direction. Is the composition-dependent shear-band velocity reflected in composition-dependent shear-band heating during flow? What

would be the consequences of that effect for models on dynamic embrittlement, which up to now have only considered influences of stiffness, elastic constants and sample sizes?

In the context of materials design, the results of this thesis also motivate further research into the direction of Nb- and Rh-based MGs, both of which are promising base materials for plastic glasses due to their advantageous combination of high Poisson's ratio and large self-bonding energy.

8. Appendix

8.1. List of facilitators

Daub, Eric Assistant Professor at the University of Memphis. Patiently answered all my questions concerning STZ theory.

Fischer, Erwin Technician at LMPT. Helped with alloying and casting.

Granata, Davide A former doctoral student at LMPT. Introduced me to the Zr–Cu–Al MG system which stands at the beginning of this work.

Haag, Fabian A doctoral student at LMPT. Convinced me of the prospect of *in-situ* experiments on shear-band temperature and has participated in the experiments.

Hahn, Kathy Proof-reader at ETH. Improved the English of the dissertation.

Hecht, Joe Technician at LMPT. Programmed a LabView routine for synchronous measurement of load and temperature during compression tests.

Joseph, David A former student at the University of Cambridge. Performed experiments on the processing of Au-based MGs.

Klaumünzer, David A former doctoral student at LMPT. Introduced me to the topic of shear banding in MGs and patiently answered all of my questions.

Laws, Kevin	Senior Lecturer at the University of New South Wales. Introduced me to the concept of efficient-local atomic packing and contributed largely to the understanding of alloy-specific shear banding. Also provided wedges of the alloy $La_{61.54}Cu_{23.08}Al_{15.38}$.
Löffler, Jörg F.	Professor at ETH Zurich and head of the LMPT. Supervisor of this thesis.
Maaß, Robert	Assistant professor at the University of Illinois at Urbana-Champaign. Mentor.
Pogatscher, Stefan	A former postdoc at LMPT. Participated in fruitful discussions.
Schindler, Fluregna	A former SJF student. Worked on the processing of Cu-based MGs.
Springbett, Helen	A former student at the University of Cambridge. Performed experiments on Zr-based MGs.
Wegmann, Bea	A technician at LMPT. Helped preparing the starting-materials.
Wegmann, Christian	A technician at the LMPT. Helped setting up and maintaining the experimental infrastructure.
Zhang, Jesse	A former SJF student. Worked on the processing of Zr-based MGs.

8.2. Curriculum Vitae

Peter Thurnheer
Born 2nd November 1985
Citizen of Weinfelden TG, Switzerland

peter.thurnheer@gmx.ch

Oral presentations

P. Thurnheer, D. Klaumünzer, R. Maaβ, J. F. Löffler, Size-dependent embrittlement in Zr-based bulk metallic glasses and its dependence on shear-band velocities, DPG Spring Meeting 2012, Berlin, March 26-29, 2012.

P. Thurnheer, D. Klaumünzer, J. F. Löffler, The effect of system compliance on shear-band dynamics in a Zr-based bulk metallic glass, ISMANAM 2012, Moscow, June 17-21, 2012.

P. Thurnheer, R. Maaβ, S. Pogatscher, A. Saeed-Akbari, J. F. Löffler, Kinetics of single shear bands in Zr-based bulk metallic glasses, DPG Spring Meeting 2014, Dresden, March 30 – April 4, 2014.

Poster presentation

P. Thurnheer, J. F. Löffler, Deformation kinetics in CuZrHfTi metallic glass, Barkhausen Symposium 2013, Göttingen, May 22-24, 2013.

9. References

[1]   W.L. Johnson, Bulk metallic glasses - A new engineering material, Current Opinion in Solid State & Materials Science **1** (1996) 383-386.

[2]   A. Inoue, Stabilization of metallic supercooled liquid and bulk amorphous alloys, Acta Mater. **48** (2000) 279-306.

[3]   J.F. Löffler, Bulk metallic glasses, Intermetallics **11** (2003) 529-540.

[4]   M. Telford, The case for bulk metallic glass, Mater. Today **7** (2004) 36-43.

[5]   L. Tian, Y.Q. Cheng, Z.W. Shan, J. Li, C.C. Wang, *et al.*, Approaching the ideal elastic limit of metallic glasses, Nat. Comm. **3** (2012) 609.

[6]   C.C. Dun, H.S. Liu, L. Hou, L. Xue, L.T. Dou, *et al.*, Ductile Co-Nb-B bulk metallic glass with ultrahigh strength, J. Non-Cryst. Solids **386** (2014) 121-123.

[7]   W.L. Johnson and K. Samwer, A Universal Criterion for Plastic Yielding of Metallic Glasses with a $(T/T_g)^{2/3}$ Temperature Dependence, Phys. Rev. Lett. **95** (2005) 195501.

[8]   M.F. Ashby and A.L. Greer, Metallic glasses as structural materials, Scr. Mater. **54** (2006) 321-326.

[9]   W.L. Johnson, D.S. Lee, M.D. Demetriou, J.H. Na and G. Garrett, Golf club fabricated from bulk metallic glasses with high toughness and high stiffness, **US 20140213384 A1** (2014).

[10]   C.D. Prest, M.S. Scott, S.P. Zadesky, R.W. Heley, D.J. Stratton, *et al.*, Fastener made of bulk amorphous alloy, **US 20130333165 A1** (2013).

[11]   C.A. Pampillo and H.S. Chen, Comprehensive plastic deformation of a bulk metallic glass, Mater. Sci. Eng. **13** (1974) 181-188.

[12]   H.S. Chen, H.J. Leamy and M.J. O'Brien, Bending deformation in metallic glasses, Scr. Met. Mater. **7** (1973) 415-419.

[13] J. Xu and E. Ma, Damage-tolerant Zr–Cu–Al-based bulk metallic glasses with record-breaking fracture toughness, J. Mater. Res. **29** (2014) 1489-1499.

[14] P. Duwez, R.H. Willens and W.J. Klement, Continuous Series of Metastable Solid Solutions in Silver-Copper Alloys, J. Appl. Phys. **31** (1960).

[15] W.J. Klement, R.H. Willens and P. Duwez, Non-crystalline Structure in Solidified Gold–Silicon Alloys, Nature **187** (1960).

[16] H. Lyle, Pol Duwez - How It Was, Engineering and Science **46** (1983) 25-29.

[17] P. Duwez, Metastable phases obtained by rapid quenching from the liquid state, Prog. Solid State Ch. **3** (1967) 377-406.

[18] H.S. Chen and D. Turnbull, Thermal Evidence of a Glass Transition in Gold–Silicon–Germanium Alloy, Appl. Phys. Lett. **10** (1967) 284-286.

[19] H.S. Chen and D. Turnbull, Evidence of a Glass-Liquid Transition in a Gold-Germanium-Silicon Alloy, J. Chem. Phys. **48** (1968) 2560.

[20] H. Luo and P. Duwez, Metastable Amorphous Phases in Tellurium–Base Alloys, Appl. Phys. Lett. **2** (1963) 21.

[21] P. Duwez and S. Lin, Amorphous Ferromagnetic Phase in Iron–Carbon–Phosphorus Alloys, J. Appl. Phys. **38** (1967) 4096.

[22] P. Duwez, R. Willens and R. Crewdson, Amorphous Phase in Palladium-Silicon Alloys, J. Appl. Phys. **36** (1965) 2267.

[23] A. Inoue, T. Zhang and T. Masumoto, Al-La-Ni Amorphous Alloys with a Wide Supercooled Liquid Region, Mater. Trans. **30** (1989) 965-997.

[24] T. Zhang, A. Inoue and T. Masumoto, Amorhpous Zr-Al-TM (TM=Co, Ni, Cu) Alloys with Significant Supercooled Liquid Region of Over 100 K, Mater. Trans. **32** (1991) 1005-1010.

[25] A. Peker and W.L. Johnson, A highly processable metallic glass: $Zr_{41.2}Ti_{13.8}Cu_{12.5}Ni_{10.0}Be_{22.5}$, Appl. Phys. Lett. **63** (1993) 2342-2344.

[26] A. Inoue, N. Nishiyama and H. Kimura, Preparation and Thermal Stability of Bulk Amorphous $Pd_{40}Cu_{30}Ni_{10}P_{20}$ Alloy Cylinder of 72 mm in Diameter, Mater. Trans. **38** (1997) 179-183.

[27] D.B. Miracle, W.S. Sanders and O.N. Senkov, The influence of efficient atomic packing on the constitution of metallic glasses, Philos. Mag. **83** (2003) 2409-2428.

[28] D.B. Miracle, K.J. Laws, O.N. Senkov and G.B. Wilks, Partial Coordination Numbers in Binary Metallic Glasses, Metall. Mater. Trans. A **43** (2012) 2649-2661.

[29] D.B. Miracle, The efficient cluster packing model – An atomic structural model for metallic glasses, Acta Mater. **54** (2006) 4317-4336.

[30] H.W. Sheng, W.K. Luo, F.M. Alamgir, J.M. Bai and E. Ma, Atomic packing and short-to-medium-range order in metallic glasses, Nature **439** (2006) 419-425.

[31] D. Ma, A.D. Stoica and X.L. Wang, Power-law scaling and fractal nature of medium-range order in metallic glasses, Nat. Mater. **8** (2009) 30-34.

[32] Y.Q. Cheng and E. Ma, Atomic-level structure and structure–property relationship in metallic glasses, Prog. Mater. Sci. **56** (2011) 379-473.

[33] J. Ding, Y.-Q. Cheng and E. Ma, Full icosahedra dominate local order in $Cu_{64}Zr_{34}$ metallic glass and supercooled liquid, Acta Mater. **69** (2014) 343-354.

[34] J. Ding, Y.Q. Cheng and E. Ma, Quantitative measure of local solidity/liquidity in metallic glasses, Acta Mater. **61** (2013) 4474-4480.

[35] Z.Y. Liu and Y. Yang, A mean-field model for anelastic deformation in metallic-glasses, Intermetallics **26** (2012) 86-90.

[36] Z.Y. Liu, Y. Yang and C.T. Liu, Yielding and shear banding of metallic glasses, Acta Mater. **61** (2013) 5928-5936.

[37] J.C. Ye, J. Lu, C.T. Liu, Q. Wang and Y. Yang, Atomistic free-volume zones and inelastic deformation of metallic glasses, Nat. Mater. **9** (2010) 619-623.

[38] Y.H. Liu, D. Wang, K. Nakajima, W. Zhang, A. Hirata, *et al.*, Characterization of Nanoscale Mechanical Heterogeneity in a Metallic Glass by Dynamic Force Microscopy, Phys. Rev. Lett. **106** (2011) 125504.

[39] J. Ding, S. Patinet, M.L. Falk, Y. Cheng and E. Ma, Soft spots and their structural signature in a metallic glass, P. Natl. Acad. Sci. USA **111** (2014) 14052–14056.

[40] R. Soklaski, Z. Nussinov, Z. Markow, K.F. Kelton and L. Yang, Connectivity of icosahedral network and a dramatically growing static length scale in Cu-Zr binary metallic glasses, Phys. Rev. B **87** (2013) 184203.

[41] F. Spaepen, A microscopic mechanism for steady state inhomogeneous flow in metallic glasses, Acta Metall. **25** (1977) 407-415.

[42] A.S. Argon, Mechanisms of inelastic deformation in metallic glasses, J. Phys. Chem. Solids **43** (1982) 945-961.

[43] Y. Fan, T. Iwashita and T. Egami, How thermally activated deformation starts in metallic glass, Nat. Comm. **5** (2014).

[44] M.L. Falk and J.S. Langer, Dynamics of viscoplastic deformation in amorphous solids, Phys. Rev. E **57** (1998) 7192-7205.

[45] D. Gritti, T. Gyger and V. Von Niederhausern, Method for shaping a barrel spring made of metallic glass, **US 8720246 B2** (2014).

[46] Z.Q. Liu and Z.F. Zhang, Strengthening and toughening metallic glasses: The elastic perspectives and opportunities, J. Appl. Phys. **115** (2014) 163505.

[47] D. Ma, A.D. Stoica, X.L. Wang, Z.P. Lu, B. Clausen, *et al.*, Elastic Moduli Inheritance and the Weakest Link in Bulk Metallic Glasses, Phys. Rev. Lett. **108** (2012) 085501.

[48] H. Chen and T. Wang, Mechanical Properties of Metallic Glasses of Pd–Si-Based Alloys, J. Appl. Phys. **41** (1970) 5338.

[49] Y.Y. Bai, Y.L. Geng, C.M. Jiang and B. Zhang, beta relaxation and its composition dependence in Ce-based bulk metallic glasses, J. Non-Cryst. Solids **390** (2014) 1-4.

[50] Z. Evenson, S.E. Naleway, S. Wei, O. Gross, J.J. Kruzic, *et al.*, β relaxation and low-temperature aging in a Au-based bulk metallic glass: From elastic properties to atomic-scale structure, Phys. Rev. B **89** (2014) 174204.

[51] Y.H. Liu, T. Fujita, D.P.B. Aji, M. Matsuura and M.W. Chen, Structural origins of Johari-Goldstein relaxation in a metallic glass, Nat. Comm. **5** (2014).

[52] H.B. Yu, K. Samwer, Y. Wu and W.H. Wang, Correlation between β Relaxation and Self-Diffusion of the Smallest Constituting Atoms in Metallic Glasses, Phys. Rev. Lett. **109** (2012) 095508.

[53] H.B. Yu, W.H. Wang, H.Y. Bai, Y. Wu and M.W. Chen, Relating activation of shear transformation zones to β relaxations in metallic glasses, Phys. Rev. B **81** (2010) 220201.

[54] H.B. Yu, K. Samwer, W.H. Wang and H.Y. Bai, Chemical influence on β-relaxations and the formation of molecule-like metallic glasses, Nat. Comm. **4** (2013).

[55] J.D. Eshelby, The Determination of the Elastic Field of an Ellipsoidal Inclusion, and Related Problems, P. Roy. Soc. Lond. A Mat. **241** (1957) 376-396.

[56] C.A. Schuh and A.C. Lund, Atomistic basis for the plastic yield criterion of metallic glass, Nat. Mater. **2** (2003) 449-452.

[57] A.C. Lund and C.A. Schuh, The Mohr–Coulomb criterion from unit shear processes in metallic glass, Intermetallics **12** (2004) 1159-1165.

[58] P.E. Donovan, A yield criterion for $Pd_{40}Ni_{40}P_{20}$ metallic glass, Acta Metall. **37** (1989) 445-456.

[59] M. Zhao and M. Li, Interpreting the change in shear band inclination angle in metallic glasses, Appl. Phys. Lett. **93** (2008) 241906.

[60] Z.F. Zhang, J. Eckert and L. Schultz, Difference in compressive and tensile fracture mechanisms of $Zr_{59}Cu_{20}Al_{10}Ni_8Ti_3$ bulk metallic glass, Acta Mater. **51** (2003) 1167-1179.

[61] W.F. Wu, Y. Li and C.A. Schuh, Strength, plasticity and brittleness of bulk metallic glasses under compression: statistical and geometric effects, Philos. Mag. **88** (2007) 71-89.

[62] S. Naleway, R. Greene, B. Gludovatz, N.N. Dave, R. Ritchie, *et al.*, A Highly Fatigue-Resistant Zr-Based Bulk Metallic Glass, Metall. Mater. Trans. A **44** (2013) 5688-5693.

[63] W.H. Peter, P.K. Liaw, R.A. Buchanan, C.T. Liu, C.R. Brooks, *et al.*, Fatigue behavior of $Zr_{52.5}Al_{10}Ti_5Cu_{17.9}Ni_{14.6}$ bulk metallic glass, Intermetallics **10** (2002) 1125-1129.

[64] Y. Kawamura, T. Nakamura and A. Inoue, Superplasticity in $Pd_{40}Ni_{40}P_{20}$ metallic glass, Scr. Mater. **39** (1998) 301-306.

[65] J. Schroers, The superplastic forming of bulk metallic glasses, JOM-J. Min. Met. Mat. S. **57** (2005) 35-39.

[66] B. Sarac, D. Sopu, E. Park, J.K. Hufenbach, S. Oswald, *et al.*, Mechanical and Structural Investigation of Porous Bulk Metallic Glasses, Metals **5** (2015) 920-933.

[67] R.T. Qu, J.X. Zhao, M. Stoica, J. Eckert and Z.F. Zhang, Macroscopic tensile plasticity of bulk metallic glass through designed artificial defects, Mater. Sci. Eng. A-Struct. Mater. Prop. Microstruct. Process. **534** (2012) 365-373.

[68] Z.T. Wang, J. Pan, Y. Li and C.A. Schuh, Densification and Strain Hardening of a Metallic Glass under Tension at Room Temperature, Phys. Rev. Lett. **111** (2013) 135504.

[69] C.A. Schuh, T.C. Hufnagel and U. Ramamurty, Mechanical behavior of amorphous alloys, Acta Mater. **55** (2007) 4067-4109.

[70] M.Q. Jiang, G. Wilde, J.H. Chen, C.B. Qu, S.Y. Fu, *et al.*, Cryogenic-temperature-induced transition from shear to dilatational failure in metallic glasses, Acta Mater. **77** (2014) 248-257.

[71] E.D. Tabachnikova, A.V. Podol'skii, V.Z. Bengus, S.N. Smirnov, D.V. Luzgin, *et al.*, Low-temperature plasticity anomaly in the bulk metallic glass $Zr_{64.13}Cu_{15.75}Ni_{10.12}Al_{10}$, Low Temp. Phys. **34** (2008) 675-677.

[72] J. Yi, S.M. Seifi, W.H. Wang and J.J. Lewandowski, A Damage-tolerant Bulk Metallic Glass at Liquid-nitrogen Temperature, J. Mater. Sci. Technol. **30** (2014) 627-630.

[73] D. Pan, H. Guo, W. Zhang, A. Inoue and M.W. Chen, Temperature-induced anomalous brittle-to-ductile transition of bulk metallic glasses, Appl. Phys. Lett. **99** (2011) 241907.

[74] Y. Wu, H.X. Li, Z.Y. Liu, G.L. Chen and Z.P. Lu, Interpreting size effects of bulk metallic glasses based on a size-independent critical energy density, Intermetallics **18** (2010) 157-160.

[75] F.F. Wu, Z.F. Zhang, S.X. Mao and J. Eckert, Effect of sample size on ductility of metallic glass, Philos. Mag. Lett. **89** (2009) 178-184.

[76] Z. Han, W.F. Wu, Y. Li, Y.J. Wei and H.J. Gao, An instability index of shear band for plasticity in metallic glasses, Acta Mater. **57** (2009) 1367-1372.

[77] Y.Q. Cheng, Z. Han, Y. Li and E. Ma, Cold versus hot shear banding in bulk metallic glass, Phys. Rev. B **80** (2009) 134115.

[78] D.B. Miracle, A. Concustell, Y. Zhang, A.R. Yavari and A.L. Greer, Shear bands in metallic glasses: Size effects on thermal profiles, Acta Mater. **59** (2011) 2831-2840.

[79] X.J. Gu, A.G. McDermott, S.J. Poon and G.J. Shiflet, Critical Poisson's ratio for plasticity in Fe–Mo–C–B–Ln bulk amorphous steel, Appl. Phys. Lett. **88** (2006) -.

[80] J. Tan, Y. Zhang, M. Stoica, U. Kühn, N. Mattern, *et al.*, Study of mechanical property and crystallization of a ZrCoAl bulk metallic glass, Intermetallics **19** (2011) 567-571.

[81] A. Castellero, D.I. Uhlenhaut, B. Moser and J.F. Löffler, Critical Poisson ratio for room-temperature embrittlement of amorphous $Mg_{85}Cu_5Y_{10}$, Philos. Mag. Lett. **87** (2007) 383-392.

[82] J.J. Lewandowski, W.H. Wang and A.L. Greer, Intrinsic plasticity or brittleness of metallic glasses, Philos. Mag. Lett. **85** (2005) 77-87.

[83] J.R. Rice and R. Thomson, Ductile versus brittle behaviour of crystals, Philos. Mag. **29** (1974) 73-97.

[84] Y. Yang and C.T. Liu, Size effect on stability of shear-band propagation in bulk metallic glasses: an overview, J. Mater. Sci. **47** (2012) 55-67.

[85] S.J. Poon, A. Zhu and G.J. Shiflet, Poisson's Ratio and Intrinsic Plasticity of Metallic Glasses, Appl. Phys. Lett. **92** (2008) 261902.

[86] L.Y. Chen, A.D. Setyawan, H. Kato, A. Inoue, G.Q. Zhang, *et al.*, Free-volume-induced enhancement of plasticity in a monolithic bulk metallic glass at room temperature, Scr. Mater. **59** (2008) 75-78.

[87] D. Pan, A. Inoue, T. Sakurai and M.W. Chen, Experimental characterization of shear transformation zones for plastic flow of bulk metallic glasses, P. Natl. Acad. Sci. USA **105** (2008) 14769-14772.

[88] A.S. Argon and M. Salama, The mechanism of fracture in glassy materials capable of some inelastic deformation, Mater. Sci. Eng. **23** (1976) 219-230.

[89] W.J. Wright, R.R. Byer and X. Gu, High-speed imaging of a bulk metallic glass during uniaxial compression, Appl. Phys. Lett. **102** (2013) 241920.

[90] B. Yang, P.K. Liaw, G. Wang, M. Morrison, C.T. Liu, *et al.*, In-situ thermographic observation of mechanical damage in bulk-metallic glasses during fatigue and tensile experiments, Intermetallics **12** (2004) 1265-1274.

[91] M.M. Trexler and N.N. Thadhani, Mechanical properties of bulk metallic glasses, Prog. Mater. Sci. **55** (2010) 759-839.

[92] A.L. Greer, Y.Q. Cheng and E. Ma, Shear bands in metallic glasses, Mater. Sci. Eng. R **74** (2013) 71-132.

[93] E.R. Homer, Examining the initial stages of shear localization in amorphous metals, Acta Mater. **63** (2014) 44-53.

[94] D. Peirce, R.J. Asaro and A. Needleman, An analysis of nonuniform and localized deformation in ductile single crystals, Acta Metall. **30** (1982) 1087-1119.

[95] S. Kweon and A.A. Benzerga, On the localization of plastic flow in glassy polymers, Eur. J. Mech. A-Solid. **39** (2013) 251-267.

[96] J.W. Rudnicki and J.R. Rice, Conditions for the localization of deformation in pressure-sensitive dilatant materials, J. Mech. Phys. Solids **23** (1975) 371-394.

[97] I. Vardoulakis, Shear band inclination and shear modulus of sand in biaxial tests, Int. J. Numer. Anal. Met. **4** (1980) 103-119.

[98] J.P. Bardet and J. Proubet, The Structure of Shear Bands in Idealized Granular Materials, Appl. Mech. Rev. **45** (1992) S118-S122.

[99] P. Schall and M. van Hecke, Shear Bands in Matter with Granularity, Annu. Rev. Fluid Mech. **42** (2010) 67-88.

[100] Y. Zhang and A.L. Greer, Thickness of shear bands in metallic glasses, Appl. Phys. Lett. **89** (2006) 071907.

[101] P.E. Donovan and W.M. Stobbs, The structure of shear bands in metallic glasses, Acta Metall. **29** (1981) 1419-1436.

[102] E. Pekarskaya, C.P. Kim and W.L. Johnson, In situ transmission electron microscopy studies of shear bands in a bulk metallic glass based composite, J. Mater. Res. **16** (2001) 2513-2518.

[103] P.B. Bowden. The Yield Behaviour of Glassy Polymers. in: R. N. Haward, (Ed.). The Physics of Glassy Polymers. Springer Netherlands, 1973. pp. 279-339.

[104] N. Tariq, J. Akhter and B. Hasan, Effect of sample geometry on the deformation behavior of Zr-based bulk metallic glass, J. Mater. Sci. **45** (2010) 6170-6173.

[105] Y. Zhang, W.H. Wang and A.L. Greer, Making metallic glasses plastic by control of residual stress, Nat. Mater. **5** (2006) 857-860.

[106] N.H. Tariq, J.I. Akhter, A. Khalid, B.A. Hasan and T. Ali, Effect of prior compression treatment on the deformation behavior of Zr based bulk metallic glass, Mater. Chem. Phys. **143** (2014) 1384-1390.

[107] D.C. Hofmann, J.Y. Suh, A. Wiest, G. Duan, M.L. Lind, *et al.*, Designing metallic glass matrix composites with high toughness and tensile ductility, Nature **451** (2008) 1085-1089.

[108] J.M. Park, D.H. Kim, M. Stoica, N. Mattern, R. Li, *et al.*, The influence of in situ formed precipitates on the plasticity of Fe-Nb-B-Cu bulk metallic glasses, J. Mater. Res. **26** (2011) 2080-2086.

[109] D. Klaumünzer, A. Lazarev, R. Maass, F.H. Dalla Torre, A. Vinogradov, *et al.*, Probing shear-band initiation in metallic glasses, Phys. Rev. Lett. **107** (2011) 185502.

[110] Y.M. Chen, T. Ohkubo, T. Mukai and K. Hono, Structure of shear bands in $Pd_{40}Ni_{40}P_{20}$ bulk metallic glass, J. Mater. Res. **24** (2009) 1-9.

[111] H. Rösner, M. Peterlechner, C. Kubel, V. Schmidt and G. Wilde, Density changes in shear bands of a metallic glass determined by correlative analytical transmission electron microscopy, Ultramicroscopy **142** (2014) 1-9.

[112] A.J. Cao, Y.Q. Cheng and E. Ma, Structural processes that initiate shear localization in metallic glass, Acta Mater. **57** (2009) 5146-5155.

[113] Y. Ritter and K. Albe, Thermal annealing of shear bands in deformed metallic glasses: Recovery mechanisms in $Cu_{64}Zr_{36}$ studied by molecular dynamics simulations, Acta Mater. **59** (2011) 7082-7094.

[114] D.V. Louzguine-Luzgin, V.Y. Zadorozhnyy, N. Chen and S.V. Ketov, Evidence of the existence of two deformation stages in bulk metallic glasses, J. Non-Cryst. Solids **396–397** (2014) 20-24.

[115] H.S. Chen, Plastic flow in metallic glasses under compression, Scr. Met. Mater. **7** (1973) 931-935.

[116] H. Kimura and T. Masumoto, A model of the mechanics of shear-crack propagation in tearing for amorphous metals II. Kinetics of inhomogeneous flow, Philos. Mag. A **44** (1981) 1021-1030.

[117] A. Dubach, F.H. Dalla Torre and J.F. Löffler, Deformation kinetics in Zr-based bulk metallic glasses and its dependence on temperature and strain-rate sensitivity, Philos. Mag. Lett. **87** (2007) 695-704.

[118] D. Klaumünzer, R. Maaß and J.F. Löffler, Stick-slip dynamics and recent insights into shear banding in metallic glasses, J. Mater. Res. **26** (2011) 1453-1463.

[119] K. Georgarakis, M. Aljerf, Y. Li, A. LeMoulec, F. Charlot, *et al.*, Shear band melting and serrated flow in metallic glasses, Appl. Phys. Lett. **93** (2008) 031907.

[120] R. Maaß, D. Klaumünzer and J.F. Löffler, Propagation dynamics of individual shear bands during inhomogeneous flow in a Zr-based bulk metallic glass, Acta Mater. **59** (2011) 3205-3213.

[121] H. Neuhäuser, Rate of shear band formation in metallic glasses, Scr. Met. Mater. **12** (1978) 471-474.

[122] W.J. Wright, R. Saha and W.D. Nix, Deformation mechanisms of the $Zr_{40}Ti_{14}Ni_{10}Cu_{12}Be_{24}$ bulk metallic glass, Mater. Trans. **42** (2001) 642-649.

[123] S.-H. Joo, H. Kato, K. Gangwar, S. Lee and H.S. Kim, Shear banding behavior and fracture mechanisms of $Zr_{55}Al_{10}Ni_5Cu_{30}$ bulk metallic glass in uniaxial compression analyzed using a digital image correlation method, Intermetallics **32** (2013) 21-29.

[124] S.X. Song, X.L. Wang and T.G. Nieh, Capturing shear band propagation in a Zr-based metallic glass using a high-speed camera, Scr. Mater. **62** (2010) 847-850.

[125] H. Guo, J. Wen, N.M. Xiao, Z.F. Zhang and M.L. Sui, The more shearing, the thicker shear band and heat-affected zone in bulk metallic glass, J. Mater. Res. **23** (2008) 2133-2138.

[126] J.J. Lewandowski and A.L. Greer, Temperature rise at shear bands in metallic glasses, Nat. Mater. **5** (2006) 15-18.

[127] S.K. Slaughter, F. Kertis, E. Deda, X. Gu, W.J. Wright, *et al.*, Shear bands in metallic glasses are not necessarily hot, APL Materials **2** (2014) 096110.

[128] S.X. Song, H. Bei, J. Wadsworth and T.G. Nieh, Flow serration in a Zr-based bulk metallic glass in compression at low strain rates, Intermetallics **16** (2008) 813-818.

[129] R. Maaß, D. Klaumünzer, E.I. Preiß, P.M. Derlet and J.F. Löffler, Single shear-band plasticity in a bulk metallic glass at cryogenic temperatures, Scr. Mater. **66** (2012) 231-234.

[130] D. Klaumünzer, R. Maaß, F.H. Dalla Torre and J.F. Löffler, Temperature-dependent shear band dynamics in a Zr-based bulk metallic glass, Appl. Phys. Lett. **96** (2010) 061901.

[131] W.J. Wright, M.W. Samale, T.C. Hufnagel, M.M. LeBlanc and J.N. Florando, Studies of shear band velocity using spatially and temporally resolved measurements of strain during quasistatic compression of a bulk metallic glass, Acta Mater. **57** (2009) 4639-4648.

[132] D. Klaumünzer, A. Lazarev, R. Maaß, F.H. Dalla Torre, A. Vinogradov, *et al.*, Probing Shear-Band Initiation in Metallic Glasses, Physical Review Letters **107** (2011) 185502.

[133] R.T. Qu, Z.Q. Liu, G. Wang and Z.F. Zhang, Progressive shear band propagation in metallic glasses under compression, Acta Mater. **91** (2015) 19-33.

[134] R. Maaß and J.F. Löffler, Shear-Band Dynamics in Metallic Glasses, Adv. Funct. Mater. **25** (2015) 2353-2368.

[135] H.M. Chen, J.C. Huang, S.X. Song, T.G. Nieh and J.S.C. Jang, Flow serration and shear-band propagation in bulk metallic glasses, Appl. Phys. Lett. **94** (2009) 141914.

[136] R. Maaß, D. Klaumünzer, G. Villard, P.M. Derlet and J.F. Löffler, Shear-band arrest and stress overshoots during inhomogeneous flow in a metallic glass, Appl. Phys. Lett. **100** (2012) 071904.

[137] D. Klaumünzer, Stick-slip shear banding in metallic glasses, ETH Zurich Diss. Nr. **20562** (2012), Zurich, Switzerland.

[138] E.G. Daub, D. Klaumünzer and J.F. Löffler, Effective temperature dynamics of shear bands in metallic glasses, Phys. Rev. E **90** (2014) 062405.

[139] B.A. Sun, S. Pauly, J. Hu, W.H. Wang, U. Kühn, *et al.*, Origin of Intermittent Plastic Flow and Instability of Shear Band Sliding in Bulk Metallic Glasses, Phys. Rev. Lett. **110** (2013) 225501.

[140] D. Jang and J.R. Greer, Transition from a strong-yet-brittle to a stronger-and-ductile state by size reduction of metallic glasses, Nat. Mater. **9** (2010) 215-219.

[141] A. Donohue, F. Spaepen, R.G. Hoagland and A. Misra, Suppression of the shear band instability during plastic flow of nanometer-scale confined metallic glasses, Appl. Phys. Lett. **91** (2007) 241905.

[142] B.E. Schuster, Q. Wei, T.C. Hufnagel and K.T. Ramesh, Size-independent strength and deformation mode in compression of a Pd-based metallic glass, Acta Mater. **56** (2008) 5091-5100.

[143] X.L. Wu, Y.Z. Guo, Q. Wei and W.H. Wang, Prevalence of shear banding in compression of Zr41Ti14Cu12.5Ni10Be22.5 pillars as small as 150 nm in diameter, Acta Mater. **57** (2009) 3562-3571.

[144] W.L. Johnson, J. Lu and M.D. Demetriou, Deformation and flow in bulk metallic glasses and deeply undercooled glass forming liquids—a self consistent dynamic free volume model, Intermetallics **10** (2002) 1039-1046.

[145] M.Q. Jiang, G. Wilde and L.H. Dai, Origin of stress overshoot in amorphous solids, Mechanics of Materials **81** (2015) 72-83.

[146] J.S. Langer, Shear-transformation-zone theory of plastic deformation near the glass transition, Phys. Rev. E **77** (2008) 021502.

[147] L. Li, E.R. Homer and C.A. Schuh, Shear transformation zone dynamics model for metallic glasses incorporating free volume as a state variable, Acta Mater. **61** (2013) 3347-3359.

[148] J. Schroers, B. Lohwongwatana, W.L. Johnson and A. Peker, Gold based bulk metallic glass, Appl. Phys. Lett. **87** (2005) 061912.

[149] A. Inoue, W. Zhang, T. Zhang and K. Kurosaka, Cu-Based Bulk Glassy Alloys with Good Mechanical Properties in Cu-Zr-Hf-Ti System, Mater. Trans. **42** (2001) 1805-1812.

[150] Q. Zhang, S. Pang, Y. Li and T. Zhang, Correlation between supercooled liquid region and crystallization behavior with alloy composition of La–Al–Cu metallic glasses, Science China Physics, Mechanics and Astronomy **54** (2011) 1608-1611.

[151] H. Tan, Z. Lu, H. Yao, B. Yao, Y. Feng, *et al.*, Glass Forming Ability of La-rich La-Al-Cu Ternary Alloys, Mater. Trans. **42** (2001) 551-555.

[152] L. Xia, W.H. Li, S.S. Fang, B.C. Wei and Y.D. Dong, Binary Ni–Nb bulk metallic glasses, J. Appl. Phys. **99** (2006) 026103.

[153] J. Schroers and W.L. Johnson, Ductile Bulk Metallic Glass, Phys. Rev. Lett. **93** (2004) 255506.

[154] J. Qiang, X. Ding, Y. Wang, Q. Wang, Q. Duan, *et al.*, A Zr–Co–Al Bulk Metallic Glass Derived from the Atomic-Cluster-Plus-Glue-Atom Model and Its Mechanical Properties, Transactions of the Indian Institute of Metals **65** (2012) 577-580.

[155] J. Schroers and W.L. Johnson, Highly processable bulk metallic glass-forming alloys in the Pt–Co–Ni–Cu–P system, Appl. Phys. Lett. **84** (2004) 3666-3668.

[156] Y. Yokoyama, K. Fukaura and A. Inoue, Formation and mechanical properties of Zr–Cu–Al bulk glassy alloys, Mater. Sci. Eng. A **375–377** (2004) 427-431.

[157] Z.D. Sha, Q.X. Pei, Z.S. Liu, Y.W. Zhang and T.J. Wang, Necking and notch strengthening in metallic glass with symmetric sharp-and-deep notches, Sci. Rep. **5** (2015).

[158] G. Villard, Stress Overshoots During Inhomogeneous Non-Serrated Flow of a Zr-Based Bulk Metallic Glass, Master's thesis, Laboratory of Metal Physics and Technology, ETH Zurich (2011).

[159] J. Antonaglia, X. Xie, G. Schwarz, M. Wraith, J.W. Qiao, *et al.*, Tuned Critical Avalanche Scaling in Bulk Metallic Glasses, Sci. Rep. **4** (2014) 4382.

[160] J. Antonaglia, W.J. Wright, X. Gu, R.R. Byer, T.C. Hufnagel, *et al.*, Bulk Metallic Glasses Deform via Slip Avalanches, Phys. Rev. Lett. **112** (2014) 155501.

[161] J.X. Zhao, F.F. Wu, R.T. Qu, S.X. Li and Z.F. Zhang, Plastic deformability of metallic glass by artificial macroscopic notches, Acta Mater. **58** (2010) 5420-5432.

[162] F. Haag, D. Beitelschmidt, J. Eckert and K. Durst, Influences of residual stresses on the serrated flow in bulk metallic glass under elastostatic four-point bending – A nanoindentation and atomic force microscopy study, Acta Mater. **70** (2014) 188-197.

[163] F.H. Dalla Torre, A. Dubach, M.E. Siegrist and J.F. Löffler, Negative strain rate sensitivity in bulk metallic glass and its similarities with the dynamic strain aging effect during deformation, Appl. Phys. Lett. **89** (2006) 091918.

[164] Y.Q. Cheng, E. Ma and H.W. Sheng, Atomic Level Structure in Multicomponent Bulk Metallic Glass, Phys. Rev. Lett. **102** (2009) 245501.

[165] J. Zemp, M. Celino, B. Schönfeld and J.F. Löffler, Icosahedral superclusters in $Cu_{64}Zr_{36}$ metallic glass, Phys. Rev. B **90** (2014) 144108.

[166] J. Zemp, M. Celino, B. Schönfeld and J.F. Löffler, Crystal-Like Rearrangements of Icosahedra in Simulated Copper-Zirconium Metallic Glasses and their Effect on Mechanical Properties, Phys. Rev. Lett. **115** (2015) 165501.

[167] A. Dubach, F.H. Dalla Torre and J.F. Löffler, Constitutive model for inhomogeneous flow in bulk metallic glasses, Acta Mater. **57** (2009) 881-892.

[168] F.H. Dalla Torre, D. Klaumünzer, R. Maaß and J.F. Löffler, Stick–slip behavior of serrated flow during inhomogeneous deformation of bulk metallic glasses, Acta Mater. **58** (2010) 3742-3750.

[169] T. Masumoto and R. Maddin, The mechanical properties of palladium 20 a/o silicon alloy quenched from the liquid state, Acta Metall. **19** (1971) 725-741.

[170] M. Yamada, Y. Tanimoto, T. Yamasaki, T. Kikuchi, Y. Yokoyama, *et al.*, Compositional Dependence of the Viscosity of Zr–Cu–Al Alloys in the Supercooled Liquid State, J. Soc. Mater. Sci., Jpn. **59** (2010) 124-129.

[171] R. Ferro and A. Saccone. Structure of intermetallic ocmpounds and phases. in: R. W. Cahn and P. Haasen, (Eds.). Physical Metallurgy. Elsevier Science B.V, Amsterdam, 1996. pp. 329.

[172] M.I. Mendelev, M.J. Kramer, R.T. Ott, D.J. Sordelet, D. Yagodin, *et al.*, Development of suitable interatomic potentials for simulation of liquid and amorphous Cu–Zr alloys, Philos. Mag. **89** (2009) 967-987.

[173] W.M. Haynes, T.J. Bruno and D.R. Lide, (Eds.). CRC Handbook of Chemistry and Physics. 95 ed., CRC Press/Taylor and Francis, Boca Raton, FL, 2015.

[174] P. Thurnheer, R. Maaß, K.J. Laws, S. Pogatscher and J.F. Löffler, Dynamic properties of major shear bands in Zr–Cu–Al bulk metallic glasses, Acta Mater. **96** (2015) 428-436.

[175] S. Mukherjee, H.G. Kang, W.L. Johnson and W.K. Rhim, Noncontact measurement of crystallization behavior, specific volume, and viscosity of bulk glass-forming Zr–Al–Co–(Cu) alloys, Phys. Rev. B **70** (2004) 174205.

[176] P. Thurnheer, R. Maaß, S. Pogatscher and J.F. Löffler, Compositional dependence of shear-band dynamics in the Zr–Cu–Al bulk metallic glass system, Appl. Phys. Lett. **104** (2014) 101910.

[177] M. Hagiwara, A. Inoue and T. Masumoto, Production of amorphous Co–Si–B and Co–M–Si–B (M ≡ Group IV – VIII transition metals) wires by a method employing melt spinning into rotating water and some properties of the wires, Mater. Sci. Eng. **54** (1982) 197-207.

[178] B. Shen, C. Chang and A. Inoue, Ni-based bulk glassy alloys with superhigh strength of 3800 MPa in Ni–Fe–B–Si–Nb system, Appl. Phys. Lett. **88** (2006) 201903.

[179] P.J. Tao, Y.Z. Yang, X.J. Bai, Z.W. Xie and X.C. Chen, Room temperature plastic deformation behavior of ZrCuNiAl bulk metallic glasses, Int. J. Miner. Metall. Mater. **17** (2010) 327-330.

[180] O.N. Senkov, Correlation between fragility and glass-forming ability of metallic alloys, Phys. Rev. B **76** (2007) 104202.

[181] R. Babilas, R. Nowosielski, G. Dercz, Z. Stoklasa and W. Gluchowski, Influence of structure on stoft magnetic properties of $Co_{70}Fe_5Si_{15}B_{10}$ metallic glass ribbons, Archives of Material Science and Engineering **54** (2012) 37-44.

[182] H.S. Chen and M. Goldstein, Anomalous Viscoelastic Behavior of Metallic Glasses of Pd–Si-Based Alloys, J. Appl. Phys. **43** (1972) 1642-1648.

[183] D. Granata, E. Fischer, V. Wessels and J.F. Löffler, The detrimental effect of flux-induced boron alloying in Pd–Si–Cu bulk metallic glasses, Appl. Phys. Lett. **106** (2015).

[184] B.A. Legg, J. Schroers and R. Busch, Thermodynamics, kinetics, and crystallization of $Pt_{57.3}Cu_{14.6}Ni_{5.3}P_{22.8}$ bulk metallic glass, Acta Mater. **55** (2007) 1109-1116.

[185] P. Guan, M. Chen and T. Egami, Stress-Temperature Scaling for Steady-State Flow in Metallic Glasses, Phys. Rev. Lett. **104** (2010) 205701.

[186] R.E. Baumer and M.J. Demkowicz, Glass Transition by Gelation in a Phase Separating Binary Alloy, Phys. Rev. Lett. **110** (2013) 145502.

[187] W.H. Wang, Correlation between relaxations and plastic deformation, and elastic model of flow in metallic glasses and glass-forming liquids, J. Appl. Phys. **110** (2011) 053521.

[188] M.D. Demetriou, M.E. Launey, G. Garrett, J.P. Schramm, D.C. Hofmann, *et al.*, A damage-tolerant glass, Nat. Mater. **10** (2011) 123-128.

[189] W. Dmowski, Y. Tong, T. Iwashita, Y. Yokoyama and T. Egami, Universal mechanism of thermomechanical deformation in metallic glasses, Phys. Rev. B **91** (2015) 060101.

[190] K.J. Laws, D.B. Miracle and M. Ferry, A predictive structural model for bulk metallic glasses, Nat. Comm. **6** (2015) 8123.

[191] D.B. Miracle, D.V. Louzguine-Luzgin, L. Louzguina-Luzgina and A. Inoue, An Assessment of Binary Metallic glasses: Correlations between Structure, Glass Forming Ability and Stability, Int. Mater. Rev. **55** (2010) 218.

[192] B. Cordero, V. Gomez, A.E. Platero-Prats, M. Reves, J. Echeverria, *et al.*, Covalent radii revisited, Dalton Transactions (2008) 2832-2838.

[193] S. Hartley, W. Holmes, J. Jacques, M. Mole and J. McCoubrey, Thermochemical properties of phosphorus compounds, Quarterly Reviews, Chemical Society **17** (1963) 204-223.

[194] K.J. Laws, D.B. Miracle and M. Ferry, A Predictive Structural Model for Bulk Metallic Glasses, Nat. Comm. (2015).

[195] H.S. Chen and D. Turnbull, Thermal Properties of Gold-Silicon Binary Alloy near the Eutectic Composition, J. Appl. Phys. **38** (1967) 3646-3650.

[196] A. Takeuchi and A. Inoue, Classification of Buk Metallic Glasses by Atomic Size Difference, Heat of Mixing and Period of Constituent Elements and Its Application to Characterization of the Main Alloying Element, Mater. Trans. **46** (2005) 2817-2829.

[197] G. Fiore, P. Rizzi and L. Battezzati, Phase constitution and glass formation in an Au-based alloy, J. Alloy. Compd. **509, Supplement 1** (2011) S166-S169.

[198] D.A. Porter and K.E. Easterling. Phase Transformations in Metals and Alloys, Van Nostrand Reinhold Co. Ltd., Oxford, 1981.

[199] D.B. Miracle, G.B. Wilks, A.G. Dahlman and J.E. Dahlman, The strength of chemical bonds in solids and liquids, Acta Mater. **59** (2011) 7840-7854.

[200] M. Winter. WebElements. vol. 2015. University of Sheffield, UK, 2015.

[201] Y. Huang, J. Shen, J. Sun and Z. Zhang, Enhanced strength and plasticity of a Ti-based metallic glass at cryogenic temperatures, Mater. Sci. Eng. A **498** (2008) 203-207.

[202] L. Zhang, Y.Q. Cheng, A.J. Cao, J. Xu and E. Ma, Bulk metallic glasses with large plasticity: Composition design from the structural perspective, Acta Mater. **57** (2009) 1154-1164.

[203] K. Georgarakis, Y. Li, M. Aljerf, D. Dudina, A. LeMoulec, *et al.*, Glass formation in the Nb–Si binary system, J. Alloy. Compd. **504, Supplement 1** (2010) S14-S17.

[204] A. Williams, M. Mehra and W.L. Johnson, The structure and properties of some Rh 0.92-x B x Si 0.08 metallic glasses, J. Phys. F Met. Phys. **12** (1982) 1861.

[205] Q. Zheng, H. Ma, E. Ma and J. Xu, Mg–Cu–(Y, Nd) pseudo-ternary bulk metallic glasses: The effects of Nd on glass-forming ability and plasticity, Scr. Mater. **55** (2006) 541-544.

[206] K. Amiya and A. Inoue, Formation, Thermal Stability and Mechanical Properties of Ca-Based Bulk Glassy Alloys, Mater. Trans. **43** (2002) 81-84.

[207] M. Stoica, J. Das, J. Bednarcik, H. Franz, N. Mattern, *et al.*, Strain distribution in Zr64.13Cu15.75Ni10.12Al10 bulk metallic glass investigated by in situ tensile tests under synchrotron radiation, J. Appl. Phys. **104** (2008).

[208] W. Wei Hua, The elastic properties, elastic models and elastic perspectives of metallic glasses, Prog. Mater. Sci. **57** (2012) 487-656.

[209] Y.Q. Cheng, A.J. Cao and E. Ma, Correlation between the elastic modulus and the intrinsic plastic behavior of metallic glasses: The roles of atomic configuration and alloy composition, Acta Mater. **57** (2009) 3253-3267.

[210] H. Ait-Amokhtar, C. Fressengeas and S. Boudrahem, The dynamics of Portevin–Le Chatelier bands in an Al–Mg alloy from infrared thermography, Mater. Sci. Eng. A **488** (2008) 540-546.

[211] M.P. Luong, Fatigue limit evaluation of metals using an infrared thermographic technique, Mechanics of Materials **28** (1998) 155-163.

[212] O. Plekhov, T. Palin-Luc, N. Saintier, S. Uvarov and O. Naimark, Fatigue crack initiation and growth in a 35CrMo4 steel investigated by infrared thermography, Fatigue Fract. Eng. M. **28** (2005) 169-178.

[213] G. Wang, Q. Feng, B. Yang, W. Jiang, P.K. Liaw, *et al.*, "Thermographic studies of temperature evolutions in bulk metallic glasses: An overview", Intermetallics **30** (2012) 1-11.

[214] J.J. Luo, G.Y. Wang, H.R. Qi, Y. Yokoyama, P.K. Liaw, *et al.*, Interpreting temperature evolution of a bulk-metallic glass during cyclic loading through spatial-temporal modeling, Intermetallics **29** (2012) 1-13.

[215] B. Yang, P.K. Liaw, M. Morrison, C.T. Liu, R.A. Buchanan, *et al.*, "Temperature evolution during fatigue damage", Intermetallics **13** (2005) 419-428.

[216] P. Thurnheer, R. Maaß, K.J. Laws and J.F. Löffler, How topology and chemistry determine shear stability in metallic glasses, (in preparation).

[217] G. Wang, Q. Feng, B. Yang, W. Jiang, P.K. Liaw, *et al.*, Thermographic studies of temperature evolutions in bulk metallic glasses: An overview, Intermetallics **30** (2012) 1-11.

[218] Y. Zhang, N.A. Stelmashenko, Z.H. Barber, W.H. Wang, J.J. Lewandowski, *et al.*, Local temperature rises during mechanical testing of metallic glasses, J. Mater. Res. **22** (2007) 419-427.

"Five years, my brain hurts a lot,
Five years, that's all we've got!"

David Bowie